Faculty of Mathematics and Physics
Charles University

Doctoral thesis

Jakub Dostálek

Rich information optical biosensor based on surface plasmon resonance

Supervisor: Dr. Jiří Homola

Institute of Radio Engineering and
Electronics, Academy of Sciences of the
Czech Republic
Department of Optical Sensors

Study program: Quantum Optics and Optoelectronics

Author: Jakub Dostálek
Title: Rich information optical biosensor based on surface plasmon resonance
Abstract:

In the presented thesis, new optical biosensor platform for high-throughput label-free monitoring of biomolecular interactions is reported. This biosensor platform is based on a spectroscopy of surface plasmons on an array of miniature diffraction gratings. Each miniature grating serves as an independent sensing channel and allows for monitoring of optical density changes induced by biomolecular interactions on the grating surface. The presented platform has a potential for monitoring of hundreds of interactions on a single sensor chip. The presented research include theoretical study of surface plasmon resonance on metallic diffraction gratings and the analysis of diffraction grating-based SPR biosensor. In the experimental work, preparation, replication and characterization of diffraction gratings is carried out. A prototype SPR sensor device including an SPR sensor chip with a two-dimensional array of sensing channels, fluidic system and SPR chip reader is developed and its main performance characteristics are determined.

Keywords: surface plasma resonance; diffraction grating, biosensor;
Department:
Department of Chemical Physics and Optics
Faculty of Mathematics and Physics
Charles University in Prague
Specialization: F-6 Quantum Optics and Optoelectronics
Supervisor: Jiří Homola
Organization:
Institute of Radio Engineering and Electronics
Chaberská 57
CZ-18251 Prague
Tel +420 266 773 407
Fax +420 284 680 222
Email: dostalek@ure.cas.cz

Prohlašuji, že jsem svou disertační práci napsal samostatně a výhradně s použitím citovaných pramenů. Souhlasím se zapůjčováním práce.

(I declare that all results and conclusions in this thesis were obtained only with the use of the bibliographed references. I agree with using and distributing of the work for studying and reffering purposes.)

V Praze dne 3. května 2006

(In Prague, 3. May 2006)

Table of contents:

1. Introduction

Sensors become increasingly exploited technology for detection and analysis of various chemical and biological compounds. In important areas such as environmental monitoring, medical diagnostics, food safety and security, chemical sensors are pursued for economical and fast analysis of chemical compounds. Chemical sensors are devices which convert a quantity of interest (e.g. concentration of target molecule) into a signal. These sensors can be combined with biorecognition elements (e.g. antibodies, enzymes or DNA) taking advantage of their unique sensitivity and selectivity. Such devices are referred as to biosensors and they can be divided to three main groups - electrochemical [1]-[2], electromechanical [3]-[5] and optical [6]-[13]. Up to now, myriads of optical biosensors have been developed [14]-[16] including the ones relying on molecular spectroscopy (IR absorption spectroscopy [6], UV absorption spectroscopy [17], Raman scattering spectroscopy [7]), fluorescence (fluorescence intensity measurement [8], fluorescence quenching [9], fluorescence resonance energy transfer [10]), spectroscopy of guided modes (resonant mirror [11], grating coupler [13]), interferometry [18], colorimetry [12], reflectometry [19], ellipsometry [20] and surface plasmon resonance (SPR) [26]-[29]. Among these, SPR biosensors offer an attractive sensor platform which in conjunction with appropriate biorecognition elements can be tailored for analysis and detection of chemical and biological compounds without the need molecule labeling. Up to now, numerous SPR biosensors were commercialized [21]-[24] and they have found wide range of applications in biomolecular interaction analysis (BIA) [25] and detection of compounds relevant to environmental monitoring (e.g. herbicides [30]), food safety (e.g. protein toxins [31], bacteria [32], [33]), medical diagnostics (e.g. DNA [34], hormones [35]) and security (e.g. toxins [31], [36]).

Nowadays, we witness growing needs for increasing throughput of optical biosensors. For instance, such devices are attractive for high-throughput analysis of proteins and their interaction in areas such as proteome research and drug discovery [37]-[40]. Among others, protein chips (which are counterparts to already established DNA chips) are pursued for these applications. Two main principles for optical readout of protein chips are possible. The more traditional approach employs fluorescent or radioactive tags used for visualization of binding of molecules no an array of molecular probes on the chip surface [41], [42]. However, as labeling of biomolecules imposes an additional time consuming step and it can alter functionality of studied biomolecules, another - label-free - approaches are pursued [16], [27], [29].

The subject of this thesis is development of a novel SPR sensor platform for high-throughput and label-free analysis of biomolecular analytes. The presented approach relies on spectroscopy of surface plasmons on an array of metallic diffraction gratings. Comparing with conventional SPR sensors utilizing prism couplers, diffraction grating based sensors offer numerous advantages including the potential for more economical preparation of sensor chips (e.g. using injection moulding or hot embossing of plastics), simpler use (optical contact between the sensor chip and a coupler is not required) and flexibility in the design of the system supporting the SPR biosensor.

1.1 Fundamentals of surface plasmon resonance

Surface plasmon resonance is an optical phenomenon in which light interacts with a *surface plasma wave* (SPW). This wave is also referred as to surface plasmon polariton (SPP) and it originates from coupled oscillations of electromagnetic field and density of electron plasma on a metal surface. Surface plasmon resonance was first observed in 1902 by R.W. Wood as anomalies in the diffraction efficiency of shallow metallic diffraction gratings [43]. In the forties of last century, these anomalies were found to be related to the excitation of waves guided along the surface of metallic diffraction gratings [44] later identified as SPWs. Since then, research in surface plasmon resonance originally related to diffraction gratings [45]-[48] has flourished in numerous fields [49], [50], [51] including non-linear optics (e.g. Raman scattering and second harmonic generation [52]-[54]), metrology (e.g. surface roughness [55]-[57] and optical properties of metals [58]), SPP optics on nanostructured objects (e.g. metal nanoparticles [59], [60], chains of metal nanoparticles [61], [62] and subwavelength arrays of holes [63]), lasers [64], optical data storage [65], photonic bandgap structures [66], [67], sub-diffraction imaging [68], surface plasmon-based integrated optics [69] and optical sensors [70]-[76].

1.1.1 Surface plasma wave on a planar surface

In this section, let us describe properties of surface plasma wave on planar surfaces. Let us assume the geometry composed of a plane interface between semi-infinite, isotropic, homogenous, non-magnetic metal and dielectric. From Maxwell equations with standard boundary conditions follows the existence of one and only one mode guided at the metal – dielectric interface, [57]. This mode is referred as to surface plasma wave (SPW) and its dispersion relation can be expressed as:

$$k_{SPW} = k_0 \sqrt{\frac{\varepsilon_m \varepsilon_d}{\varepsilon_m + \varepsilon_d}}\,, \tag{1.1}$$

where k_{SPW} is the SPW propagation constant, $k_0=\omega/c$ is the propagation constant of light in vacuum (ω is the angular frequency and c is the velocity of light in vacuum), ε_d and ε_m are dielectric and metal permittivity, respectively. From boundary conditions it follows, that SPW exists only in transversally magnetic (TM) polarization for which magnetic intensity vector of SPW field is parallel to the metal surface. In addition, SPW exists at frequencies for which $\mathrm{Re}\{\varepsilon_m\}<0$ and $\varepsilon_d<|\mathrm{Re}\{\varepsilon_m\}|$. If the metal permittivity is expressed using Drude’s model, this condition is fulfilled below the metal plasma frequency ω_p.

As metal permittivity ε_m is in general a complex function of the angular frequency, the propagation constant k_{SPW} is complex as well. If we assume real permittivity ε_d and $\mathrm{Im}\{\varepsilon_m\}< |\mathrm{Re}\{\varepsilon_m\}|$, the real and imaginary part of the propagation constant k_{SPW} can be expressed as:

$$\mathrm{Re}\{k_{SPW}\} = k_0 \sqrt{\frac{\mathrm{Re}\{\varepsilon_m\}\varepsilon_d}{\mathrm{Re}\{\varepsilon_m\} + \varepsilon_d}}\,, \tag{1.2}$$

$$\mathrm{Im}\left\{k_{SPW}\right\} = k_0 \left(\frac{\mathrm{Re}\left\{\varepsilon_m\right\} \varepsilon_d}{\mathrm{Re}\left\{\varepsilon_m\right\} + \varepsilon_d} \right)^{3/2} \frac{\mathrm{Im}\left\{\varepsilon_m\right\}}{2\,\mathrm{Re}\left\{\varepsilon_m\right\}^2}. \tag{1.3}$$

SPW propagates along the metal surface with its field exponentially decaying into both metal and dielectric medium with the transverse propagation constants $\sqrt{k_0^2\varepsilon_m - k_{SPW}^2}$ and $\sqrt{k_0^2\varepsilon_d - k_{SPW}^2}$ in the metal and dielectric, respectively. As an example, we calculated the field distribution of SPW propagating along the interface between gold and dielectric with refractive index 1.32. There was used the wavelength of 800 nm and Cartesian coordinates with x axis perpendicular to the interface and y and z axis lying in plane of the interface perpendicular and parallel to SPW propagation, respectively, see Fig. 1a. Obtained spatial distribution of electromagnetic field components E_x, E_z and H_y are presented in Fig. 1b) - Fig. 1d), respectively.

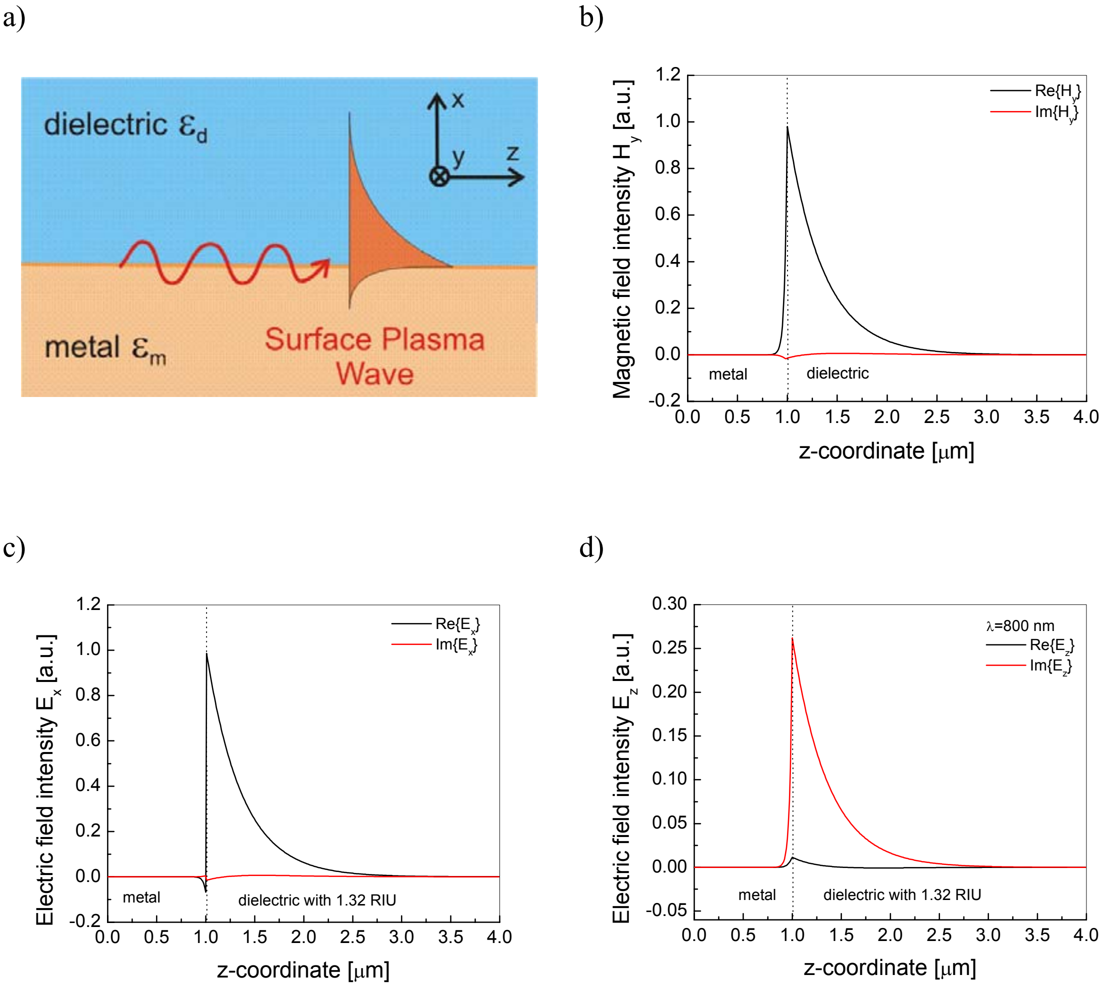

Fig. 1 a) Metal – dielectric interface along which SPW propagates; field distribution of surface plasma wave guided along the interface between gold and a dielectric with refractive index 1.32, wavelength 800 nm; b) magnetic intensity H_y, c) electric intensity E_x and d) electric intensity E_z.

As follows from Equation (1.2), the real part of the propagation constant $\mathrm{Re}\{k_{SPW}\}$ is always higher then the one of an optical wave propagating in the dielectric, see Fig. 2. Therefore, these waves cannot be phase-matched along the metal surface and direct coupling between them is not possible. In order to optically excite SPW, a coupler providing enlargement of the optical wave’s momentum needs to be employed. For this purpose, two types of couplers can be used – *prism coupler* employing the attenuated total reflection method (ATR) [57] and *grating coupler* relying on the diffraction of light on periodic modulated metallic surfaces [48].

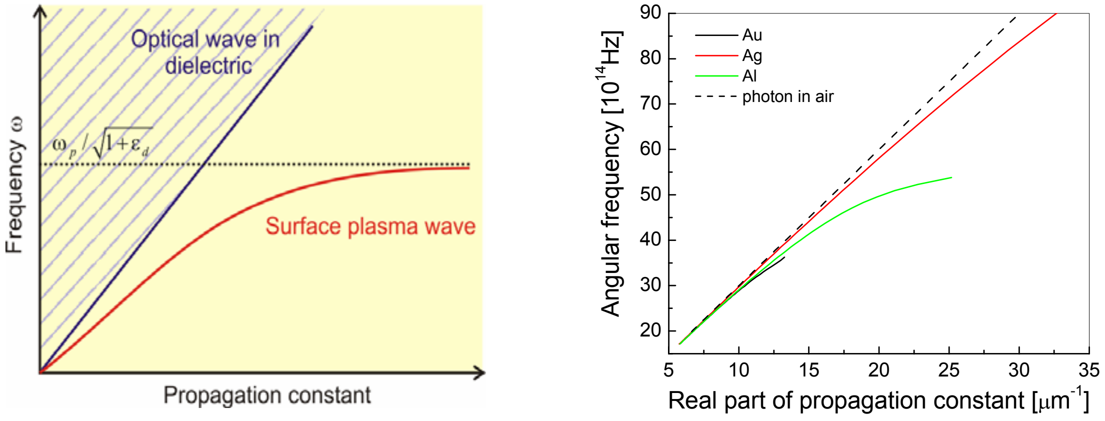

a) b)

Fig. 2 a) Dispersion relation of surface plasma wave propagating along planar interface between metal and dielectric (red curve) and the dispersion relation of optical wave in the dielectric (blue dashed region) for metal without losses, b) dispersion relation of SPW at the interface between air and real metals (gold - black curve, silver - green curve, aluminum - red curve).

1.1.2 Prism coupler for excitation of surface plasma wave

In the prism coupler, optical excitation SPW is achieved by means of the attenuated total reflection method (ATR). Two implementations of ATR method can be used utilizing Otto or Kretschmann geometry. In mostly used Kretschmann geometry of ATR method, an optical beam propagating through the prism with the permittivity ε_p is made incident under an angle of incidence θ on a thin metal layer at the prism base, Fig. 3. Upon its incidence, the optical wave totally reflects and its evanescent field penetrates through the thin metal layer. At the interface between the metal and outer dielectric with lower refractive index ($\varepsilon_d<\varepsilon_p$) SPW can be excited as the momentum of the incident optical wave is higher than the one of an optical wave propagating in the outer dielectric, see Fig. 4. Excitation of SPW occurs, when the propagation constant of SPW at the interface between the metal and the dielectric with a lower refractive index is matched to the one of the incident optical wave:

$$k_0\sqrt{\varepsilon_p}\,\sin(\theta)=\mathrm{Re}\{k_{SPW}\}\,. \tag{1.4}$$

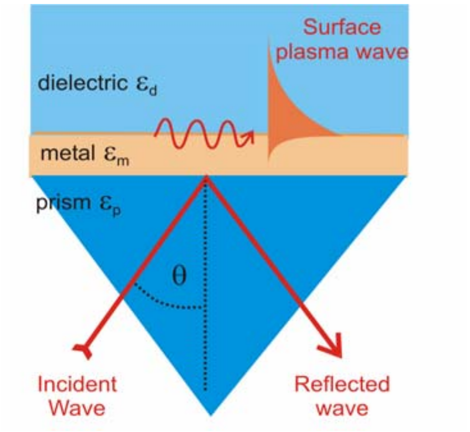

Fig. 3 Attenuated total reflection method with the Kretschmann geometry for excitation of SPW.

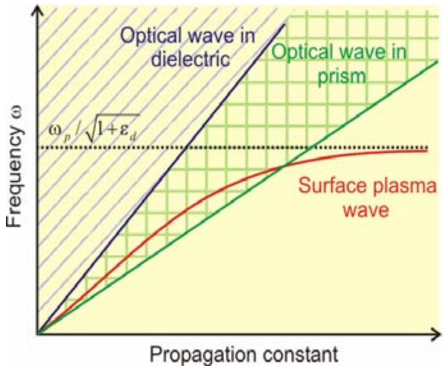

Fig. 4 Dispersion relation of SPW propagating along planar metal - dielectric interface (red curve), the dispersion relation of an optical wave in the dielectric (blue dashed region) and in the prism (green dashed region).

In ATR method with Kretschmann geometry, the strength of the coupling between an optical wave and surface plasma wave can be controlled by varying the thickness of the metal layer. The excitation of SPW manifests itself as a narrow absorption dip in the wavelength or angular spectrum of reflectivity. The spectral position of SPR dip can be determined from phase-matching condition (1.4). As follows from this condition, SPR dip position is a function of refractive index $\sqrt{\varepsilon_d}$ of the dielectric on the metal surface.

1.1.3 Grating coupler for excitation of surface plasma wave

In grating coupler for optical excitation of SPW, diffraction on a periodic modulation of a relief metallic diffraction grating is employed to match the propagation constant of an optical wave and SPW, see Fig. 5. This approach can be explained using the Floquet theorem by means of which dispersion relations of a SPW and an optical wave are described as folded in the first Brillouin zone, Fig. 6. In this zone, the propagation constant of a SPW and the one of an optical wave propagating in the dielectric lie between -π/Λ and π/Λ, where Λ is the period of the periodic modulation. Due to the folding of dispersion relations, component of the propagation vectors of a SPW and of an optical wave parallel to the grating surface can be matched at certain frequencies, see Fig. 6. These frequencies fulfill following equation:

$$k_0\sqrt{\varepsilon_d}\sin\left(\theta\right)+p\frac{2\pi}{\Lambda}=\pm\mathrm{Re}\left\{k_{SPW}\right\}, \tag{1.5}$$

where the first term on the right hand side $k_0\sqrt{\varepsilon_d}\sin\left(\theta\right)$ represents the component of the propagation constant of the incident optical wave and the second term is the contribution due to the diffraction, θ is the angle of incidence of the incident wave and p is an integer. The integer $p \neq 0$ is indexing the order of diffracted wave.

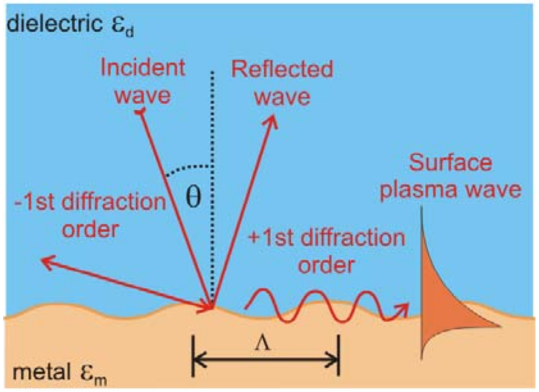

Fig. 5 Example of surface plasma wave guided along periodically corrugated metal-dielectric interface diffraction coupled to an optical wave propagating in the dielectric.

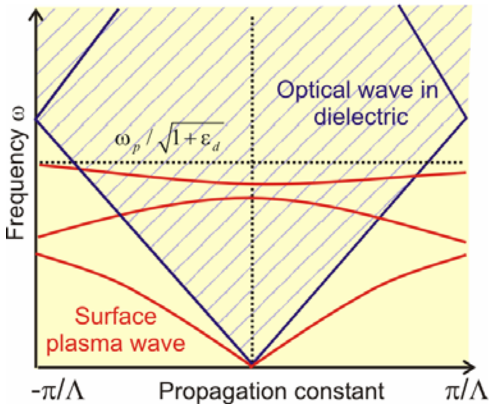

Fig. 6 Dispersion relation of surface plasma wave propagating along a periodically modulated metal - dielectric interface with the dispersion relation of an optical wave in the dielectric (blue dashed region).

The strength of coupling between and an optical wave and a SPW is mainly affected by the profile and depth of the modulation of grating surface. The excitation of SPW on metallic grating is associated with narrow anomaly in the grating efficiency wavelength or angular spectrum. This anomaly is manifested as a peak or a dip in the spectrum depending on the mutual phase between SPW and reflected or diffracted wave. As follows from the condition (1.5), the position of SPR dip or peak is a function of refractive index $\sqrt{\varepsilon_d}$ of the dielectric adjacent to the metal surface.

1.2 Biosensors based on surface plasmon resonance

The application of surface plasmon resonance in sensors was firstly reported in early eighties in [75], [76]. Since then, SPR sensor technology was adopted for measurements of numerous physical and chemical quantities including humidity [70], pressure [71], temperature [73], physical displacement [74], gas concentration [75], electric field [74] and interaction analysis of various chemical and bio-chemical compounds [76]. Among these, applications of SPR for detection of chemical and biomolecular compounds and in biomolecular interactions analysis (BIA) are recently the major and most rapidly evolving areas [27], [28].

1.2.1 Principle of SPR biosensors

In general, an SPR sensor consists of two key components: *sensitive layer* and *SPR refractometer.* The sensitive layer is designed to specifically alter its refractive index or thickness with a change in the measurand of interest. These variations are resolved with SPR refractometer which probes refractive index changes in the sensitive layer with a SPW. Variations in optical characteristics of the sensitive layer alter the propagation constant of SPW which induces a change in parameters of an optical wave exciting the SPW. These changes are subsequently converted into the sensor signal, see Fig. 7.

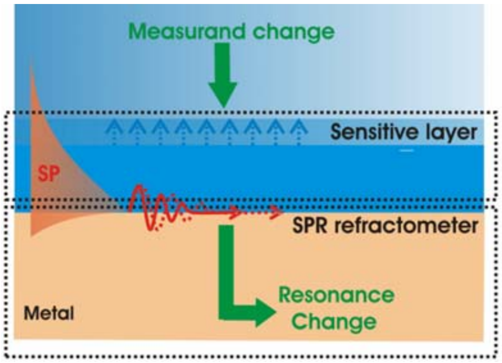

Fig. 7 SPR sensor surface with a sensitive layer converting a measurand change into a change in SPR.

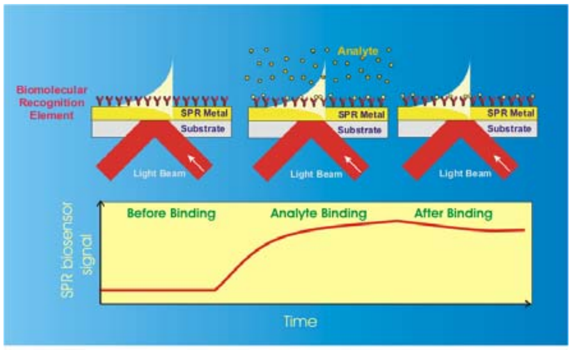

Fig. 8 Scheme of an SPR biosensor with binding of an analyte to bio-recognition elements on the sensor surface.

In SPR biosensors, the sensitive layer is composed of recognition elements which specifically interact with target molecules: e.g. antibodies [77], DNA [78] or special artificial materials such as molecular imprinted polymers [79], [80] and aptamers [81]. If an analyzed sample containing analyte is flowed over the sensor surface, analyte molecules are captured by the recognition elements leading to an increase in the mass at the sensor surface. The increase of the mass produces a change in the refractive index which is measured with the SPR refractometer, see Fig. 8.

1.2.2 Optical configurations used in SPR biosensors

In SPR biosensors, the binding of an analyte to biorecognition elements induces a change in the refractive index change on the sensor surface. These variations alter the propagation constant of SPW which alters characteristics of the optical wave exciting the SPW. Up to now, the following approaches for measurement of variations in optical wave parameters were used in SPR sensors: *spectroscopy of surface plasmons*, *SPR intensity modulation* and *SPR phase modulation*. In spectroscopy of surface plasmons, angular or wavelength spectrum of an optical wave reflected from the sensor surface is measured and a shift in the resonant angle of incidence (sensor with angular modulation) or the resonant wavelength (sensor with wavelength modulation) is determined, Fig. 9a. In sensors with SPR intensity and phase modulation, monochromatic optical wave is made reflected under fixed angle of incidence and changes in its intensity (Fig. 9a) or phase (Fig. 9b) are measured, respectively. Currently, the most accurate method for measurement refractive index changes was reported using heterodyne measurement of SPR phase. This approach allowed discrimination of refractive index changes down to 2×10^{-7} refractive index units (RIU), [82]. Spectroscopy of surface plasmons-based sensors are capable to measure refractive index variations down to 3×10^{-7} RIU, [83]. SPR sensors with intensity modulation typically exhibit the accuracy in refractive index measurements of 10^{-5} RIU, [84].

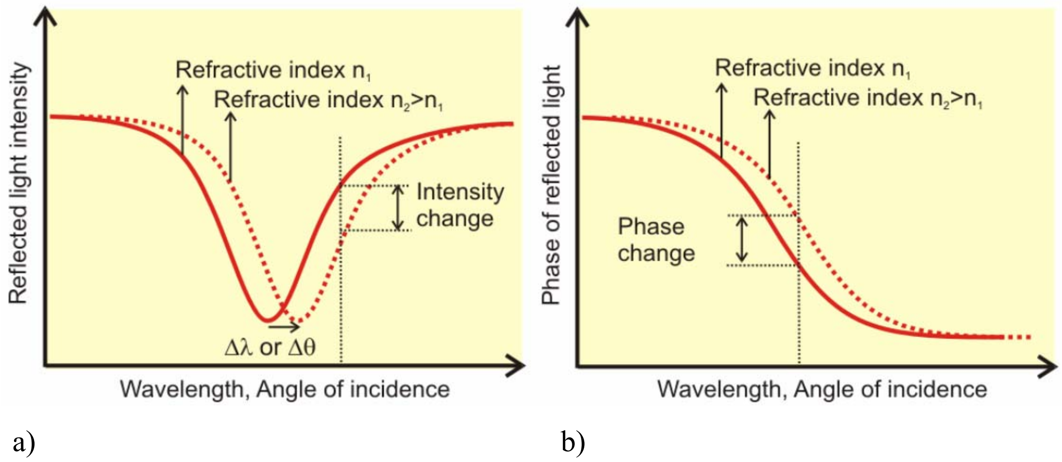

Fig. 9 SPR changes due to a refractive index variations in the angular or wavelength spectrum of reflectivity a) intensity and b) phase.

So far, various designs of SPR refractometers supporting SPR biosensors were developed:

Prism coupler employing the attenuated total reflection method in Kretschmann geometry has been used in SPR biosensors since the beginning of eighties [76] and it became the most common configuration in SPR biosensors. Up to now, numerous prism coupler-based SPR biosensors with intensity modulation [75], phase modulation [85], [86] and spectroscopy of surface plasmons relying on wavelength modulation [87] and angular modulation [88] were developed.

Fiber optics was introduced in SPR biosensors to offer miniature sensor probes, Fig. 10. In the nineties, intrinsic fiber optic biosensors using multi-mode [89], [90] and single-mode optical fibers [91], [92], [93] were carried out. In these biosensors wavelength modulation [89] and intensity modulation [90], [92], [93] was applied for measurement of SPR changes.

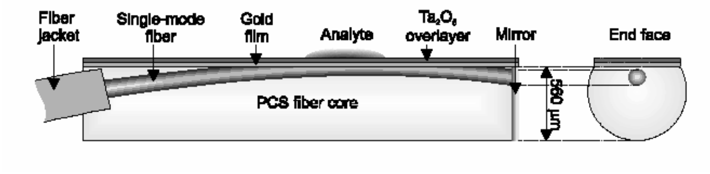

Fig. 10 SPR sensor probe with single mode optical fiber, reproduced from [93].

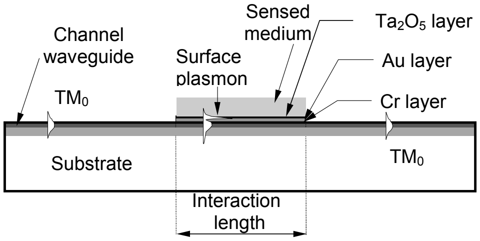

Fig. 11 SPR sensor with channel waveguide, reproduced from [35].

SPR sensors based on *integrated optics* (IO) were investigated due to possibility of straightforward integration of multiple optical components and multiple sensing channels on chip. The first SPR integrated optical sensor has been described in late eighties, [94] and over nineties SPR sensor with IO waveguides were explored more extensively [95]-[98]. This research has resulted in IO-SPR biosensor devices using intensity modulation [99] and wavelength modulation [35], see Fig. 11.

Although the early studies of SPR were closely associated to *diffraction gratings* [43], [44], these optical structures were exploited much less frequently in SPR biosensors than their prism coupler-based counterparts. The main reason for this lower activity is probably due to the more complex design and optimization necessary for the preparation of grating structures suitable for SPR sensing. In addition, as a disadvantage can be assumed that an optical wave has to pass through the sensed sample to excite SPW in diffraction grating-based SPR biosensor. The first SPR biosensor with diffraction grating was reported at the end of eighties [100], see Fig. 12. Lately, there were reported SPR sensors based on low-cost disposable diffraction gratings, [101] and [102]. These works pointed out an important benefit of diffraction grating-based SPR sensors – the possibility of using standard mass-production technologies such as hot embossing or injection molding [103] allowing potentially large-volume low-cost fabrication of sensors chips. So far wavelength [104] and angular [105], [106] modulation of SPR as well as intensity modulation [100], [101] was used in diffraction grating-based SPR biosensors.

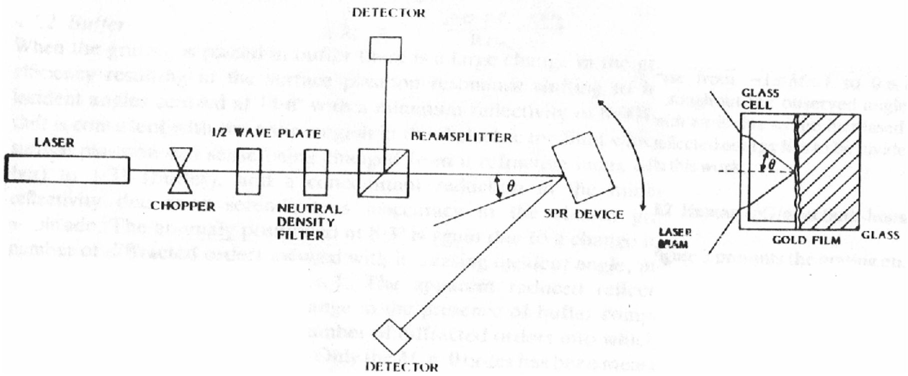

Fig. 12 SPR sensor with metallic diffraction grating, reproduced from [100].

1.2.3 Optical configurations used in multichannel SPR biosensors

As SPR refractometric systems are sensitive to integral refractive index changes in the evanescent field of SPW, SPR biosensors cannot distinguish specific binding of target analyte molecules to attached receptors from the non-specific response (e.g., due to binding of other molecules present in analyzed samples and from background refractive index changes caused by variations in temperature and overall composition of samples). Therefore SPR biosensors with measuring and reference channels were designed for compensating these effects. In addition, research in multichannel SPR biosensors was pursued due to the need for parallelized measurements.

Multichannel SPR biosensors with intensity modulation

In the group of intensity modulation-based SPR biosensors, SPR imaging [107] become common technique for measuring of SPR changes from an array of sensing channels [108], [84], [109]. In this approach, a monochromatic collimated light beam is reflected from a metal coated surface with two-dimensional array of sensing channels. In the cross-section of reflected beam, the intensity is spatially modulated due to the excitation of surface plasmons in each channel. Intensity changes originating from variations in SPR are simultaneously measured in each sensing channel by means of a spatially sensitive detector such as two-dimensional charge coupled device (CCD), see Fig. 13. Recently numerous biosensors based on SPR imaging with up to hundreds of sensing channels were reported, e.g. [84].

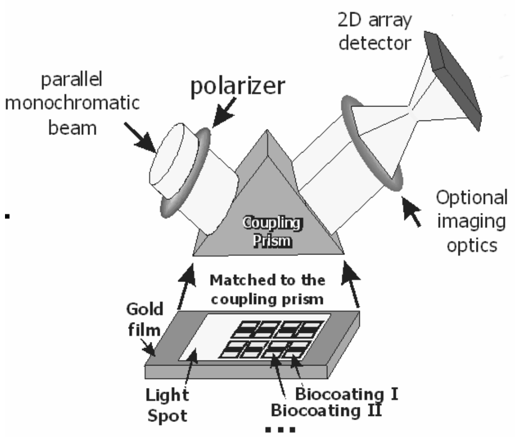

Fig. 13 Optical setup of SPR biosensor based on SPR imaging, reproduced from [109].

Multichannel SPR biosensors with spectroscopy of surface plasmons

Majority multichannel biosensors based on spectroscopy of surface plasmons rely on parallel architecture of sensing channels. In this architecture, multiple light beams exciting surface plasma wave in different sensing channels located in different areas on sensor chip are independently interrogated for SPR changes. In *prism coupler-based SPR biosensors* with *angular modulation*, series of convergent monochromatic beams are focused on a row of sensing channels and reflected light beams are projected on a position sensitive detector. By using different areas of the detector, angular reflectivity spectra are simultaneously measured from each sensing channel, Fig. 14. The first multi-channel SPR sensor system with angular modulation was developed in the beginning of nineties by BIAcore and it supported two [110] and later four [111] channels. In years following, the possibility of extending this approach up to ten channels was explored, [112].

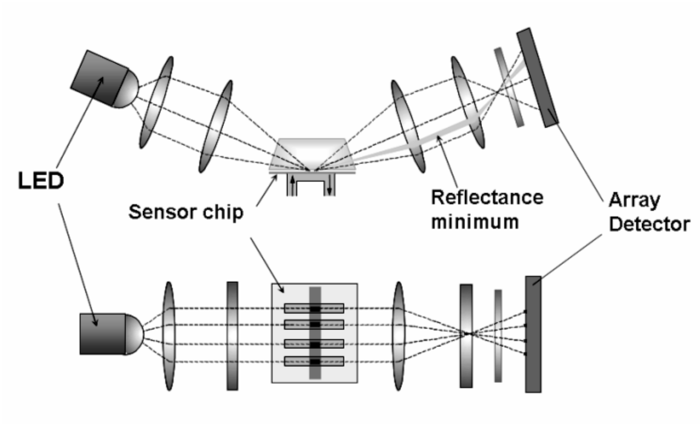

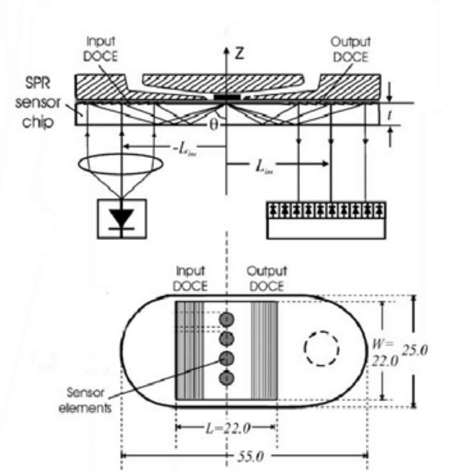

Fig. 14 Parallel architecture of sensing channels in sensor with angular modulation of SPR, reproduced from [111]. The optical arrangement consists of laser diode (LED), collimator, focusing lens, sensor chip, objective, cylindrical lens and polarizer.

Fig. 15 Parallel architecture of SPR sensing channels in sensor with angular modulation in geometry using diffractive optics coupling elements (DOCE), reproduced from [113].

A different approach for multichannel SPR sensor relying on the ATR method and angular modulation of SPR was reported by Thirstrup et al., [113]. As shows Fig. 15, employing an SPR sensor chip with diffractive optic coupling elements (DOCE) allows significantly reducing the complexity of SPR readout optics. DOCE elements embossed on the chip surface serve for coupling of a monochromatic beam into a sensor chip, in which series of converging beams are focused onto a linear array of sensing channels. Light beams reflected from the metal coated surface are projected onto a two-dimensional CCD detector by means of output DOCE. Using the CCD detector, angular SPR spectra are simultaneously measured from each sensing channel.

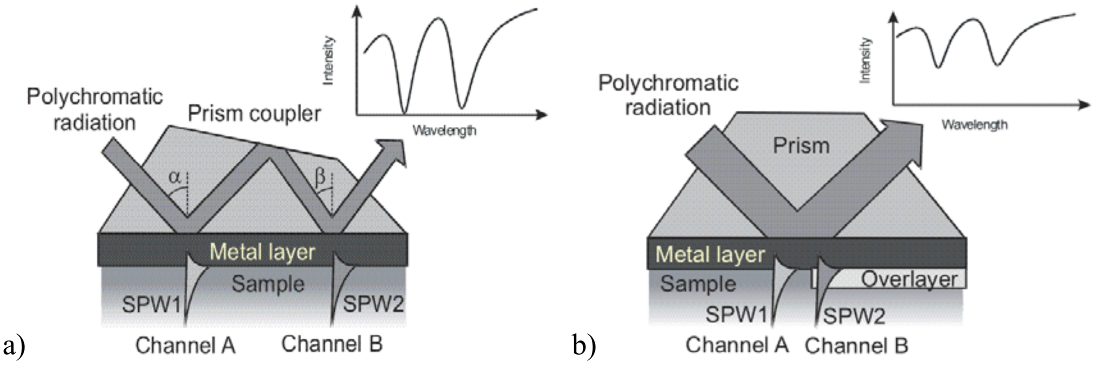

a) b)

Fig. 16 SPR dual-channel sensors based on WDM of sensing channels. a) WDM of sensing channels by means of altered angles of incidence. b) WDM of sensing channels by means of a high refractive index overlayer.

In *prism coupler-based SPR biosensors* with *wavelength modulation*, spectral analysis of multiple light beams is performed by multiple spectrographs [114] or by using an optical switch routing light from multiple sensing channels to a single spectrograph [115], see Fig. 17. In addition, wavelength division multiplexing (WDM) of sensing channels was utilized in wavelength modulation-based SPR biosensors. In this approach, SPR from multiple sensing channels is encoded at different wavelengths into a single polychromatic light beam analyzed with a spectrograph. The wavelength separation of SPR in different sensing channels achieved by altering the angle of incidence of the light beam in a special multi-reflection element [116] or by simultaneously illuminating areas with or without a dielectric overlayer [117] was reported, see Fig. 16. Lately, WDM multiplexing of sensing channels was combined with parallel architecture of sensing channels in a four-channel [118] and eight-channel [119] SPR biosensor.

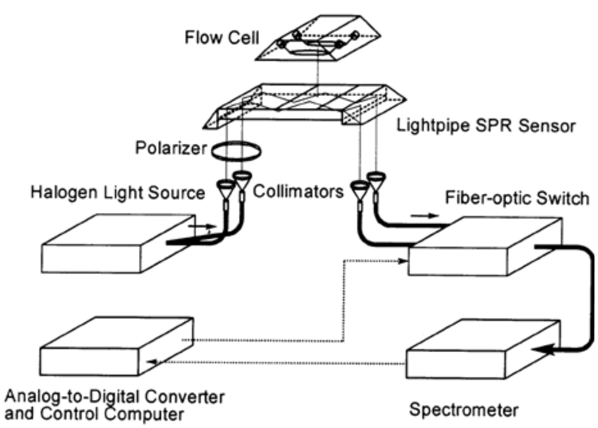

Fig. 17 Scheme of SPR biosensor with wavelength modulation and optical switch routing light from two channels to spectrograph, reproduced from [115].

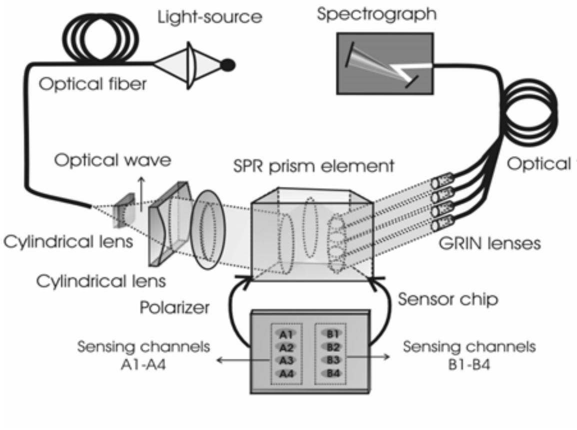

Fig. 18 Scheme of the optical system of eight-channel SPR sensor combining parallel architecture with the wavelength division multiplexing of serially-ordered channels, reproduced from [119].

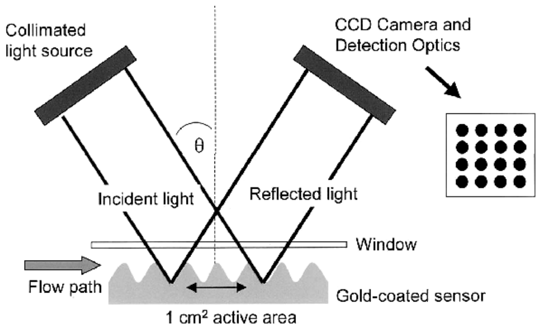

Fig. 19 Multichannel SPR sensor with an array of sensing channels on a sensor chip with diffraction grating, reproduced from [105].

Recently, SPR biosensor device based on *diffraction grating* with hundreds of channels has been reported, [105]. SPR changes in each channel are determined from angular reflectivity spectrum acquired by sequential scanning of SPR images at different angles of incidence, see Fig. 19. This sensor system is currently available under name FlexiChip from BIAcore Inc. A different approach allowing for screening of two-dimensional array of sensing channels with diffraction grating is the subject of this thesis. The herein presented approach is based on the SPR sensor system in which angular SPR spectra are measured from hundreds of sensing channels with the use of spatial and time multiplexing, [106].

1.2.4 Patterning of protein arrays and sample delivery on SPR sensor chip

In SPR biosensors, appropriate biorecognition elements need to be immobilized on the surface of metal-coated sensor chip. Recently gold is preferably used as SPR-active metal as it is stable and numerous methods for the attachment of biomolecular recognition elements are available. Up to now, immobilization of biomolecular recognition elements on gold using physical adsorption [120], [121], affinity binding [78], [122] or covalent binding [123], [124] in form of monolayers [77], [78], [120] or into a three-dimensional dextran matrix [124] were reported, see Fig. 20. In order to exploit the benefit of parallel monitoring of multiple biomolecular interactions in multichannel SPR biosensors, different recognition elements have to be attached to different areas on the sensor chip. For spatial resolved immobilization of arrays biomolecules on planar surfaces, methods including microfluidic networks (μFN) [125], [126] micro-contact printing (μCP) [127], [128], [129], contact spotting [130], electron beam patterning [131] and photoactive patterning [132] were prospected.

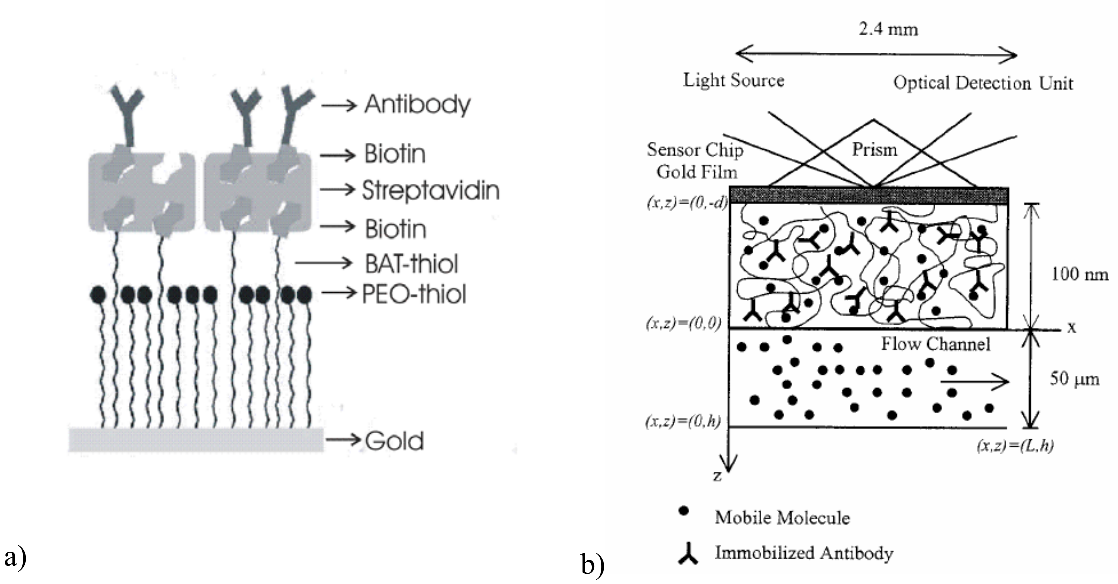

Fig. 20 Biomolecular recognition elements attached at gold surface in form of a) single layer attached using a thiol linker (reproduced from [133]) and b) into a three-dimensional dextran matrix (reproduced from [134]).

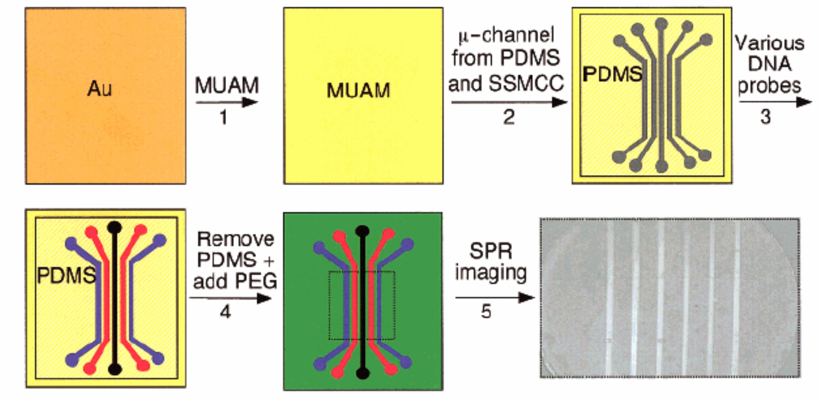

Fig. 21 PDMS microfluidic channels on the top of the SPR sensor surface, reproduced from [126].

In order to distribute analyzed samples to sensing channels on a sensor chip, SPR biosensors are combined with a fluidic system. The first SPR biosensor with integrated fluidic system was introduced in the beginning of nineties by BIAcore Inc., [110]. This microfluidic system was based on a plastic molded cartridge with integrated valves and loop extensions. Later, SPR sensor with microfluidic channels prepared by photolithography was reported, [135]. Also, since the end of the last decade, microfluidic systems molded in a poly(dimethylsiloxane) (PDMS), [136], [137] has become common in SPR biosensors [138], [112], [139], see Fig. 21.

1.3 Modeling of surface plasmon resonance on diffraction gratings

Up to now, various analytical [141], [142] and numerical methods (e.g. integral method [48], finite difference time domain [143], modal method [144], rigorous coupled wave analysis [145]) were exploited for modeling of surface plasmon resonance on periodic metallic structures such as diffraction gratings. Analytical approaches were proved offer physical insight into studied problem. However, these theories are typically valid only for a narrow range of studied parameters and their complexity is substantially increasing when studying structures with arbitrary surface modulations, multilayer structures or gratings with deep modulations. Therefore, we used numerical approaches based on rigorous coupled wave analysis (RCWA), integral method (IM) and eigen-mode expansion method (EEM) for simulation of SPR on diffraction gratings. In this section, these three apparoaches are briefly introduced.

In RCWA and IM methods, the grating geometry is laterally divided into three regions, see Fig. 22. The region I consists of a semi-infinite dielectric medium above the metal grating surface, region II encompasses periodic corrugated surface between a metal and dielectric with the modulation depth *h* and in the region III contains semi-infinite metal medium.

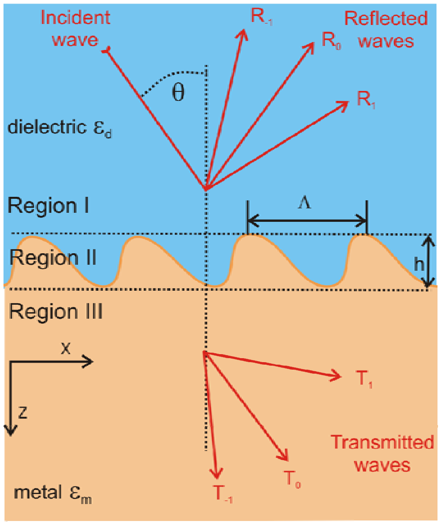

Fig. 22 Geometry of a grating structure with decomposition of electromagnetic field into reflection and transmission terms.

Further let us use Cartesian coordinates with the *z* axis perpendicular to the grating surface and *y* axis parallel to grating grooves. In addition, let us assume a monochromatic plane wave impinging from the region I at the periodic corrugated surface of the metallic grating with the plane of incidence defined by axis *x* and *z*. According to Floquet theorem, electromagnetic field in the studied geometry can be expressed in series (1.6) and (1.7) in the region I and III, respectively. These equations describes the solution for TM polarization (with its magnetic intensity vector $\vec{H}$ is parallel to the grating surface). The theory can be analogously built for the complementary transverse electric (TE) polarization (electric intensity vector $\vec{E}$ is parallel to the grating surface) as well.

$$H_y^I = \exp\left[-j\left(k_{x0}x + k_{z0}z\right)\right] + \sum_p R_p \exp\left[-j\left(k_{xp}x + k_{zpI}z\right)\right], \tag{1.6}$$

$$H_y^{III} = \sum_p T_p \exp\left[-j\left(k_{xp}x + k_{zpIII}z\right)\right], \tag{1.7}$$

$$K = \frac{2\pi}{\Lambda}, \tag{1.8}$$

$$k_{x0} = \frac{2\pi}{\lambda}\sqrt{\varepsilon_d}\sin\theta, \tag{1.9}$$

$$k_{z0} = \frac{2\pi}{\lambda}\sqrt{\varepsilon_d}\cos\theta, \tag{1.10}$$

$$k_{xp} = k_{x0} + pK, \tag{1.11}$$

$$k_{zpI} = \sqrt{\varepsilon_m - k_{xp}^2}, \tag{1.12}$$

where $j = \sqrt{-1}$, H_y^I and H_y^{III} is the magnetic intensity field in the region I and III, respectively, λ is the wavelength, θ is the angle of incidence of the plane wave impinging the grating surface and p is an integer. The first term in RHS of Equation (1.6) describes the field of the incident plane wave and the second term represents reflected waves expanded into the reflection diffraction orders with complex amplitudes R_p. Equation (1.7) describes the field transmitted through the grating structure expanded into transmission orders with amplitudes T_p. Reflection and transmission terms are coupled with the incident wave through diffraction in the region II. The reflection and transmission coefficients R_p and T_P can be determined from the solution inside the region II. This solution can be obtained using various numerical methods including the integral method [146], [147], [148] [149] and differential methods based on RCWA [150], [151], modal method [152], [153] and coordinate transformation method [154].

1.3.1 Rigorous coupled wave analysis

In the differential method, the permittivity and magnetic intensity $\vec{H} = \left(0, H_y\left(x, y, z\right), 0\right)$ inside the interface region II is expanded to series (1.13) and (1.14), respectively.

$$\varepsilon_{II}\left(x, z\right) = \varepsilon\left(x + \Lambda, z\right) = \sum_p \varepsilon_p\left(z\right)\exp\left(jpKx\right), \tag{1.13}$$

$$H_y^{II} = \sum_p U_p\left(z\right)\exp\left[-j\left(k_{xp}x + k_{z0}z\right)\right]. \tag{1.14}$$

The field inside the region II fulfills the wave equation (1.15), which together with boundary conditions (1.16)-(1.19) applied at the borders of regions I and III for *z=0* and *z=h* forms a complete set of equations describing the problem.

$$\Delta H_y^{II} - \left(\frac{\nabla\varepsilon}{\varepsilon}\cdot\nabla\right)H_y^{II} + k_0^2\varepsilon\left(x, y\right)H_y^{II} = 0, \tag{1.15}$$

$$H_y^{II}\Big|_{z=0} = H_y^{I}\Big|_{z=0}, \tag{1.16}$$

$$H_y^{II}\Big|_{z=h} = H_y^{II}\Big|_{z=h}, \tag{1.17}$$

$$\frac{1}{\varepsilon}\frac{\partial H_y^{II}}{\partial z}\Bigg|_{z=0} = \frac{1}{\varepsilon}\frac{\partial H_y^{I}}{\partial z}\Bigg|_{z=0}, \tag{1.18}$$

$$\frac{1}{\varepsilon}\frac{\partial H_y^{II}}{\partial z}\Bigg|_{z=h} = \frac{1}{\varepsilon}\frac{\partial H_y^{III}}{\partial z}\Bigg|_{z=h}. \tag{1.19}$$

When expressions (1.6), (1.7), (1.13) and (1.14) are substituted into Equations (1.15)-(1.19), an infinite set of second-order linear differential equations for coefficients R_p, T_p and $U_p(z)$ is obtained. Two methods can be used to numerically solve this set of (exact) coupled wave equations for coefficients R_p, T_p and $U_p(z)$ - *state-variables method* [151] or *modal method* [152]. Both these methods can treat arbitrary grating profile by approximating the diffraction grating profile with a stack of lamellar gratings (multilayer approximation). In state-variables method the set of second-order differential Equations (1.15)-(1.19) is rewritten in form of first-order differential equation which is truncated at a certain number of orders $N<p<N$ and numerically solved. In the modal method the solution is found in terms of modal field expansion connected across the stack using boundary conditions.

1.3.2 Integral method

In the integral method, a different approach is used to solve the electromagnetic field expanded to series with coefficients R_p and T_p in the regions I and II, respectively. In this method the total field solution is expressed as the superposition of an incident field E^{inc} (1.20) and diffracted field E^{diff}, which is assumed to be generated by a surface current $\vec{J}$ (1.21) flowing on the grating surface. This surface current is induced by the incident optical wave E^{inc} and it is determined by the Helmholtz equation (1.22). Further let us illustrate the principle of integral method for TE polarization (TM polarization can be treated analogously).

$$E_y^{inc} = \exp\left[-j\left(k_{x0}x + k_{z0}z\right)\right], \tag{1.20}$$

$$\vec{J}\left(x,y\right) = \left(0, j_e\delta\left(z - f(x)\right), 0\right), \tag{1.21}$$

$$\left[\Delta + k_0^2\varepsilon\left(x,z\right)\right]\left(E_y^{inc} + E_y^{diff}\right) = -j\omega\mu_0 J_y, \tag{1.22}$$

where δ is the Dirac delta function and j_e is the current density at the grating surface. Based on Equation (1.22), the diffracted field in the region I can be written in form of Helmholtz-Kirchoff integral (1.23). In this equation, the integration is done over one period of the modulation described by the function *f(x)*. $G^+\left[x,x',z,f\left(x'\right)\right]$ defined by Equation (1.24) is the upper half space Green function and $\Psi\left[x',f\left(x'\right)\right]$ (1.25) is an unknown function representing transformed current density j_e.

$$E_y^{diff} = \int_{\Lambda} G^+\left[x,x',z,f\left(x'\right)\right]\Psi\left[x',f\left(x'\right)\right]dx', \tag{1.23}$$

$$\begin{aligned} G^{+}\left(x,x',z,f\left(x'\right)\right) &= \exp\left(jk_0x\right)\times \\ &\times\left\{\sum_{-\infty}^{\infty}\exp\left[jKn\left(x-x'\right)+j\gamma_n^{+}\left|z-f\left(x'\right)\right|\right]/\gamma_n^{+}\right\}/\left(2i\Lambda\right), \end{aligned} \qquad (1.24)$$

$$\Psi\left[x',f\left(x'\right)\right]=-i\omega\mu_0 j_e\delta\left(x-x'\right)\delta\left(z-f\left(x'\right)\right)\exp\left(-ik_{x0}x'\right)\left\{1+\left[f\left(x'\right)\right]^2\right\}^{1/2}, \quad (1.25)$$

where $\gamma_n^{+}=\sqrt{k_0^2\varepsilon_I-k_{xn}^2}$. The unknown function $\Psi\left[x',f\left(x'\right)\right]$ can be solved using the boundary conditions at the grating surface. These conditions lead to an integral equation from which the function $\Psi\left[x',f\left(x'\right)\right]$ can be expressed as a function of E^{inc} and *f(x)*. This function can be solved numerically for truncated number of harmonics in the expansion of Green function (1.24). After the Ψ is solved, the diffracted field is obtained from Equation (1.23). The integral method was further extended for solving of multilayer diffraction grating structures, [155].

1.3.3 Eigen-mode expansion method

In the eigen-mode expansion method, the studied (two-dimensional) structure is perpendicularly divided into a stack of planar waveguides, see Fig. 23. These waveguides are enclosed between perfectly electric (PEC) or magnetic conductive (PMC) mirrors to discretize the spectrum of eigen-modes in transverse electric (TE) or transverse magnetic (TM) polarization, respectively. In addition, absorbing or perfect matched layer (PML) layers can be placed between the waveguide structure and PEC/PMC to avoid light reflection of electromagnetic field back into the studied structure [156]. In each waveguide in the stack, the set of eigenmodes is found. The optical wave entering the structure is expressed as a linear combination of these eigenmodes and using the overlap integrals this field is propagated through the structure. Based on this approach, the electromagnetic field in the whole structure as well as the field reflected or transmitted through the structure can be calculated using the transmission and reflection matrix.

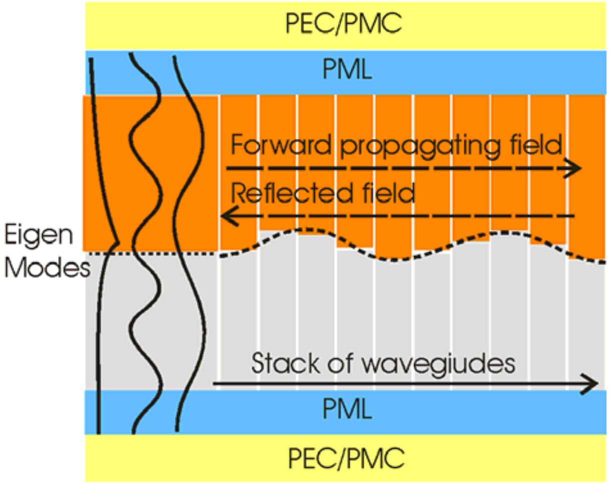

Fig. 23 Geometry of a stack of waveguides approximating the grating structure between perfectly matched layers (PML) and perfect electric / magnetic conductor (PEC / PMC).

2 Research goals

It is the aim of this work to develop an SPR sensor platform for high-throughput screening of biomolecular interactions. This goal is pursued by exploiting surface plasmon resonance on diffraction gratings (see Fig. 24). For SPR biosensors, diffraction gratings offer numerous advantages including the flexibility in design of the sensor optical system, avoiding the optical matching of the sensor chip to a coupler and the potential for economical fabrication of sensor chips from plastics using mass production-compatible technologies such as injection molding or hot embossing.

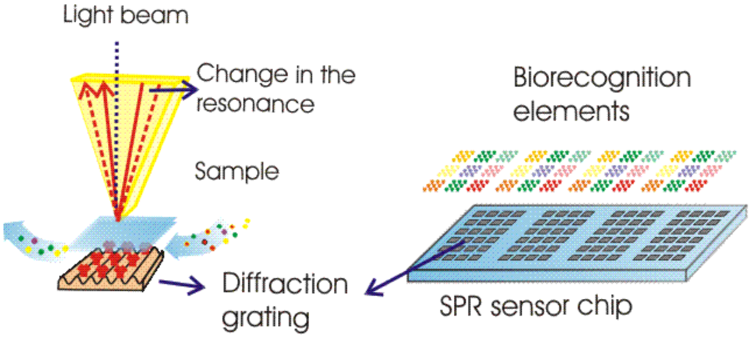

Fig. 24 SPR sensor chip with an array of diffraction grating and its optical readout using angular modulation of surface plasmon resonance.

The herein pursued SPR sensor platform relies on a sensor chip with a two-dimensional array of metallic diffraction gratings. Each diffraction grating serves as an independent sensing channel with a built-in coupler for excitation of surface plasmons, see Fig. 24. Biomolecular interactions occurring on the surface of each channel are detected using angular spectroscopy of surface plasmons. The reflectivity spectra from the array of sensing channels are determined using a convergent light beam scanned across rows of diffraction gratings (spatial and time multiplexing of sensing channels).

The presented work encompasses theoretical and experimental study of diffraction-coupled SPR and its implementation in an SPR sensor. In the theoretical part of the work, numerical methods are evaluated for simulation of SPR on diffraction gratings ("Numerical simulations of SPR on diffraction gratings", Chapter 3.1). Then, key parameters of diffraction gratings affecting the excitation of a SPW and its sensitivity to refractive index changes are investigated ("Diffraction coupling to surface plasma wave" and "SPR sensitivity to refractive index changes", Chapters 3.2 and 3.3, respectively) and diffraction gratings are optimized for SPR biosensing ("Analysis of diffraction grating-based SPR biosensor", Chapter 3.4). In the experimental part of the work, SPR sensor device is developed. First, diffraction grating structures with different modulation profiles and depths are prepared ("Preparation of diffraction gratings", Chapter 4.1) and characterized ("Surface plasmon resonance on diffraction gratings", Chapter 4.2). Then a prototype SPR sensor device including a diffraction grating-based SPR sensor chip, fluidic system and SPR chip reader is developed ("SPR sensor device with an array of diffraction gratings", Chapter 4.3). The main performance characteristics of the sensor device are determined ("Characterization of the SPR sensor refractometer", Chapter 4.4) and its applicability for biomolecular interaction analysis is demonstrated ("Application of the SPR sensor device to biosensing" Chapter 4.5).

3 Theory

In this section, numerical methods for simulation of SPR on diffraction gratings are evaluated. These methods are further used for investigation of key parameters of diffraction gratings affecting the excitation of SPW and its sensitivity to refractive index changes on grating surface. On the ground of this study, optimization of diffraction gratings for SPR biosensor applications is carried out.

3.1 Numerical simulations of SPR on a diffraction grating

Three numerical methods for simulation of SPR on diffraction gratings were used: *rigorous coupled wave analysis* (RCWA), *modified integral method* (IM) and *eigen mode expansion method* (EEM). The RCWA model was embodied in software *GSolver* (from Grating Solver Development, Inc., USA, [157]), IM in *PCGrate-S* software (from International Intellectual Group, Inc., USA, [158]) and EEM in *Cavity Model Framework* (CAMFR, developed by Peter Bienstman, University of Gent, [159]).

3.1.1 Rigorous coupled wave theory (RCWA)

As follows from Chapter 1.3.1, the most important parameters affecting the accuracy and convergence of RCWA method are the number of layers approximating the grating modulation and the number of diffraction orders at which the expansion of electromagnetic field is truncated. To demonstrate typical convergence and stability of RCWA, an optical response from a model diffraction grating was calculated while varying these parameters. For this purpose, we used the diffraction grating of which parameters are specified in Tab. 1. We excited SPW in the geometry shown in Fig. 25 with a plane wave with the wavelength of 830nm impinging at the grating.

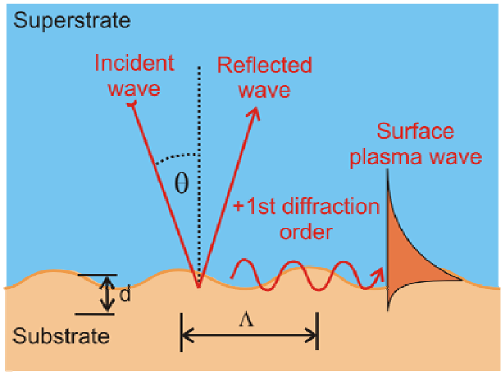

Fig. 25 Excitation of surface plasma wave on periodically corrugated surface of a metallic diffraction grating.

Modulation profile	Sinusoidal
Modulation period	Λ=907 nm
Modulation depth	d=25 nm
Superstrate	n=1.33 RIU
Substrate	Gold
Wavelength	Λ=830 nm
Polarization	TM

Tab. 1 Parameters of model diffraction grating structure and optical wave.

The performed analysis revealed that the number of layers 10 was sufficient for approximating the modulation of diffraction grating. For this number of layers, the convergence and stability of calculated reflectivity was explored for an increasing number of diffraction orders. In this study, the angle of incidence was fixed at the edge of SPR dip (θ=21.5 deg) and the reflectivity was calculated for two slightly different grating parameters (grating modulation period 907 nm and 907.1 nm was used). When taking into account only the stable solutions (the ones for which a small change of the grating parameters slightly alters the reflectivity), we can observe that the reflectivity fluctuates with the standard deviation of 3% for the number of diffraction orders above 25, see Fig. 26a. The whole angular spectrum with SPR absorption dip centered at the angle of incidence 20.8 deg for number of diffraction orders of 20, 30 and 40 are shown in Fig. 26b.

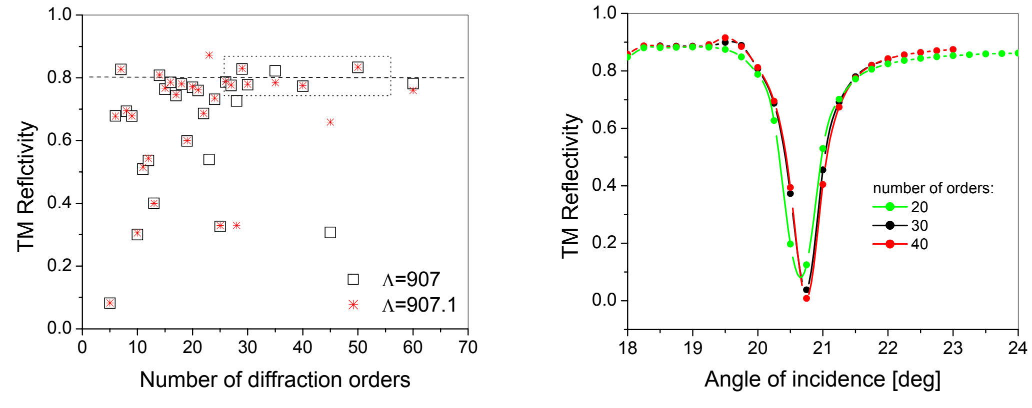

a) b)

Fig. 26 a) TM reflectivity of the grating structure as a function of number of diffraction orders, grating modulation period Λ=907 nm and 907.1 nm, angle of incidence θ=21.5 deg, wavelength λ=830 nm; b) Angular TM reflectivity spectrum for number of diffraction orders 20, 30, and 40 and for the wavelength of 830 nm.

Clearly, for a low number of diffraction orders (<20) the convergence of the RCWA method embodied in GSolver was found insufficient. For high number of diffraction orders (>25), the method yields results with the error of 3 % (standard deviation of reflectivity) but exhibits poor stability. The computation time was typically in order of tens of minutes for a single reflectivity value (using a PC with 500MB RAM and 1.6GHz CPU).

3.1.2 Integral method (IM)

Stability and accuracy of IM was explored for the identical configuration as in the previous section (Tab. 1 and Fig. 25). In IM embodied in the PC-Grate software, the most important parameter affecting the accuracy and convergence is the number of collocation points. This parameter determines the number of terms, into which the Green function is expanded (see Chapter 1.3.2). Similarly to the previous chapter, the stability and convergence was evaluated by calculating the dependence of reflectivity on the number of collocation points for two slightly different grating parameters. Obtained results presented in Fig. 27a reveal excellent stability and convergence for number of collocation points higher than 50. The fluctuation of the reflectivity when changing the number of collocation points exhibited standard deviation smaller than 0.01% for the number of collocation points around 100. For the number of collocation points of 100, the calculation of single reflectivity value required tens of seconds (using a PC with 500MB RAM and 1.6GHz CPU).

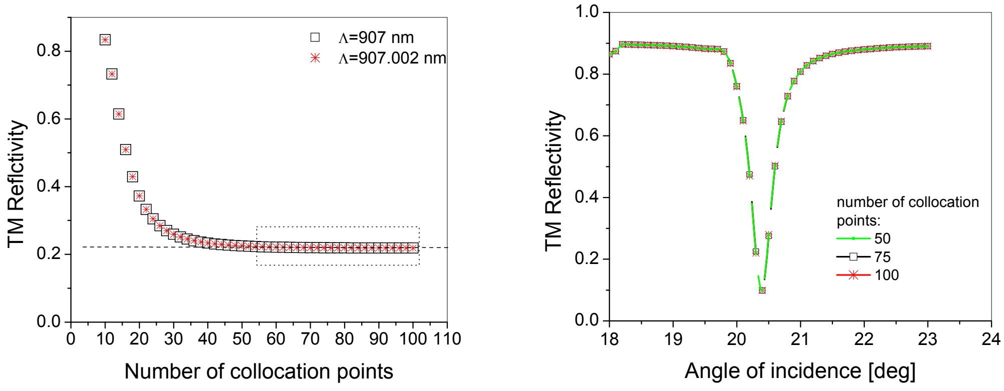

a) b)

Fig. 27 a) TM reflectivity of the grating structure as a function of number of collocation points for the grating modulation period Λ=907 and 907.002 nm, angle of incidence θ=20.3 deg, wavelength λ=830 nm; b) Angular TM reflectivity spectrum for number of collocation points 50, 75, and 100 and the wavelength of 830 nm.

3.1.3 Eigen mode expansion method (EEM)

The EEM can not be directly applied for the geometry used in the previous two chapters in which a plane wave was made incident on the infinite metallic grating structure. The reason is that in EEM method the diffraction grating has to be of a finite size. Furthermore, an optical field can be launched into the structure only from the sides as above and below the grating structure perfectly magnetic conductive and perfectly matched layers are placed (see Chapter 1.3.3). Therefore, in order to compare SPR resonance obtained by EEM to the ones calculated with previous models, diffraction out-coupling of SPW into an optical wave propagating in the dielectric adjacent to the grating was explored. We assumed the grating structure with the length and width of 45 µm and 25.2 µm, respectively, ad the (average) thickness of the metal and dielectric of 0.3 µm and 24.9 µm, respectively. The diffraction grating parameters stated in Tab. 1 were approximated by a periodic stack of waveguides in which each period was divided into n_{seg} sub-waveguides with the width Λ/n_{seg} (Λ is the grating period). Inside the stack of waveguides electromagnetic field was expanded into N_{modes} eigen modes. The PML layer with the thickness of 0.6 µm was placed at the top and bottom of this structure. For such grating structure, the convergence of electromagnetic field transmitted through the grating structure was explored for different n_{seg} and N_{modes}. The coupling efficiency of SPW to the spectrum of plane waves propagating in the dielectric was obtained using the transmission matrix.

The spectrum of coupling efficiency of SPW to series of plane waves propagating at the end of the grating structure was calculated for n_{seg}=2 and 8 and N_{modes}=50 and 25. The calculated spectra exhibit a peak in the coupling efficiency centered at the angle of 21 deg which matches the position of the SPR dip in the reflectivity obtained from RCWA and IM (Fig. 26b and Fig. 27b). However, the angular width of the resonance calculated with EEM is almost an order of magnitude broader when comparing with RCWA and IM. The reason is that the width of the diffraction grating structure is too small. In addition, electromagnetic field distribution inside the grating structure (n_{seg}=8 and N_{modes}=50) was calculated to illustrate the coupling of SPW to a plane wave in the dielectric. Obtained Fig. 29a and Fig. 29b with the electromagnetic field distribution of SPW propagating in the structure with and without the modulation of the metal surface, respectively, clearly shows the effect of diffraction grating out-coupling of SPW to a plane wave.

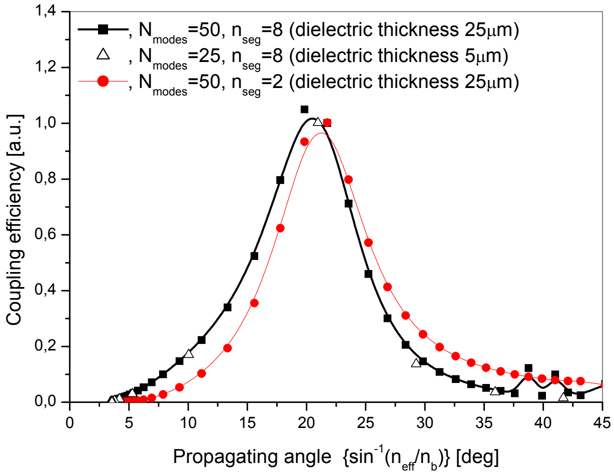

Fig. 28 Efficiency of coupling of SPW into the plane wave modes as a function of the angle of incidence.

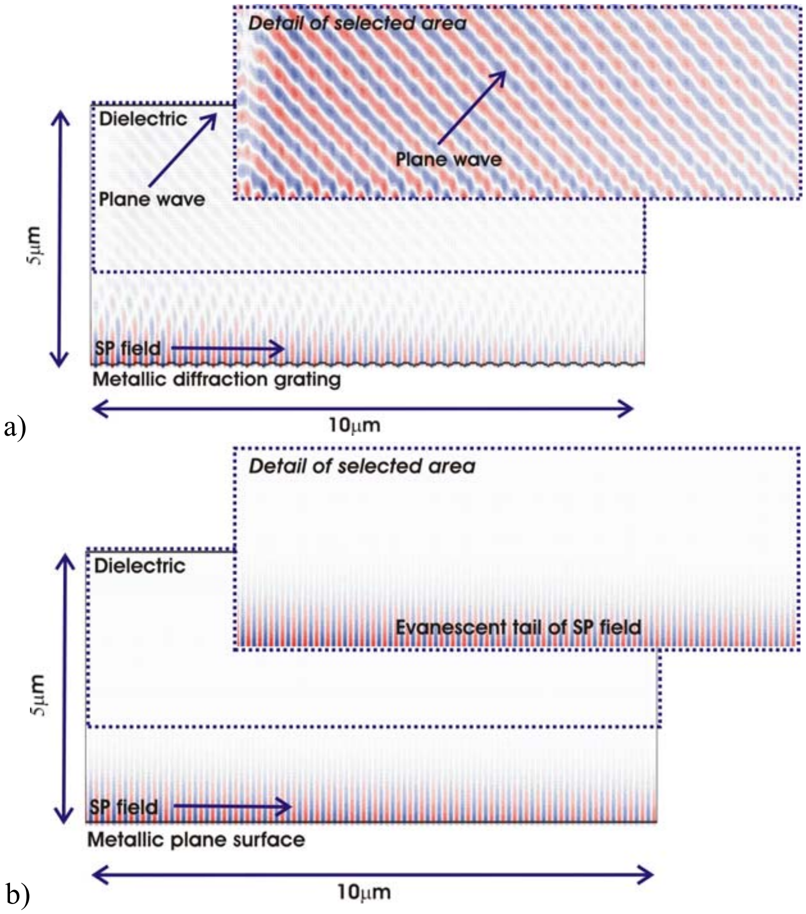

Fig. 29 Magnetic intensity distribution of field propagating through the grating structure with SPW propagating for a) diffraction coupling of SPW into an optical wave propagating above grating, b) without diffraction coupling into an optical wave at plane metal dielectric interface; red and blue regions corresponds to opposite phase.

Performed analysis revealed that EEM is, in principle, capable of simulating SPR on diffraction gratings. However, its applicability for simulation of larger structures supporting higher number of modes is limited. For such geometries, the solver can miss modes and the computation time dramatically increases.

3.1.4 Comparison of numerical models with analytical theory

In order to verify results obtained from IM and RCWA numerical methods, let us compare them with the analytical theory presented in Chapter 1.1.3. In this study, we used the geometry in which an optical wave is incident on a metallic diffraction grating where it couples to SPW through the first diffraction order, see Fig. 25. The parameters of the diffraction grating geometry are stated in Tab. 2.

Grating modulation profile	Sinusoidal
Grating modulation period	Λ=455 nm
Grating modulation depth	d=12.5-50 nm
Substrate	Gold
Superstrate	Water
Angle of incidence	0 deg
Polarization	TM

Tab. 2 Parameters of the diffraction grating structure used in simulations.

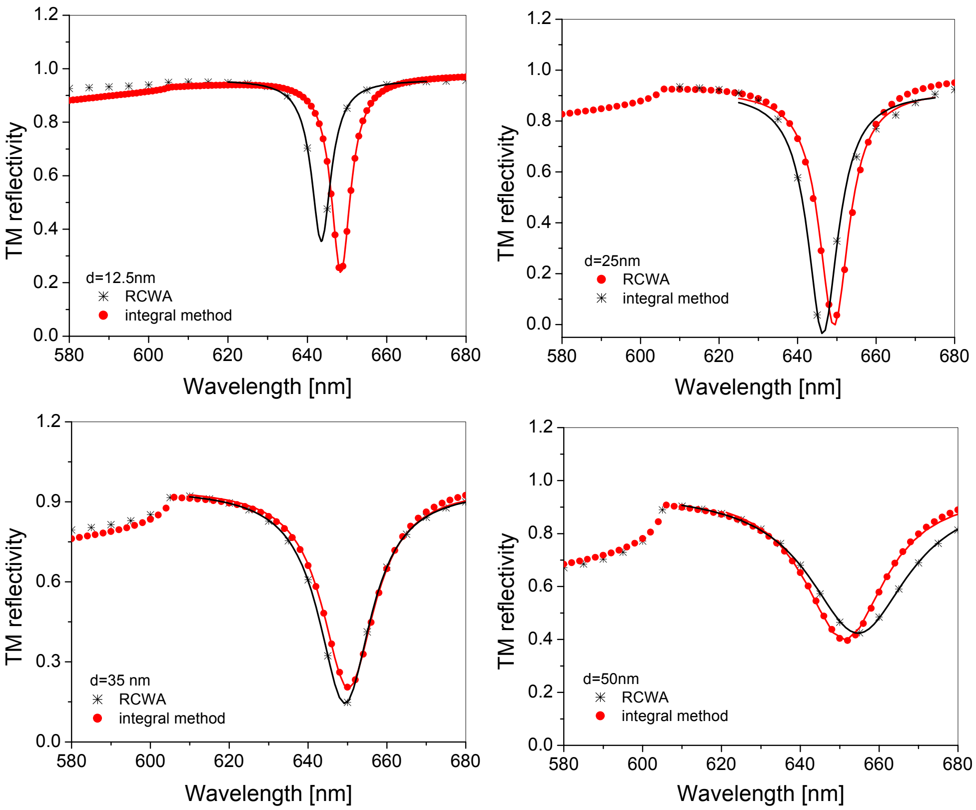

Fig. 30 Comparison of IM and RCWA methods – wavelength TM reflectivity from grating structure specified in Tab. 2, the grating modulation depth d=12.5, 25, 35 and 50nm. Lines show Lorentzian fits of SPR dips.

From this diffraction grating with the modulation depth in the range from 12.5 to 50 nm, wavelength TM reflectivity spectra were calculated for normal incident light by using IM and RCWA method. Obtained results shown in Fig. 30 reveal that the difference between SPR wavelengths calculated by IM and RCWA is smaller than 4 nm, the average difference in the full width in half minimum of SPR dips and in the depth of SPR dips is 5 per cent. In addition, calculated SPR absorption dips were showed an excellent agreement with Lorentzian function as predicted by the analytical theory [48].

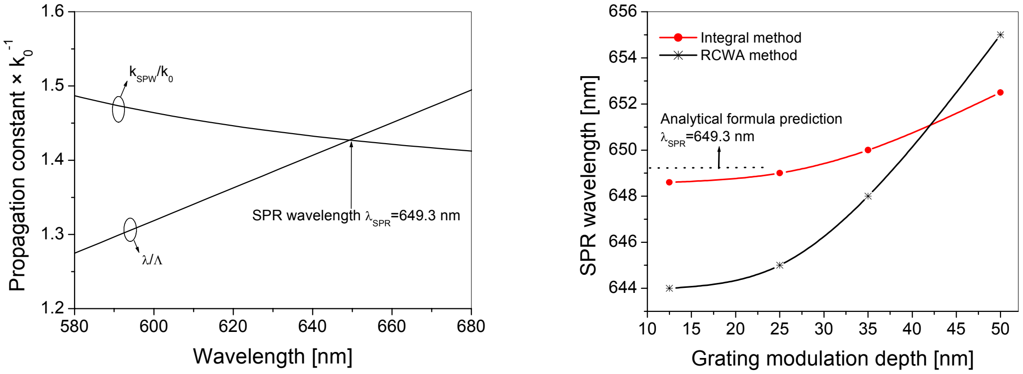

a) b)

Fig. 31 a) Matching of SPW propagation constant with the one of on incident optical wave, b) dependence of SPR wavelength on the grating modulation depth; diffraction grating specified in Tab. 2.

For metallic diffraction gratings with shallow surface modulations, dispersion relation of SPW holds the one for plane metal surface and thus SPR wavelength obtained from numerical methods match the one from the phase-matching condition (see Equation (1.5) and Fig. 31a). As shown in Fig. 31b, the SPR wavelength of 648.6 nm and 644 nm was calculated using IM and RCWA, respectively, for the grating modulation depth d=12.5 nm. These values agree well with SPR wavelength 649 nm obtained from the phase-matching condition (1.5). Furthermore, results depicted in Fig. 31b exhibit quadratic dependence of SPR wavelength on the grating modulation depth which is in accordance with the analytical theory, [48].

3.1.5 Numerical simulations of SPR on diffraction gratings - summary

Performed analysis of integral method (IM, embodied in software PCGrate-S from International Intellectual Group, Inc., USA) and RCWA method (embodied in software G-Solver from Grating Solver Development, Inc., USA) revealed that both these models are capable of simulation of SPR on metallic diffraction gratings. These models provide almost identical parameters of far-field distribution of electromagnetic radiation coupled with SPW on a metallic grating. Obtained results agreed with the analytical theory. Further, IM is preferably used in the following calculations as it offers the advantage of better stability, convergence and shorter computing times. In addition, eigen-mode expansion method (EEM, embodied in CAMFR software developed by Peter Bienstman, University of Gent) was investigated for calculating of both near-field and far-field distribution of electromagnetic fields. We showed that EEM results of far-field distribution agree with IM and RCWA method, however the exact solution was difficult to obtain as too large structure would need to be defined for which this method is not appropriate.

3.2 Diffraction coupling to surface plasma wave

In the following part of this work, key parameters of diffraction gratings affecting the coupling of an optical wave and a SPW are analyzed. These include the diffraction grating period, modulation depth and profile of the surface modulation, and optical constants of materials forming the grating structure.

Herein, we shall focus on the geometry depicted in Fig. 25. In this geometry an optical wave is incident through a dielectric with the refractive index of water at the gold grating where it couples to SPW through plus first or minus first diffraction order. The coupling of an optical wave to a SPW is investigated in wavelength and angular spectrum of reflectivity. SPR wavelength spectrum is studied for the angle of incidence θ=0 and the angular spectrum for the fixed wavelength and angles of incidence near the normal incidence. The angle of incidence under which the grating is illuminated is taken in the air. Optical constants of used materials are stated in Appendix.

3.2.1 Diffraction grating modulation period

When a light beam is incident on a diffraction grating with the period Λ, the component of its propagation constant that is parallel to the grating surface can be increased or decreased by multiples of $2\pi/\Lambda$ (see Chapter 1.1.3). On metallic gratings, this phenomenon allows enlarging the momentum of an optical wave necessary for its coupling to SPW. As was demonstrated in Chapter 1.1.3, the coupling between these waves occurs when the condition (1.5) is fulfilled. This condition interrelates the angle of incidence and the wavelength for which resonant interaction between an optical wave and a SPW occurs for certain grating period Λ and diffraction order p. By using this equation, we calculated the dependence of SPR wavelength and SPR angle incidence on the grating period for fixed angle of incidence (see Fig. 32a) and fixed wavelength (see Fig. 32b), respectively. These results shows that for shallow semi-infinite gold grating on which SPW dispersion relation is not significantly affected by the surface modulation, the plus and minus first diffraction order resonance overlap in the normal incidence geometry. When the angle of incidence is not zero, two separate resonances occur.

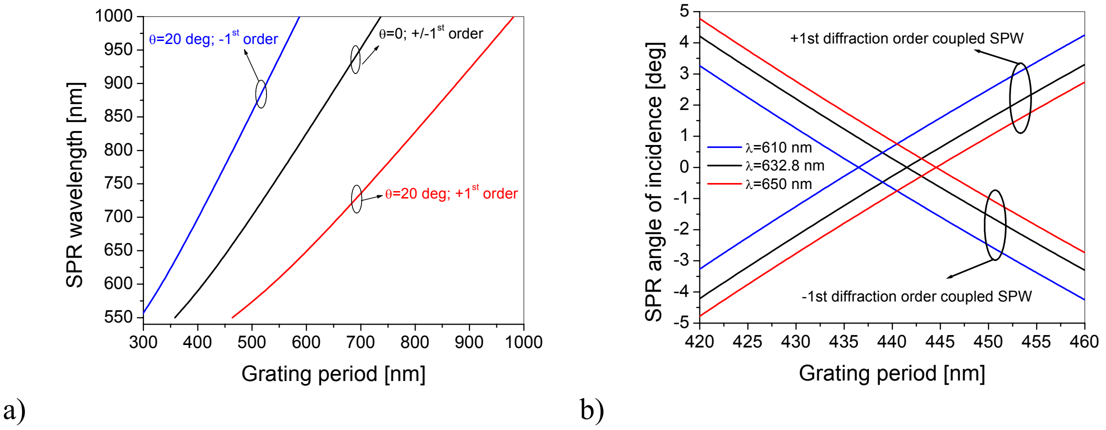

Fig. 32 a) The dependence of SPR wavelength on the diffraction grating period Λ for θ=0 deg and θ=20 deg, b) the dependence of SPR angle of incidence on Λ for wavelengths λ=610, 632.8 and 650 nm; SPW is excited in the interface between gold and water.

3.2.2 Diffraction grating modulation depth

The most important parameter influencing the strength of diffraction coupling between an optical wave and a SPW is the grating modulation depth. In order to analyze this effect, SPR reflectivity wavelength spectrum (for θ=0 deg) and angular spectrum (for wavelength λ=633 nm and angle of incidence in the range θ=0-5 deg) was calculated for sinusoidal diffraction grating with different modulation amplitudes a_1 and modulation period Λ=455 nm (parameters of the diffraction grating are summarized in Tab. 2). As shown in Fig. 33a and Fig. 33b, an increasing grating depth leads to a decrease in the SPR dip minimum until the incident wave is totally coupled to SPW. The total coupling of an optical to SPW is manifested as a zero reflectivity at the minimum of SPR dip. When increasing the grating depth above the value for which total coupling to SPW occurs, the resonance becomes over-coupled and the SPR reflectivity minimum is increasing. In normal incidence geometry, the zero reflectivity occurs at the wavelength of 650 nm for the grating depth of 20 nm. When a SPW is excited under a slightly different angle of incidence θ=3 deg, the zero reflectivity occurs for deeper grating with the depth of 35 nm. This reason for this change is the fact that in normal incidence geometry both plus and minus first diffraction orders simultaneously couple with SPW. For slightly different angle of incidence, the resonance is split and the interaction with SPW is mediated through plus first or minus first diffraction orders individually.

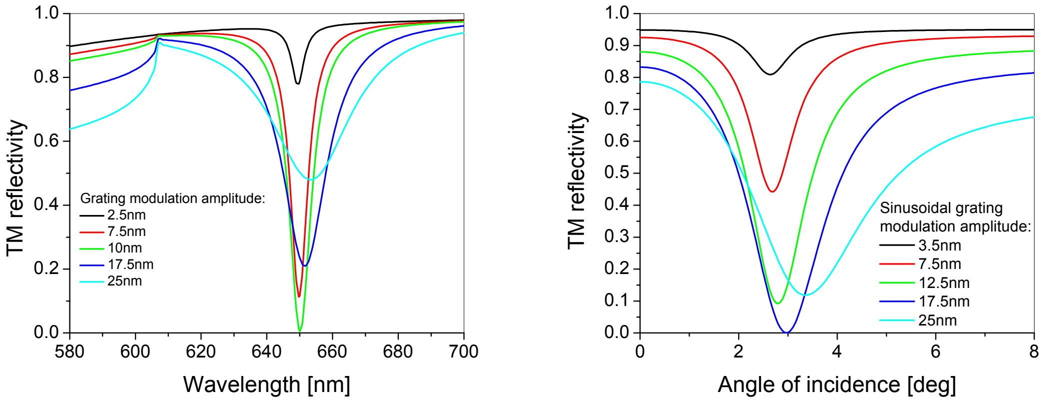

a) b)

Fig. 33 TM reflectivity from sinusoidal diffraction grating: a) wavelength spectrum, angle of incidence θ=0 deg, b) angular spectrum, wavelength λ=633nm; parameters of the diffraction grating stated in Tab. 2.

The grating depth of a sinusoidal grating allowing full coupling of light to a SPW (optimum grating depth) is dependent on the wavelength. This dependence is calculated for both angle of incidence θ=0 and 5 deg. Obtained results plotted in Fig. 33 reveal that dependence of the optimum grating modulation depth exhibits a minimum centered at the wavelength of 800 nm. The occurrence of the minimum can be elucidated as follows. When increasing damping of a SPW, the optimum grating modulation depth increases as a SPW can interact with an optical wave along shorter distance and thus for its full coupling stronger diffraction interaction (i.e. higher grating depth) is required. As follows from Equation (1.3), damping of SPW described with the imaginary part of its propagation constant $\mathrm{Im}\{k_{SPW}\}$ is proportional to the imaginary part of metal permittivity $\mathrm{Im}\{\varepsilon_m\}$. For gold grating used in presented calculations, $\mathrm{Im}\{\varepsilon_m\}$ exhibits the minimum at the wavelength of 800 nm (see Fig. 91).

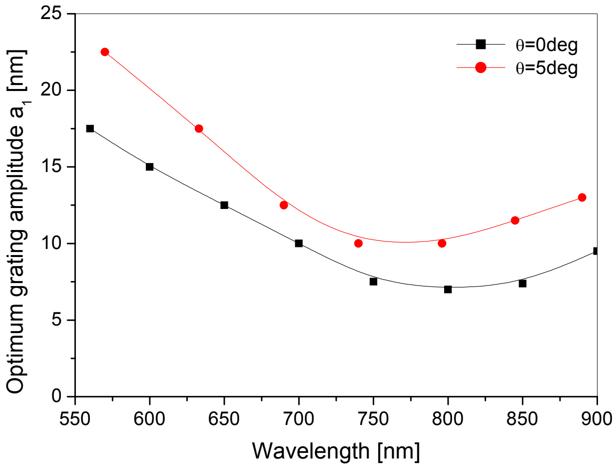

Fig. 34 The grating modulation amplitude allowing full coupling of incident light to a SPW as a function of wavelength for angle of incidence θ=0 and 5 deg; parameters of sinusoidal diffraction grating stated in Tab. 2.

3.2.3 Diffraction grating with a general modulation profile

In general, the interaction of SPW and an optical wave can be altered by varying the grating modulation profile. In order to explore this effect, let us expand the modulation profile in the Fourier series:

$$f(x)=\sum_{p=1}^{\infty} a_p \sin\left(pKx+\phi_p\right), \tag{3.1}$$

where $K=2\pi/\Lambda$ is the fundamental frequency, a_p and φ_p are the amplitude and the phase of p^{th} spatial harmonic, respectively. First, let us investigate gratings in which only first two amplitudes a_1 and a_2 are non-zero. Moreover, let us restrict this study to diffraction gratings with mirror symmetry in which the phase difference is equal to $\phi_2-\phi_1=\pi/2$ or $3/2\pi$. As shown in Fig. 35, introduction of the amplitude a_2 in the expansion of grating modulation gives rise to a grating with "narrow valley" and "narrow peak" profiles for phase differences φ_2-$\varphi_1=\pi/2$ and φ_2-$\varphi_1=3/2\pi$, respectively.

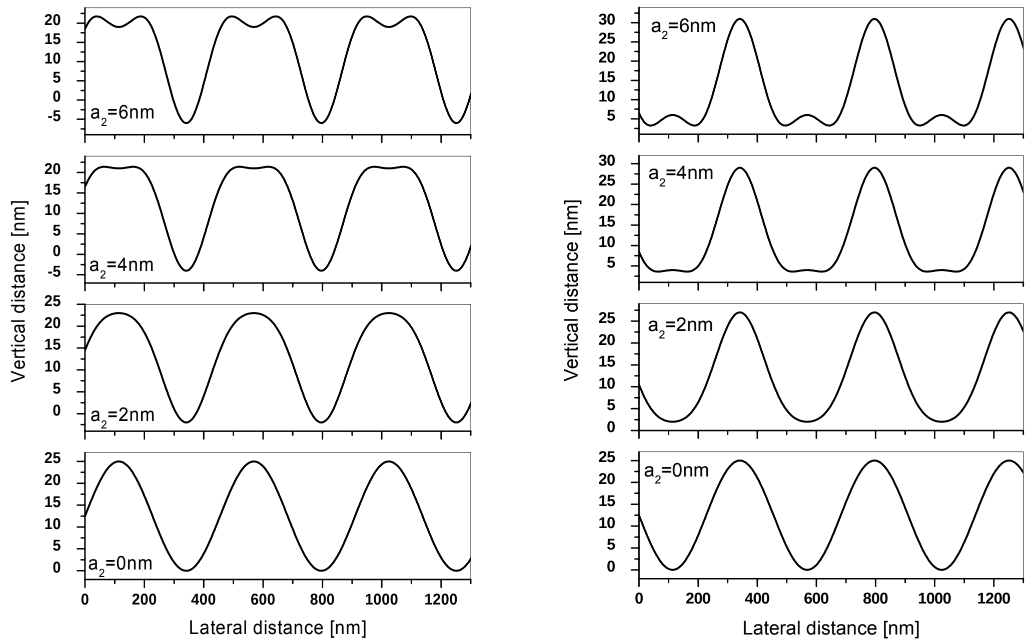

a)

b)

Fig. 35 Diffraction grating profile for: a_1=10 nm, a_2=0-6 nm, Λ=455 nm, a) $\varphi_2-\varphi_1=\pi/2$ – “narrow valley“ profile, b) $\varphi_2-\varphi_1=3/2\pi$ - “narrow peak” profile.

SPR reflectivity from gratings with “narrow valley“ and “narrow peak“ profiles were calculated in either angular spectrum (λ=633 nm) and wavelength spectrum (angle of incidence θ=0 deg). Results in Fig. 36 suggest that for the grating with “narrow valley” profile and the angular spectrum, SPR dip shifts to lower angles of incidence and the coupling to SPW decreases when increasing the amplitude a_2. For the diffraction grating with “narrow peak” profile, SPR dip shifts to lower angles of incidence and the coupling to SPW increases when increasing amplitude a_2. In the wavelength spectrum presented in Fig. 37, we observe a shift of SPR dip towards shorter / longer wavelengths for “narrow peak” / “narrow valley” profile with increasing the amplitude a_2, respectively.

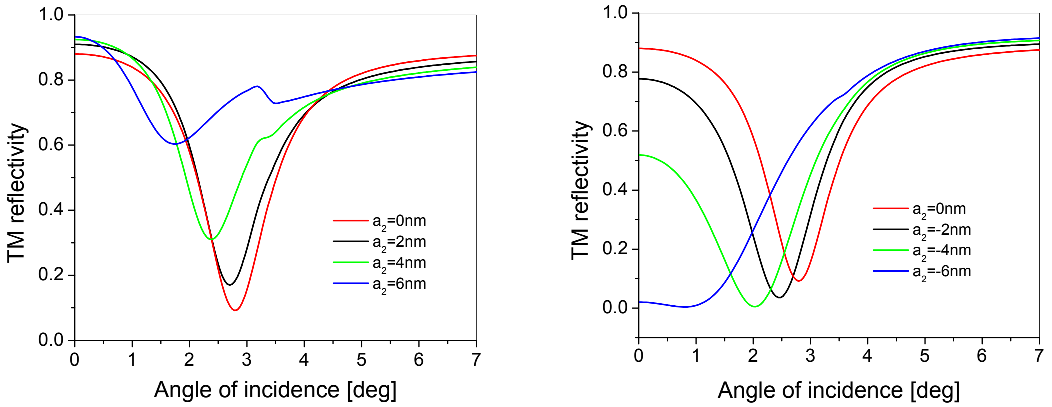

a)

b)

Fig. 36 Change in SPR angular spectrum when increasing amplitude a_2 for a) $\varphi_2-\varphi_1=\pi/2$ “narrow valley” profile, b) $\varphi_2-\varphi_1=3/2\pi$ “narrow peak”, a_1=10 nm, Λ=455 nm, wavelength 633 nm.

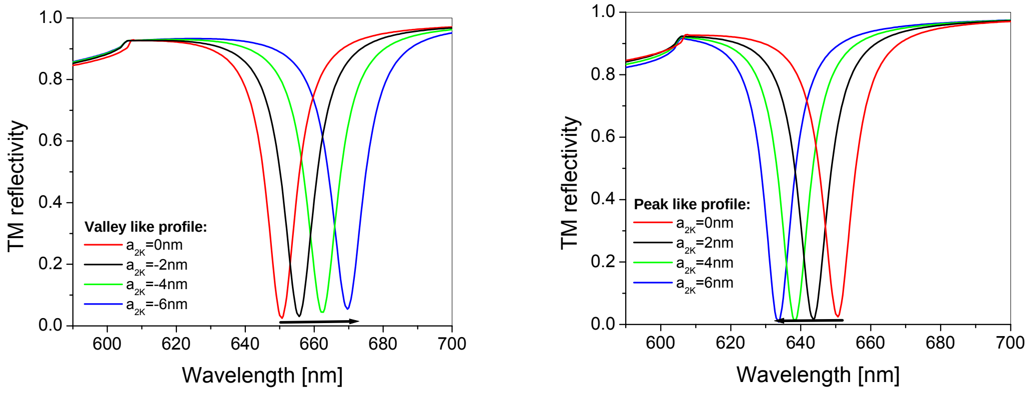

a)

b)

Fig. 37 Change in SPR wavelength spectrum when increasing amplitude a_2 for a) φ_2-φ_1=$\pi/2$ “narrow valley” like profile, b) φ_2-φ_1=$3/2\pi$ “narrow peak”, a_1=10 nm, Λ=455 nm, angle of incidence θ=0 deg.

Observed changes in SPR spectra are related to the occurrence of Bragg scattering of counter-propagating SPWs on the grating modulation with the amplitude a_2. This scattering leads to a split in the dispersion relation of SPW as the plasmonic bandgap opens up, [66]. The width of the bandgap can be analytically expressed by Equation (3.2) which was adopted from [67].

$$\Delta\lambda = \mathrm{Re}\left\{\frac{4\lambda^3(2K)^2 a_2\left(1-\frac{7}{2}(2Ka_2)^2\right)}{4\pi^2\sqrt{-\varepsilon_m\varepsilon_d}}\right\}. \tag{3.2}$$

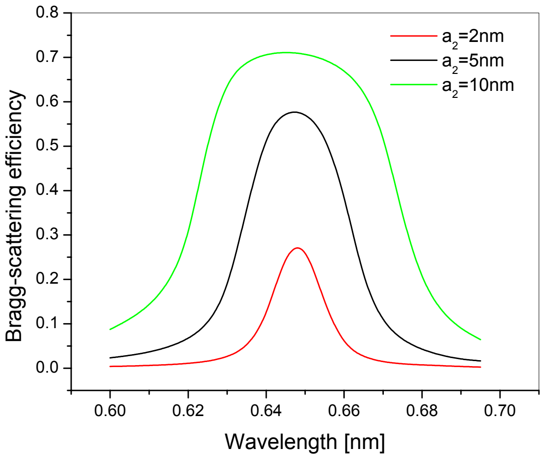

Fig. 38 Wavelength spectrum of Bragg scattering efficiency of SPW on diffraction grating calculated for the amplitude a_2=2, 5 and 10 nm, Λ=455 nm.

In order to illustrate the occurrence of the bandgap, we calculated the wavelength spectrum of Bragg scattering efficiency (defined as the square ratio of amplitude of SPW mode entering the grating and the amplitude of back-reflected SPW) for the amplitudes a_1=0 and a_2=2, 5 and 10 nm. Results obtained by using the EEM method which are presented in Fig. 38 show that when the magnitude of a_2 increases the Bragg scattering occurs over a wider range of wavelengths centered at the wavelength 650 nm. On edges of the bandgap, new SPW eigen-modes arise: a) at the *shorter wavelength* standing SPW mode localized in *peaks* of the harmonic modulation with the amplitude a_2 and b) at the *longer wavelength* standing SPW mode localized in *valleys* of the harmonic modulation with the amplitude a_2. The field distribution of Bragg scattered SPW modes were calculated by EEM for the a_2=5 nm (see Fig. 39). These results show that the mode at longer wavelength exhibits the field distribution more confined at the grating surface while the one at the lower wavelength is stretched further into the dielectric.

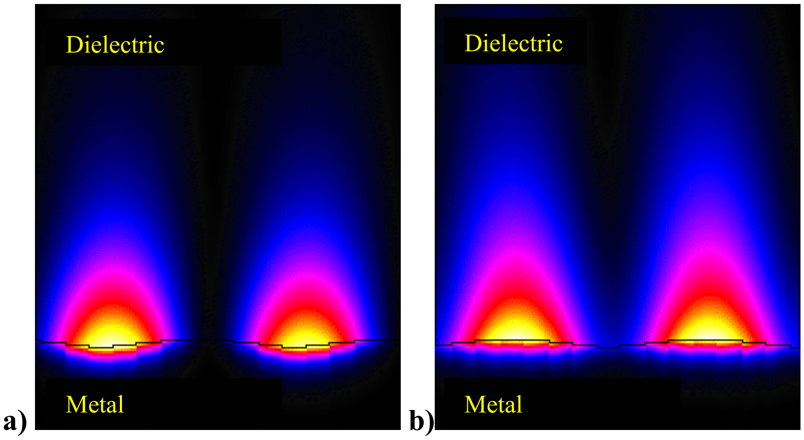

Fig. 39 Magnetic intensity distribution of SPW at the wavelengths on edge of the photonic bandgap, a) wavelength 635 nm, b) wavelength 665 nm, a_2=5nm; horizontal and vertical size of the structure is 455 nm and 500 nm, respectively.

On mirror-symmetric diffraction gratings, either shorter wavelength-SPW mode ("narrow peak" profile) or longer-wavelength SPW mode ("narrow valley" profile) can be excited, see Fig. 37. The reason for this behavior is because minima or maxima of the modulation with amplitude a_2 (where Bragg-scattered modes can be excited) are located at peaks or valleys of the "narrow peak" and "narrow valley" diffraction grating, respectively (see Fig. 35). As the electric intensity vector of the incident wave (TM polarized, angle of incidence θ=0) is parallel to the grating surface at grating peaks and valleys, light cannot excite the Bragg-scattered SPW mode with its electric intensity vector perpendicular to the grating surface [67]. On mirror-symmetric gratings, only modes located on slopes of the diffraction grating modulation profile can be excited in normal incidence geometry.

In the angular spectra, the shift to shorter angle of incidence and a decrease / an increase in the depth of SPR dip is observed for "narrow valley profile" / "narrow peak profile". It is caused by transition of the SPR wavelength in or out of the SPW bandgap. These effects are illustrated by the sketch of SPW dispersion relation in the vicinity of the SPW bandgap (see Fig. 40a).

The dependence of the bandgap width on the amplitude a_2 was calculated with IM and RCWA as the spectral distance between SPR reflectivity dips for gratings with the phase φ_2-φ_1= $\pi/2$ and $3\pi/2$ (see Fig. 37), and by EEM method as the FWHM of the scattering efficiency wavelength band (see Fig. 38). From obtained results shown in Fig. 40b, the slope of the bandgap width shift induced with an increase of the amplitude a_2 was calculated as 7.5, 8.8 and 5.0 for and IM, RCWA and EEM numerical methods, respectively. These values agree with the slope of 6.2 calculated with the analytical Equation (3.2).

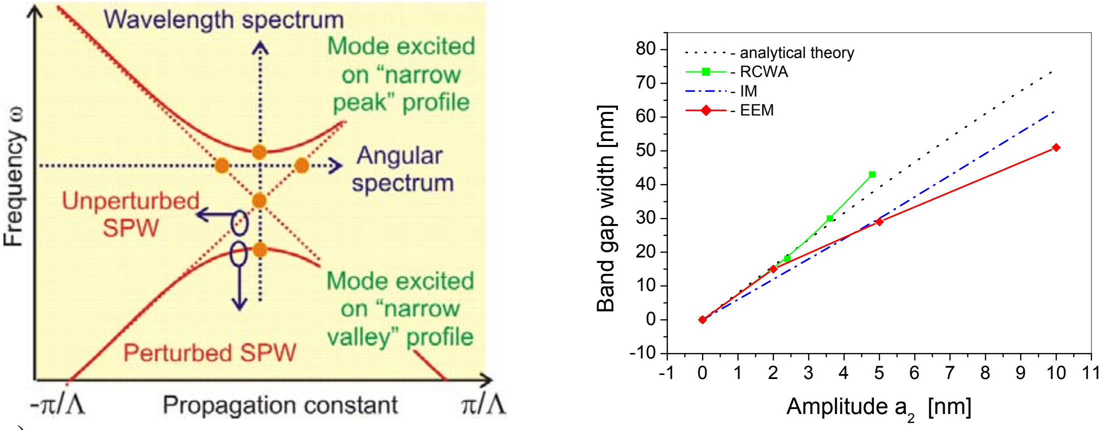

a)

b)

Fig. 40 a) SPW dispersion relation in the vicinity of the Bragg scattering bandgap a_1=0 nm, a_2=5 nm, Λ=455 nm; b) SPW bandgap width versus amplitude a_2 – comparison of IM, RCWA and EEM model and analytical theory.

In order to determine the effect of other higher harmonics in the Fourier expansion of the grating surface modulation (2.1), a shift in the resonance wavelength in the normal incidence geometry was calculated for increasing amplitudes a_2, a_3 and a_4. Results of this study presented in Fig. 41 show that amplitude a_3 and a_4=5 nm induce smaller shift in the SPR wavelength than the a_2 of the same magnitude. In addition, these data indicate that the diffraction coupling of SPWs and an optical wave via modulation components with amplitudes a_3 and a_4 is of higher perturbation order as the dependence of SPR wavelength shift exhibits higher order polynomial behavior. For more information on these effects see also [160].

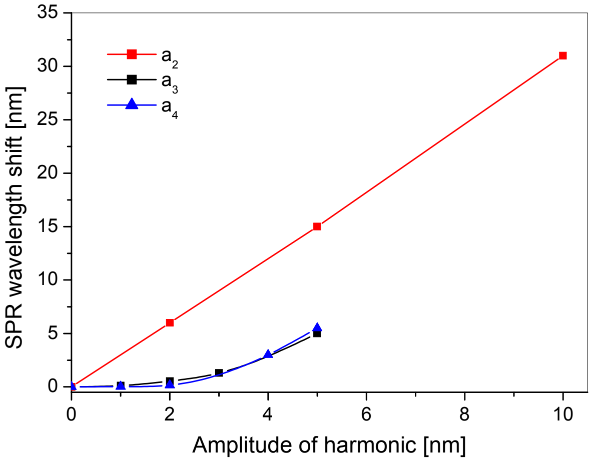

Fig. 41 Comparison of SPR wavelength shift induced by of higher spatial frequencies in the Fourier spectrum of the grating modulation, phase shift between the fundamental spatial frequency is of π/2, a_1=10 nm, Λ=455 nm, angle of incidence θ=0 deg.

3.2.4 Diffraction grating with finite thickness of the metal layer

So far, we assumed diffraction gratings consisting of semi-infinite metal and dielectric. In this section, let us investigate more realistic geometry in which the diffraction grating is composed of a periodically modulated metal layer of finite thickness h sandwiched between two seminfinite dielectrics (see Fig. 42). Semi-infinite superstrate dielectric ($n_d^2=\varepsilon_d$=1.776 at the wavelength 633 nm), gold metal layer, bottom substrate dielectric ($n_s^2=\varepsilon_s$=2.25 at the wavelength 633 nm) and sinusoidal modulated interfaces (amplitude a_1=12.5 nm and the period Λ=455 nm) are assumed. Similarly to previous study, an optical wave propagating in the superstrate dielectric is coupled to a SPW at the upper metal surface through first diffraction order.

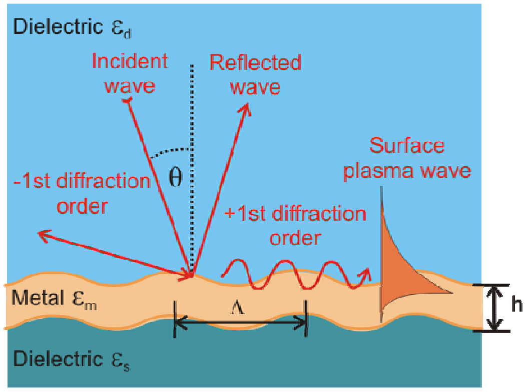

Fig. 42 Geometry of excitation of SPW on a diffraction grating with finite thickness metal layer.

At an interface between a semi-infinite metal and a dielectric, the field of SPW evanescently decays in both these media. However, when the semi-infinite medium is replaced with a metal layer of finite thickness, SPW mode can penetrate through this layer and become a leaky mode [161]. In order to investigate this effect, we calculated the field profile and the propagation constant of a SPW propagating on the interface between the metal and superstrate dielectric by using transfer matrix method [162] (the periodic modulated interfaces were replaced with plane interfaces). Obtained results presented in Tab. 3 reveal that the real part SPW propagation constant Re$\{k_{SPW}\}$ decreases with the gold layer thickness while its imaginary part increases. As shown in Fig. 43, these changes are accompanied with coupling of SPW to an optical wave in the substrate. Consistently with these data, numerical simulations of SPR reflectivity presented in Fig. 44a and Fig. 44b reveal that SPR angle and SPR wavelength decreases and the SPR dip width increases with gold layer thickness. In addition, from Fig. 44a and Fig. 44b follows that for the thickness of metal layer higher than 100 nm the interaction of SPW with the substrate dielectric is negligible and the SPR reflectivity is identical to the one obtained from grating the with semi-infinite metal.

h=20 nm	k_{SPW}=1.402 + 0.059j
h=30 nm	k_{SPW}=1.418 + 0.034j
h=50 nm	k_{SPW}=1.430 + j0.014j
h=100 nm	k_{SPW}=1.435 + 0.0079j

Tab. 3 Propagation constant of SPW guided on gold slab with thickness 20, 30, 50 and 100 nm between dielectrics with refractive indices 1.33 and 1.5, wavelength 633 nm.

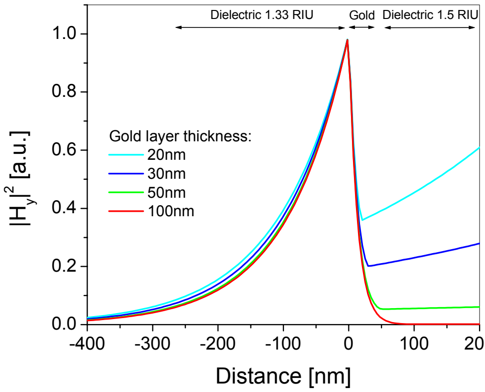

Fig. 43 **Profiles of magnetic intensity of a SPW guided by a gold layer with thickness 20, 30, 50 and 100 nm; wavelength 633 nm.**

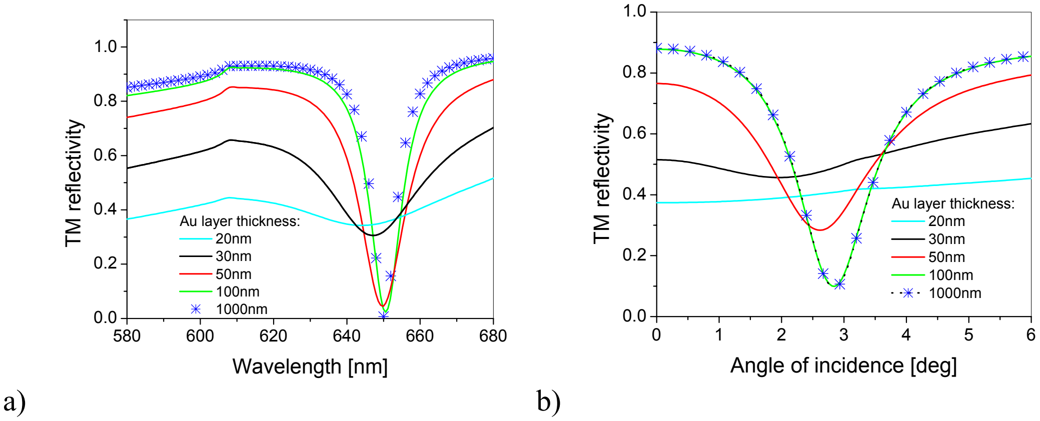

a) b)

Fig. 44 **SPR reflectivity spectra from diffraction grating with the thickness of gold layer 20, 30, 50 and 100 nm sandwiched between dielectrics with refractive index 1.33 and 1.5; sinusoidal modulation with period Λ=455 nm, amplitude a_1=12.5 nm; a) wavelength spectrum for angle of incidence θ=0 deg; b) angular spectrum for the wavelength 633 nm**

3.3 SPR sensitivity to refractive index changes

In this chapter, sensitivity of SPR on diffraction grating to variations in the refractive index is investigated. SPR sensitivity to two types of refractive index changes is explored: a) refractive index changes in a thin dielectric film on grating surface and b) refractive index changes in the whole dielectric adjacent to the grating surface. SPR changes induced by these refractive index variations are studied by using analytical theory and obtained results are compared with numerical simulations.

As shown in Fig. 45, the studied geometry consists of a substrate (refractive index n_s=1.5), gold layer (thickness h=100 nm), a thin dielectric film (refractive index n_f=1.5, thickness in the range ρ=0-10 nm) and superstrate (n_d=1.33). Parameters of the diffraction grating structure are specified in Tab. 4. Changes in SPR wavelength and SPR angle of incidence induced by refractive index variations δn_d and δn_f are calculated for normal incidence geometry or for small angles of incidence $\theta^2 << 1$ (θ in radians).

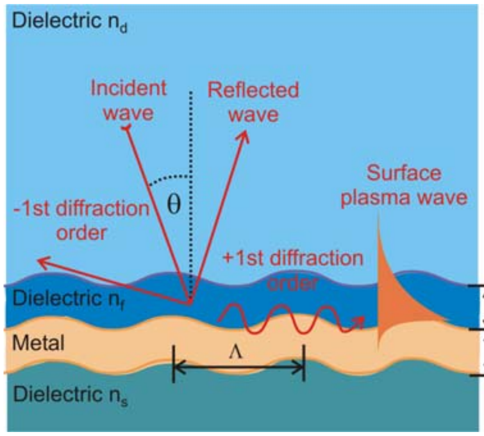

Fig. 45 The excitation of SPW on metal grating with a thin dielectric film.

Modulation profile	Sinusoidal
Modulation period	Λ=455 nm
Modulation amplitude	a_1=12.5 nm
Substrate dielectric	Refractive index n_s=1.5
Metal layer	Gold, thickness h=100 nm
Dielectric thin film	Refractive index n_f=1.5, thickness ρ=0..10 nm
Superstrate dielectric	Water, refractive index n_d=1.333

Tab. 4 Parameters of diffraction grating structure.

3.3.1 SPR sensitivity to refractive index changes - analytical theory

Refractive index variations occurring within the evanescent field of SPW alter its propagation constant. Therefore, refractive index variations on the surface of a metallic diffraction grating can be observed as a shift in surface plasmon resonance. Shifts in either SPR angle of incidence or SPR wavelength on a metallic diffraction grating can be analytically calculated by differentiating the condition (1.5) into which SPW propagation constant k_{SPW} is substituted. In general, it is a function of wavelength λ, refractive index of superstrate dielectric $n_d = \sqrt{\varepsilon_d}$, thin film refractive index $n_f = \sqrt{\varepsilon_f}$, and the thin film thickness ρ. We shall derive $k_{SPW}(\lambda,\rho,n_d,n_f)$ under following approximations: (i) the modulation of diffraction grating surface is neglected (as shown in Chapter 3.1.4, this approximation does not significantly change SPW dispersion relation for studied grating structure) and (ii) the metal layer is replaced with a semi-infinite metal medium (as follows from Chapter 3.2.4, no difference in SPR reflectivity spectrum is observed semi-infinite gold and gold with the thickness 100 nm). Using these two assumptions, Maxwell equations with standard boundary conditions yield SPW dispersion relation:

$$\left(\frac{\kappa_m}{\varepsilon_m}+\frac{\kappa_d}{\varepsilon_d}\right)+\varepsilon_f\rho\left(\frac{\kappa_f^2}{\varepsilon_f^2}+\frac{\kappa_m\kappa_d}{\varepsilon_m\varepsilon_d}\right)+\mathrm{O}\left(\kappa_f^2\rho^2\right)=0, \tag{3.3}$$

where $\kappa_j=\sqrt{k_{SPW}^2-k_0^2\cdot\varepsilon_j}$, $j=d,m,f$ is transverse propagation constant in j^{th} medium (subscript f denotes thin dielectric film, m semi-infinite metal and d semi-infinite dielectric). The dispersion relation (3.3) is valid for a thin dielectric layer $\kappa_f^2\rho^2<<1$. A change in the propagation constant δk_{SPW} induced by variations in the refractive index in whole dielectric δn_d and thin film δn_f can be obtained by differentiating the dispersion relation (3.3). After substituting terms $\delta k_{SPW}/\delta n_f$ and $\delta k_{SPW}/\delta n_d$ into the phase-matching condition (1.5) differentiated by $\delta\lambda$, $\delta\theta$, δn_d, δn_f, sensitivity of SPR wavelength and SPR angle of incidence to changes in the refractive index in whole dielectric δn_d and thin film δn_f can be obtained as:

$$S_b^W=\frac{\delta\lambda_{res}}{\delta n_d}=\mathrm{Re}\left\{\frac{\sqrt{\varepsilon_d}\,\varepsilon_m^2}{\frac{\varepsilon_m\varepsilon_d\left(\varepsilon_d+\varepsilon_m\right)}{\lambda}-\frac{\varepsilon_d^2}{2}\frac{\partial\varepsilon_m}{\partial\lambda}}\right\}, \tag{3.4}$$

$$S_b^A=\frac{\delta\theta_{res}}{\delta n_d}=\mathrm{Re}\left[\frac{\varepsilon_m}{\varepsilon_d+\varepsilon_m}\right]^{3/2}, \tag{3.5}$$

$$\Sigma=\mathrm{Re}\left\{\frac{2k_0^2}{k_{SPW}^4}\frac{2k_{SPW}^2-k_0^2\varepsilon_d}{\frac{1}{\kappa_m\varepsilon_m}+\frac{1}{\kappa_d\varepsilon_d}}\right\}, \tag{3.6}$$

$$S_s^W=\frac{\delta\lambda}{\delta n_f\rho}=S_d^W\Sigma, \tag{3.7}$$

$$S_s^A=\frac{\delta\theta}{\delta n_f\rho}=S_d^A\Sigma, \tag{3.8}$$

where S_b^W denotes the wavelength bulk refractive index sensitivity, S_b^A for angular bulk refractive index sensitivity, S_s^W wavelength surface refractive index sensitivity and S_s^A angular surface refractive index sensitivity. In angular and wavelength surface refractive index sensitivity the term Σ (3.6) takes into account the overlap of SPW field with the dielectric thin film. By using the herein derived theory, we calculated the dependence of $S_b^W, S_b^A, S_s^W, S_s^A$ on the wavelength (Fig. 46a and Fig. 46b). In these simulations, for each wavelength the grating period was be obtained from the phase-matching condition (1.5) with θ=0, see Fig. 32.

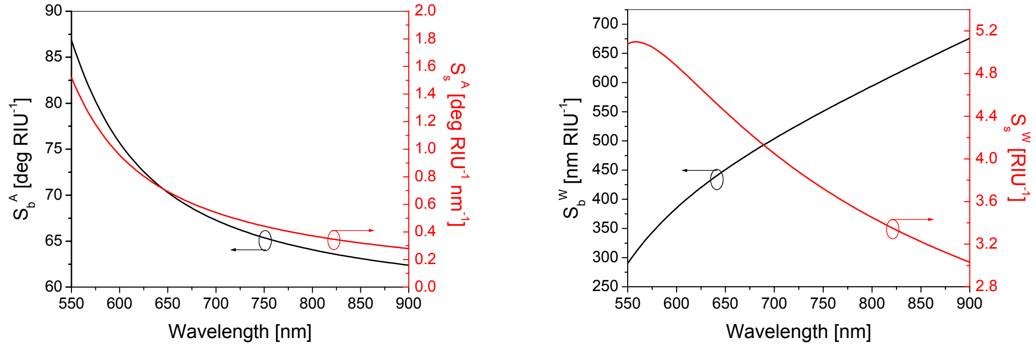

a) b)

Fig. 46 Dependence of bulk and surface refractive index sensitivity on the wavelength for: a) SPR wavelength and fixed angle of incidence *θ*=0 and b) SPR angle of incidence in the range *θ*=2-5 deg and fixed wavelength.

3.3.2 SPR sensitivity to refractive index changes - numerical theory

The analytical theory for SPR sensitivity was compared with numerical simulations relying on integral method (see Chapter 1.3.2). For grating structure identical with the one in previous Chapter 3.3.1, the bulk and surface refractive index sensitivity were determined from a shift of SPR dip in the reflectivity spectrum. In this study, angular and wavelength reflectivity spectra were calculated for the refractive index of the whole dielectric in the range from n_d=1.33-1.35 and for a thin film with refractive index 1.5 and the thickness ρ=0 -10 nm. Obtained results in Fig. 47 and Fig. 48 show that increasing dielectric refractive index n_d and the thickness of the thin layer ρ shofts the SPR dip towards longer wavelength (in wavelength SPR spectrum) and higher angle of incidence (in angular SPR spectra).

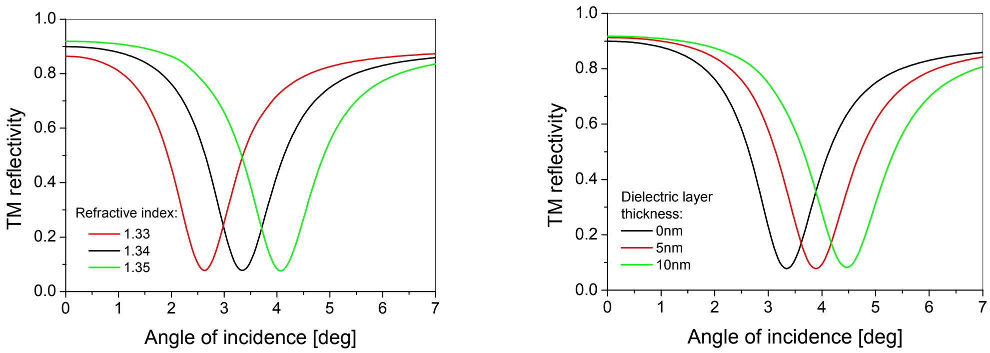

a) b)

Fig. 47 SPR angular reflectivity spectra for a) bulk dielectric refractive index n_d=1.33, 1.34 and 1.35 and b) bulk dielectric refractive index of n_d=1.33 and a layer with refractive index n_f=1.5 and thickness ρ=0, 5 and 10 nm; gold diffraction grating with sinusoidal modulation, amplitude a_1=12.5 nm, period Λ=455 nm, wavelength 633 nm.

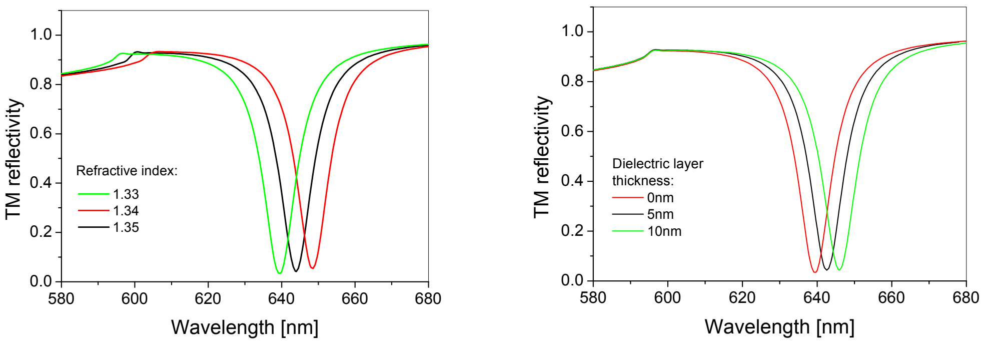

a) b)

Fig. 48 SPR wavelength reflectivity spectra for a) bulk dielectric refractive index n_d=1.33, 1.34 and 1.35 and b) bulk dielectric refractive index of n_d=1.33 and a layer with refractive index n_f=1.5 and thickness ρ=0, 5 and 10 nm; gold diffraction grating with sinusoidal modulation amplitude a_1=12.5 nm, period Λ=455 nm, angle of incidence θ=0.

From these spectra the angular and wavelength surface and bulk refractive index sensitivities S_b^A, S_s^A, S_b^W, S_s^W were calculated as the ratio of SPR dip shift and corresponding refractive index change, see definitions (3.4)-(3.8). Such obtained sensitivities were compared with the ones obtained from analytical Equations (3.4)-(3.8), see Tab. 5. The difference between numerical and analytical theory was found to be 2 per cent for the bulk refractive index sensitivity and 15 per cent for surface refractive index sensitivity. This discrepancy is probably caused by approximations used in derivation of analytical formulas (3.4)-(3.8).

	Angular reflectivity spectrum (λ=633 nm)	Wavelength reflectivity spectrum (λ=640 nm)
Bulk RI sensitivity (numerical)	S_b^A=72 deg RIU^{-1}	S_b^W=445 nm RIU^{-1}
Bulk RI sensitivity (analytical)	S_b^A =71 deg RIU^{-1}	S_b^W =439 nm RIU^{-1}
Surface RI sensitivity (numerical)	S_s^A =0.67 deg nm^{-1} RIU^{-1}	S_s^W =3.9 RIU^{-1}
Surface RI sensitivity (analytical)	S_s^A =0.76 deg nm^{-1} RIU^{-1}	S_s^W =4.5 RIU^{-1}

Tab. 5 Comparison of SPR sensitivity obtained from analytical theory and numerical simulations on sinusoidal diffraction grating.

3.3.3 Sensitivity to refractive index changes - on the grating modulation profile

In general, characteristics of SPW can be altered by changing the grating modulation profile (see Chapter 3.2.3) which affects its sensitivity to refractive index changes. In this section, let us explore the affect of the component with the amplitude a_2 in the grating profile to SPR sensitivity.

As was shown previously, depending on the mutual phase φ_2-φ_1 between the modulation components with the amplitudes a_1 and a_2, two SPW modes at different wavelengths can be excited. The wavelength refractive index sensitivity of these modes was numerically investigated for the diffraction grating geometry described in Chapter 3.3.1 (see Fig. 45 and Tab. 4). SPR reflectivity spectra corresponding to the excitation of these modes were calculated for the refractive index of the bulk dielectric n_d=1.33-1.35 and for a thin film with the refractive index 1.5 and the thickness ρ=0-10 nm (see Fig. 49)

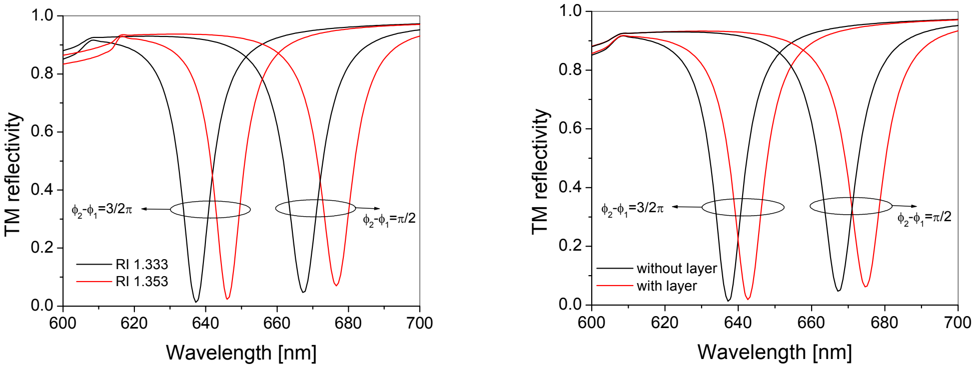

a) b)

Fig. 49 Wavelength reflectivity spectra for a) bulk dielectric refractive index n_d=1.333 and 1.353 and b) bulk dielectric refractive index n_d=1.333 and refractive index of thin film n_f=1.5 and thickness 10 nm; gold diffraction grating with Λ=455 nm, a_1=12.5 nm, a_2=5 nm, φ_2-φ_1=3/2π and φ_2-φ_1=π/2, angle of incidence θ=0.

Refractive index sensitivities S_b^W and S_s^W were calculated using the same procedure as in the previous Chapter 3.3.2. Further, we compared SPR refractive index sensitivity on sinusoidal diffraction grating (a_2=0 nm) with the one for gratings with a_2=5 nm and φ_2-φ_1=3/2π and π/2. Obtained results presented in Tab. 6 reveal that wavelength bulk refractive index sensitivity S_b^W for both longer and shorter wavelength resonances (φ_2-φ_1=1/2π and 3/2π, respectively) varied less than 5 per cent from the one on sinusoidal grating. However, the surface refractive index sensitivity was 25 per cent increased S_s^W for the longer wavelength resonance and 15 per cent decreased for the shorter wavelength resonance when comparing with SPR on sinusoidal grating. The reason for these variations is due to a higher localization of magnetic intensity distribution of longer wavelength surface plasmon mode when comparing shorter wavelength one, see Chapter 3.2.3 and Fig. 39.

Diffraction grating parameters	Surface refractive index sensitivity (numerical)	Bulk refractive index sensitivity (numerical)
a_1=12.5 nm, a_2=0 nm	S_s^W =3.9 RIU^{-1}	S_b^W =445 nm RIU^{-1}
a_1=12.5 nm, a_2=5 nm, φ_2-φ_1=1/2π	S_s^W =4.9 RIU^{-1}	S_b^W =465 nm RIU^{-1}
a_1=12.5 nm, a_2=5 nm, φ_2-φ_1=3/2π	S_s^W =3.3 RIU^{-1}	S_b^W =453 nm RIU^{-1}

Tab. 6 Comparison of SPR sensitivity on diffraction grating with sinusoidal modulation and mirror- symmetric modulation with two harmonic components a_1=10 nm and a_2=5 nm.

3.4 Analysis of diffraction grating-based SPR biosensor

In this chapter, analysis of diffraction grating-based SPR biosensor is carried out. As was introduced in Chapter 2, we further focus on the configuration in which refractive index variations at the surface of a metallic grating are measured using *spectroscopy of surface plasmons* and *angular modulation of SPR*.

For design of diffraction grating-based SPR biosensor, let us assume the geometry in which an angular reflectivity spectrum from a diffraction grating is projected at position sensitive detector. As illustrated in Fig. 50, for normal incidence geometry this can be performed by an optical system with a beam splitter and a cylindrical lens. A parallel large diameter monochromatic light beam is focused by the cylindrical lens at the grating surface where it is partially coupled to a SPW and partially reflected. The excitation of a SPW manifests as a decrease in the angular distribution of reflected light intensity in a narrow range of angles. The reflected beam propagates back through the cylindrical lens, it is separated from the incident wave in a beam splitter and its intensity distribution is projected at a position sensitive detector. Variations in resonant angle of incidence due to refractive index changes at the diffraction grating surface are observed from changes in the intensity distribution measured with position sensitive detector.

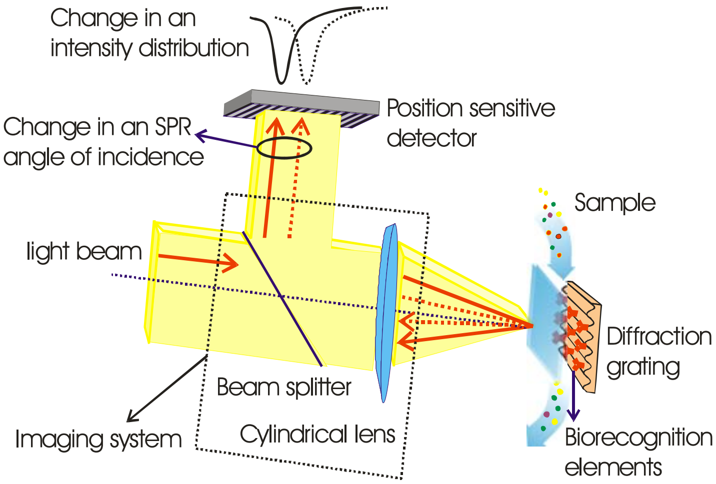

Fig. 50 SPR biosensor with diffraction grating and angular modulation of SPR in normal incidence geometry.

The analysis of diffraction grating-based SPR biosensor includes (i) investigation of SPR sensitivity to binding of biomolecules on a metallic diffraction grating and (ii) determining of optimum grating modulation profile and optimum operating wavelength yielding maximum accuracy in the measurement of refractive index changes induced by binding of biomolecules at the sensor surface.

3.4.1 Sensitivity of SPR angle of incidence to binding of biomolecules

In SPR biosensors, binding of an analyte to biorecognition elements is measured from changes in (average) refractive index n_f at the of the sensor surface. Typically, these refractive index variations occur within certain (sensitive) layer in which the biorecognition elements are immobilized. As was discussed in Chapter 1.2.4, biorecognition elements can form a monolayer or a three-dimensional matrix (see Fig. 20a and Fig. 20b). The refractive index of the sensitive layer n_f increases linearly with the concentration of analyte δc, (3.9). By combining this expression and the Equation (3.8), a change in the SPR angle of incidence $\delta\theta_{res}$ induced by the biomolecule surface coverage Γ can be written as (3.10).

$$\delta n_f = \frac{\partial n_f}{\partial c} \cdot \delta c \tag{3.9}$$

$$\delta\theta_{res} = S_s^A \frac{\partial n_f}{\partial c} \Gamma , \tag{3.10}$$

where S_s^A is the surface refractive index sensitivity derived in Chapter 3.3. The Equation (3.10) holds for the sensitive layer of which thickness is much smaller the transverse propagation constant of SPW (see Chapter 1.1.1). For most protein analytes, the slope coefficient $\partial n_f / \partial c$ lies in the range 0.14-0.2 µl mg^{-1}, [165]. For example, the surface coverage of the SPR sensor corresponding to the shift in SPR angle of incidence $\delta\theta_{res}$ =1 deg lies in the range Γ=7.5-10.5 ng mm^{-2} (for the wavelength of 633 nm).

3.4.2 Determination of SPR changes from angular reflectivity spectrum

The analysis of changes in an SPR spectrum acquired from the position sensitive detector can be performed using numerous methods. These include optimal linear [166], centriod method [167], polynomial regression [167] and Lorentzian function regression [168]. Further, let us assume the polynomial regression method applied to an angular SPR reflectivity spectrum with an SPR dip located at certain angle of incidence θ_{res}. As illustrated in Fig. 51, in polynomial regression method the SPR angle of incidence θ_{res} is calculated as a minimum of a polynomial function fitted to the SPR spectrum.

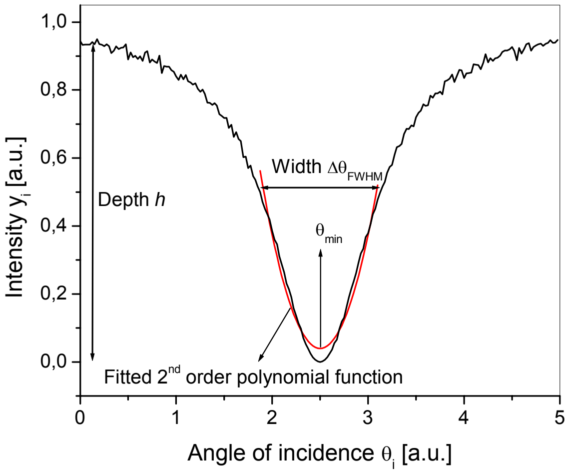

Fig. 51 An SPR dip fitted with a polynomial function.

In general, the accuracy with which the SPR angle of incidence θ_{res} can be determined depends on the noise of SPR spectrum and on the contrast of SPR dip. Typically, the SPR spectrum from a position sensitive detector can be described with a discrete Lorentzian function (3.11) defined at equidistant angles of incidence θ_i corresponding to pixels of position-sensitive detector.

$$f\left(\theta_i\right)=1-h\frac{\Delta\theta_{res}^2/4}{\left(\theta_i-\theta_{res}\right)^2+\Delta\theta_{res}^2/4}, \tag{3.11}$$

where h is the depth of the SPR dip and $\Delta\theta_{res}$ is the SPR dip's full width at half minimum (FWHM). Let us suppose the SPR spectrum exhibits the shot noise which is typically dominant for mostly used photodiode-based detectors such as charge coupled device – CCD, [166]. Assuming the noise between neighboring pixels is non-correlated and exhibits identical statistics for all pixels, the intensity y_i acquired at each detector pixel can be described as:

$$y_i = f(\theta_i)+\eta\cdot\sigma_{y=1}\sqrt{f(\theta_i)}, \tag{3.12}$$

where η is normal distribution $\langle\eta\rangle=0$, $\langle\eta^2\rangle=1$, $\sigma_{y=1}$ is the standard deviation of the intensity acquired by an individual detector pixel at the maximum of SPR spectrum (y=1). To determine standard deviation of the minimum of fitted polynomial function, a set of SPR spectra (indexed with j) with superimposed noise were numerically generated in Maple 7 (from Waterloo Maple Inc., Canada). These spectra were fitted using the least square method with second order polynomial function in the region below SPR dip FWHM. From acquired polynomial functions, minima positions $\theta_{\min}^j$ were analytically calculated. Standard deviation of obtained set of minima positions was found to be dependent on the parameters of SPR dip as:

$$\sigma_\theta=\left\langle\left(\theta_{res}^j-\theta_{res}\right)^2\right\rangle=0.46\sqrt{\Delta\theta_{res}\zeta}\left(\frac{7}{4h}-\frac{3}{4}\right)\sigma_{y=1}, \tag{3.13}$$

where ζ is the angular distance between neighboring pixels. In the region $\Delta\theta_{res}\zeta^{-1}$=50-300 pixels, $\sigma_{y=1}=10^{-3}-5\times10^{-2}$ and h=0.3-1, the difference between numeric model and the approximation formula (3.13) was lower than 5 per cent.

3.4.3 Optimum operating wavelength and grating parameters

Based on the results from previous Chapters 3.4.1 and 3.4.2, let us find the operating wavelength and parameters of a diffraction grating for which the diffraction grating-based SPR sensor yields maximum accuracy in determining of refractive index changes induced by binding of biomolecules at the sensor surface.

Dependence of angular SPR spectrum characteristics on wavelength

Two key parameters of SPR dip affecting the accuracy of SPR sensor are the SPR dip depth h and SPR dip width $\Delta\theta_{res}$. Equation (3.13) shows that the standard deviation with which the SPR angle of incidence can be determined decreases when the SPR dip width $\Delta\theta_{res}$ decreases and the SPR dip depth h increases. As shown in Chapter 3.2.2, the diffraction grating modulation parameters can be adjusted to achieve total extinction of reflected optical wave intensity. As illustrated in Fig. 34, the maximum resonance depth (i.e. h=1) can be achieved for sinusoidal grating by tuning its modulation depth. The second key parameter - SPR dip width $\Delta\theta_{res}$ – rapidly changes with the wavelength. A set of SPR angular spectra for wavelengths from 570 nm to 800 nm was calculated for sinusoidal gold grating with modulation depth adjusted for full coupling of light to a SPW and the angle of incidence equal to $2\Delta\theta_{res}$, see Fig. 52a. The plot in Fig. 52b reveals that the SPR dip width $\Delta\theta_{res}$ decreases with the wavelength in the range 600-750 nm.

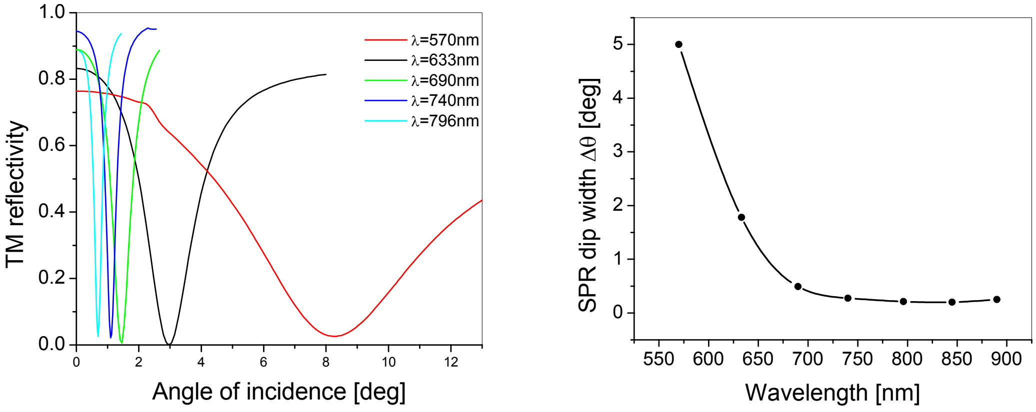

a) b)

Fig. 52 a) Angular SPR reflectivity spectra for different wavelengths - gold sinusoidal diffraction grating with water on its surface, grating period and modulation depth adjusted so full coupling to SPW occurred at the angle of incidence $2\Delta\theta_{res}$, b) The dependence of an SPR dip width $\Delta\theta_{res}$ on the wavelength.

Angular range of SPR biosensor

The angular span of SPR reflectivity spectrum projected on a position sensitive detector needs to be adjusted to cover sufficient part of the SPR dip and its shifts induced by binding of biomolecules on the sensor surface. To cover the spectrum with a Lorentzian SPR dip, let us use the range of $3\Delta\theta_{res}$. In addition, the angular range need to be extended to cover shifts in the SPR dip due to an analyte binding leading to the surface coverage Γ=0-Γ_{max}. From Equation (3.10) follows that the total angular range can be described as:

$$\Delta\theta_{range} = 3\Delta\theta_{res} + S_s^A \frac{\partial n}{\partial c}\Gamma_{\max} . \tag{3.14}$$

Both width of the SPR dip $\Delta\theta_{res}$ and surface refractive index sensitivity S_s^A are functions of the wavelength. By using the surface refractive index sensitivity derived in Chapter 3.3 (see Fig. 46) and SPR dip width $\Delta\theta_{res}$ presented in Fig. 52, the wavelength dependence of the angular span $\Delta\theta_{range}$ was calculated. The wavelength dependence of $\Delta\theta_{range}$ shown in Fig. 53 was obtained for the maximum protein coverage of the sensor surface Γ_{max}=1.1μg mm^{-2} which corresponds to a growth of a protein layer with the thickness up to 10 nm and refractive index 1.45 RIU.

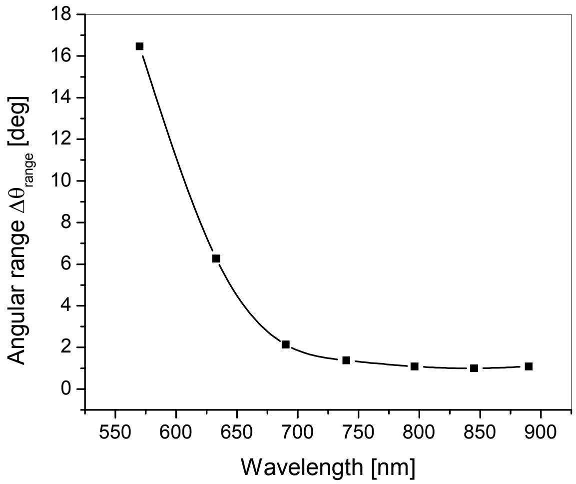

Fig. 53 Wavelength dependence of the angular range of an SPR biosensor corresponding to the maximum surface coverage Γ_{max}=1.1 μg mm^{-2}.

Optimum operating wavelength of SPR biosensor

As follows from Equation (3.10), the surface coverage of an analyte can be obtained from a shift in the SPR angle of incidence as $\delta\Gamma=\delta\theta_{res}(S_S^A\,\partial n/\partial c)^{-1}$. Based on this expression, let us define the function $\chi=S_S^A/\sigma_\theta$ in which S_S^A is the angular surface refractive index sensitivity and σ_θ is the standard deviation of SPR angle of incidence. Using the function χ, the optimum parameters of the biosensor (for which highest accuracy in measurement of $\delta\Gamma$ is achieved) can be determined as the ones for which χ function reaches its maximum. As derived in Chapter 3.4.2, for polynomial regression method the standard deviation of resonant angle of incidence σ_θ is proportional to the term $\Delta\theta_{res}^{1/2}\zeta^{1/2}$. In this term $\Delta\theta_{res}$ denotes the SPR dip width and ζ the angular distance between two neighboring pixels of detector. If we assume a detector with certain number of pixels on which the angular range $\Delta\theta_{range}$ is matched, the angular distance ζ can be assumed to be proportional to the angular range $\Delta\theta_{range}$ and thus χ function can be rewritten as follows.

$$\chi=\frac{S_S^A}{\sigma_\theta}\sim\frac{S_S^A}{\sqrt{\Delta\theta_{res}\zeta}}\sim\frac{S_S^A}{\sqrt{\Delta\theta_{res}\Delta\theta_{range}}}. \tag{3.15}$$

With the use of previous results, the wavelength dependence of χ function was calculated in the range 630 – 900 nm. As shown in Fig. 54, the function χ has its maximum at 800 nm. These simulations indicate that an SPR biosensor with gold diffraction grating, angular modulation of SPR and small SPR angles of incidence achieves its maximum accuracy at this wavelength.

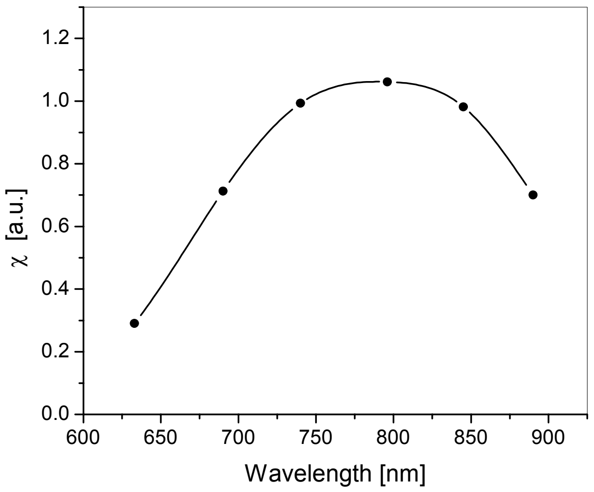

Fig. 54 The dependence of χ function on the operating wavelength for diffraction grating SPR biosensor relying on angular modulation of SPR and near normal incidence geometry.

4 Experimental

Experimental part of this work includes fabrication of diffraction gratings, their replication and characterization. Based on this work, optimized diffraction grating structure was developed and implemented in a SPR sensor chip cartridge with interfaced a fluidic system. To measure SPR changes occurring on the sensor chip, sensor chip reader and data processing were designed. The overall sensor device was tested and its main performance characteristics were determined. The potential of developed SPR sensor platform is demonstrated in model bioexperiment for study of biomolecular interactions at the sensor surface.

4.1 Preparation of diffraction gratings

The preparation of relief diffraction grating structures consisted of two steps described in this section: fabrication of *holographic grating master* and its *replication*. Diffraction gratings made according to presented protocols were characterized optically and by the Atomic Force Microscope (AFM).

4.1.1 Holographic diffraction gratings

Gratings masters were holographically prepared in a photoresist layer. In this technique, the photoresist layer is exposed to an interfering coherent optical field followed with etching to produce a periodic modulated surface of a grating, see Fig. 55. Positive photoresist polymers AZ1350 or SF1813 (from Shipley Inc., USA) which are sensitive at wavelengths 350-450 nm) were used. The polymer was deposited on a polished substrate made of BK7 glass (dimensions of 32 x 15 x 1.5 mm from Schott Glass Technologies, Duryea, USA) by means of spin-coating using the protocol in Tab. 7. The thickness of photoresist layer (1 μm) and refractive index (1.7 at the wavelength 633 nm) was measured by ellipsometer (SE850 Santech, Germany). The deposition of the photoresist layer was made in a laminar flow-box with HEPA filters to avoid contamination of its surface with dust particles. Exposure of photoresist to light at the wavelengths 350-450 nm was avoided using filters.

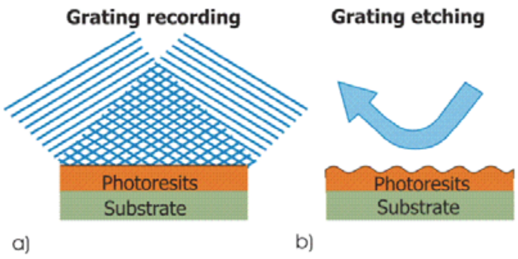

Fig. 55 Preparation of diffraction grating: a) holographic recording, b) etching.

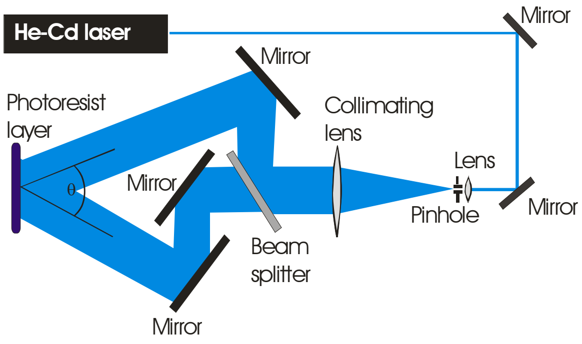

Fig. 56 Optical arrangement for holographic recording of diffraction gratings based on Mach-Zehnder interferometer.

1)	The rear surface of a glass slide was painted with light absorbing black paint to reduce back reflections during the holographic recording of the grating.
2)	The top surface of the glass substrate was carefully cleaned with acetone, ozone cleaned (UVO Cleaner 42-220 from Jelight Company, Inc.) for 20 min, subsequently washed in purified water and ethanol, and dried in nitrogen stream.
3)	The photoresist solution was spun at the rotation speed 3500 rpm, rotation time 15 s.
4)	After the rotation, the deposited photoresist layer was dried for 30 min at the temperature 90 ˚C.

Tab. 7 Protocol for preparation of photoresist layer on a planar glass substrate.

The photoresist layer on the glass substrate was exposed to an interfering field formed by two coherent plane waves intersecting under certain angle θ. The grating recording was performed using the optical setup based on Mach-Zehnder interferometer arrangement depicted in Fig. 56. In this optical setup, laser beam from stabilized He-Cd laser (model 4240PS from Liconix, USA, emitting a polarized light at the wavelength λ=442 nm, the output optical power 60mW, coherence length 25 cm) was focused at a pinhole (from Spectra Physics) by means of a microscope objective (from Spectra Physics) producing zero diffraction order diverging spherical wave. This wave was collimated with an objective lens and launched into a Mach-Zehnder interferometer. In the interferometer, the collimated beam was made passed through a beam-splitter, after which the two waves with equal intensity were directed toward the glass substrate by means of metallic mirrors (dimensions 100 x 70 mm, planarity λ/4, custom made in VOD, Turnov, Czech Republic). The glass substrate with photoresist layer was mounted perpendicularly to the interference fringes and thus recorded gratings possessed mirror symmetry. In each interferometer arm the optical wave carried the intensity 30 μW/cm^2 (measured with a silicon detector 1830-C from Newport). Before each holographic recording, the whole setup was let mechanically stabilize for 2 min. The holographic recording was applied with the exposure time in the range of 20-500 seconds. The spacing of interference fringes Λ recorded into the photoresist layer was adjusted by tuning the intersection angle θ according to following equation.

$$\Lambda = \frac{\lambda}{2\sin(\theta/2)}, \tag{5.1}$$

In the following step, the photoresist layer was soaked with a gently stirred developer (AZ303 from Shipley, USA, diluted with distilled water at the ratio 1:9) to etch the grating surface. The development was applied successively. After each development cycle the grating was removed from the developer, rinsed in distilled water, dried with a nitrogen stream and optically characterized. The development continued until the desired parameters were achieved. The total development time was typically between 15-500 seconds. In between each development cycle, minus first diffraction order efficiency of etched diffraction grating was measured in minus first diffraction order Littrow configuration. In this configuration, the grating efficiency (we used the ratio of intensity in diffracted wave and normal incidence reflected wave) was measured at the wavelength of 632.8 nm (using the He-Ne laser LGK 7634, from Carl Zeiss, Germany). TM polarized light was used as for this polarization grating efficiency is higher than for TE polarization. An example of the dependence of the efficiency on the grating modulation depth for photoresist and gold-coated gratings calculated for sinusoidal modulation with the period Λ=455 nm is given in Fig. 57.

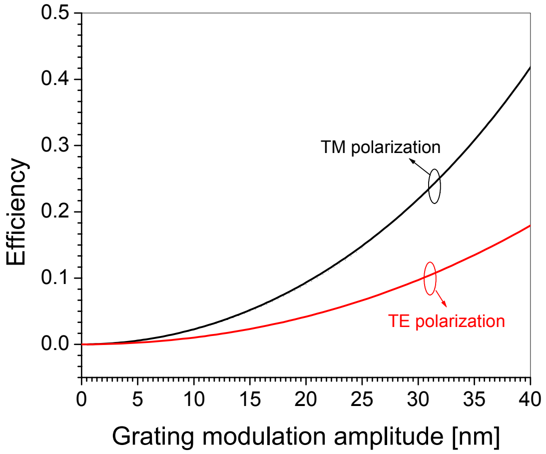

Fig. 57 Dependence of minus first diffraction order efficiency on the modulation amplitude for TM and TE polarization; minus first diffraction order Littrow geometry and sinusoidal photoresist grating with the period Λ=455 nm, wavelength λ=632.8 nm.

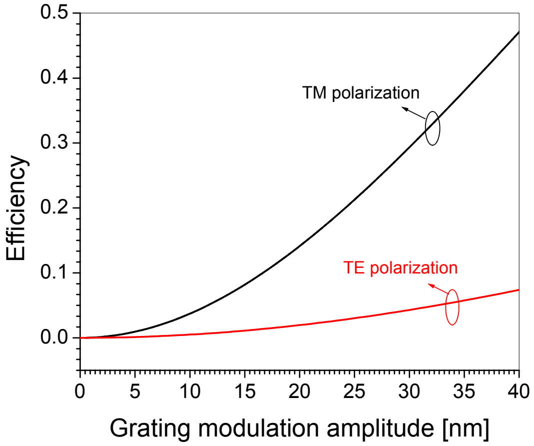

Fig. 58 Dependence of minus first diffraction order efficiency on the modulation amplitude for TM and TE polarization; minus first order Littrow geometry and sinusoidal gold grating with the period Λ=455 nm, wavelength λ=632.8 nm.

4.1.2 Diffraction gratings replication

To produce durable diffraction gratings, we used the holographic gratings as masters and replicated them. We adopted the soft lithography technique originally proposed by Whitesides in early nineties of the last century [169] as this approach offers the advantage of relatively simple technique capable of copying of surface details with dimensions smaller than 30 nm.

The procedure of replication is illustrated in Fig. 59. It consists of two steps in which master diffraction grating is cast into an elastomer stamp which is after used for transfer the grating modulation into a UV curable polymer.

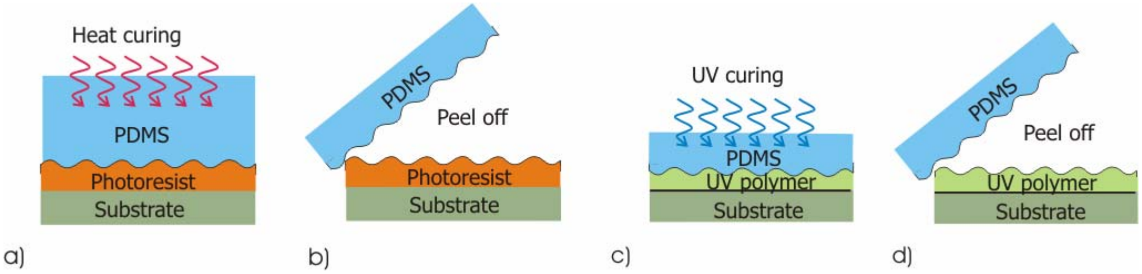

Fig. 59 Replication of master grating: a) elastomer stamp casting and curing, b) elastomer release from the master grating, c) elastomer copy into a UV curable polymer, d) elastomer stamp release from the replica grating.

The elastomer stamp was made using the protocol presented in Tab. 8. The master grating was mounted into a special mould and a thin self adhesive Mylar sheet (thickness 100 μm) was attached over its edges. Then, the mould was filled with liquid poly-dimethylsiloxane (PDMS, obtained as Sylgard 184 from Dow Cornig Inc., USA) and cured at the temperature 60 °C. After the curing, PDMS elastomer stamp with cast relief modulation was released from the master grating. The thin self-adhesive Mylar sheet along the master grating edges produced a depression of the stamp surface at the grating circumference which allowed suppressing the imperfection during further replication.

1)	Sylgard 184 (Dow Corning) liquid was mixed with supplied curing agent at ratio 1:10.
2)	Master grating was placed into a special mould in which mixture of Sylgard 184 and its curing agent was poured. The volume of used liquid was adjusted to produce the elastomer stamp with the thickness of about 5 mm.
3)	Sylgard polymer inside the mould was degassed using a vacuum pump (pressure 200 mbar) and cured at the temperature of 60 °C for 6 hours.
4)	The elastomer stamp was released from the master grating.

Tab. 8 Protocol for preparation of elastomer stamp with cast surface modulation of master grating.

1)	Glass substrate was cleaned in Piranha solution for 10 minutes, washed in de-ionized water and dried in nitrogen stream. After, the surface of the glass substrate was cleaned in ozone cleaner for 20 minutes (UVO Cleaner 42-220 from Jelight Company, Inc.) and again washed in de-ionized water and ethanol and dried in nitrogen stream.
2)	UV curable polymer was spincoated in a glass slide, rotation speed 9000 rpm for OGG 146 and 7000 rmp for NOA-72, time 15 s.
3)	UV curable polymer was brought in contact with elastomer stamp and let mechanically and temperature stabilize for 30 min.
4)	UV curable polymer was illuminated with UV light (from mercury discharge lamp, power 5.5 W) for 30 min.
5)	Elastomer stamp was released from the replica grating.
6)	OGG 146 replica was heated to 150 ºC for 30 min.

Tab. 9 Protocol for preparation of replica gratings in a UV curable polymer layer using PDMS elastomer stamp.

Two UV curable polymers we tested for replication of diffraction gratings: NOA-72 (from Norland Inc., USA) and OG-146 (from Epotek Inc., USA). NOA-72 and OGG-146 polymer have viscosity 40 cPs and 175 cPs, respectively. The viscosity of NOA-72 polymer was decreased by diluting with tetrahydrofuran (from Sigma-Aldrich) at the ratio 1:10. Prior the replication, the polymer was deposited on a glass substrate using spincoating (see Tab. 9). These glass substrates had dimensions of 32 x 15 mm and they were cut from microscope glass slides cleaned as described in Tab. 9. Onto the thin polymer layer, PDMS elastomer stamp was placed using the setup depicted in Fig. 60a. In this setup, the polymer-coated glass slide and the elastomer stamp were brought slowly in contact using XYZ translation stages. The glass slide and the stamp were mounted slightly unparallel (approximately 5 deg) to avoid trapping of air bubbles in between PDMS stamp and replica. Then, the polymer layer was cured by illuminating with UV light (from mercury discharge lamp, power 5.5 W) through the elastomer stamp. After, PDMS elastomer stamp was released and polymer replica was removed. Finally, the replica gratings made from OGG-146 polymer were heated to 150 ºC for 30 min to undergo glass transition. We found that it was possible to use PDMS stamps repeatedly for more than ten replication cycles.

To illustrate the presented replication procedure, holographic grating master placed in a mould made from acrylic, elastomer stamp and finished replica grating are shown in Fig. 60b. Blue prints of mould and self adhesion Mylar sheet placed over the master grating edges are shown in the Appendix.

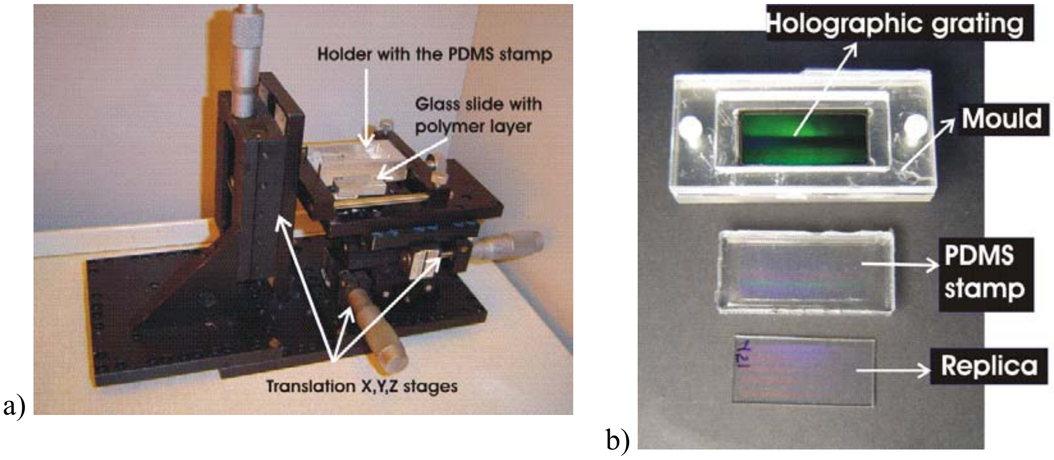

Fig. 60 a) Setup for replication of master diffraction gratings; b) image of a grating master placed in mould for casting of PDMS stamp, cast PDMS elastomer stamp and finished replica grating.

4.1.3 Coating of diffraction gratings with SPR active metal layer

In order to excite surface plasma wave on prepared gratings, their surface was coated with gold layer. To promote adhesion of gold to the grating, titanium layer with the thickness of 3 nm was used. Titanium and gold layers were prepared by thermal evaporation in PFEIFFER PLS 570 apparatus in vacuum better than 10^{-6} mbar. The thickness of gold layer was measured during the evaporation using a quartz crystal oscillator. The optical properties of the gold layer are shown in the Appendix as they were measured with ellipsometer (SE850 Santech, Germany). The evaporation was performed at the temperature of 150 ºC for OGG-146 polymer gratings and at a room temperature for the photoresists and NOA-72 polymer gratings. The gold layer was deposited with the thickness of 100 nm which was evaluated as optically thick in the theoretical part of this work, Chapter 3.2.4. Prior to the evaporation, replica gratings were cleaned in ozone cleaner for 5 minutes (UVO Cleaner 42-220 from Jelight Company, Inc.) followed with washing in de-ionized water and ethanol and drying in a nitrogen stream.

4.1.4 Characterization of holographic diffraction gratings

In this section, we investigate the dependence of depth, modulation profile and roughness of holographically prepared diffraction gratings on the exposition and development time. This study was carried out for two photoresists SF1813 and AZ1350.

Two sets of diffraction gratings were used for each photoresist. The first set of diffraction gratings was recorded for different exposition times in the range 20 - 500 s. For each exposition time, the development time was adjusted so that gratings with constant efficiency (6 per cent) were produced. In Fig. 61, the dependence of development time on the exposition time is presented for both photoresist SF1813 and AZ1350. This figure reveals that development time decreases with the exposition time and shows that photoresist SF1813 is more sensitive than AZ1350. In the second set of gratings, the exposition time was kept constant (120 s for SF1813 and 360 s for AZ1350 photoresist) and the development time was varied. Dependence of the grating efficiency on the development time presented in Fig. 62 reveals that the grating efficiency increases with the development time as the grating becomes deeper.

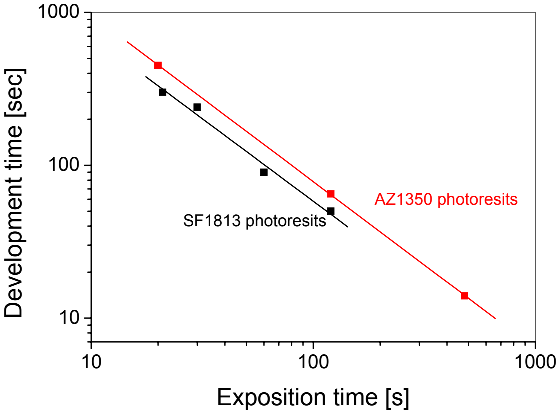

Fig. 61 Dependence of the development time on the exposition time for which grating with efficiency 6 % is prepared, comparison of the photoresist AZ1350 and SF1813, grating period 450 nm.

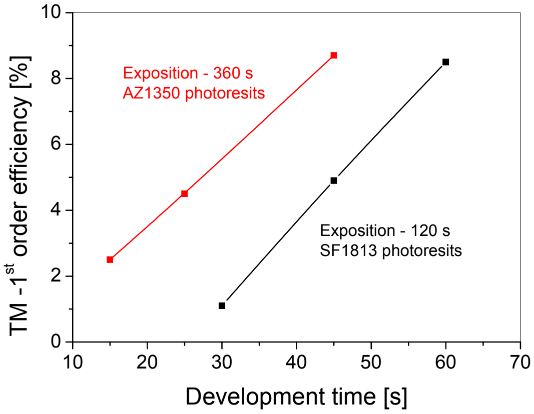

Fig. 62 Dependence of the grating efficiency and grating modulation amplitude on the development time, exposition time 120 seconds for SF1813 and 360 seconds for AZ1350 photoresist, grating period 450 nm.

To measure the profile of modulation and roughness of diffraction gratings, we analyzed their surface with Atomic Force Microscope (Multimode AFM Nan scope IIIa from Digital Instruments, silica stylus OTESPA with radius 5 - 10 nm, tapping mode). The grating modulation profile was determined from an area 2 x 2 μm in which the cross-section of perpendicular to the grating grooves was taken. Multiple lines perpendicular to the grating grooves were averaged to reduce the effect of surface roughness. For both photoresists AZ1350 and SF1813, the grating modulation exhibited sinusoidal profile when the exposition time was lower than 60 seconds. For these gratings, the modulation amplitude determined from their efficiency by comparison with the model (see Fig. 57) matched the one obtained from AFM. The maximum difference between the amplitude measured by AFM and the one determined from the grating efficiency was of 20 per cent. For the exposition time higher than 60 seconds, the grating profile started to differ from the sinusoidal modulation. It exhibited narrower trenches and flatter peaks due to non-linearity of the photoresist. This effect is illustrated in Fig. 63 for AZ1350 photoresists. For low exposition times and high development times, an opposite trend can be observed. As the etching of diffraction grating proceeds in the direction perpendicular to the surface, for high development times the gratings modulation profile tends to exhibit narrower peaks and broader trenches (more detail information can be found in the reference [170]).

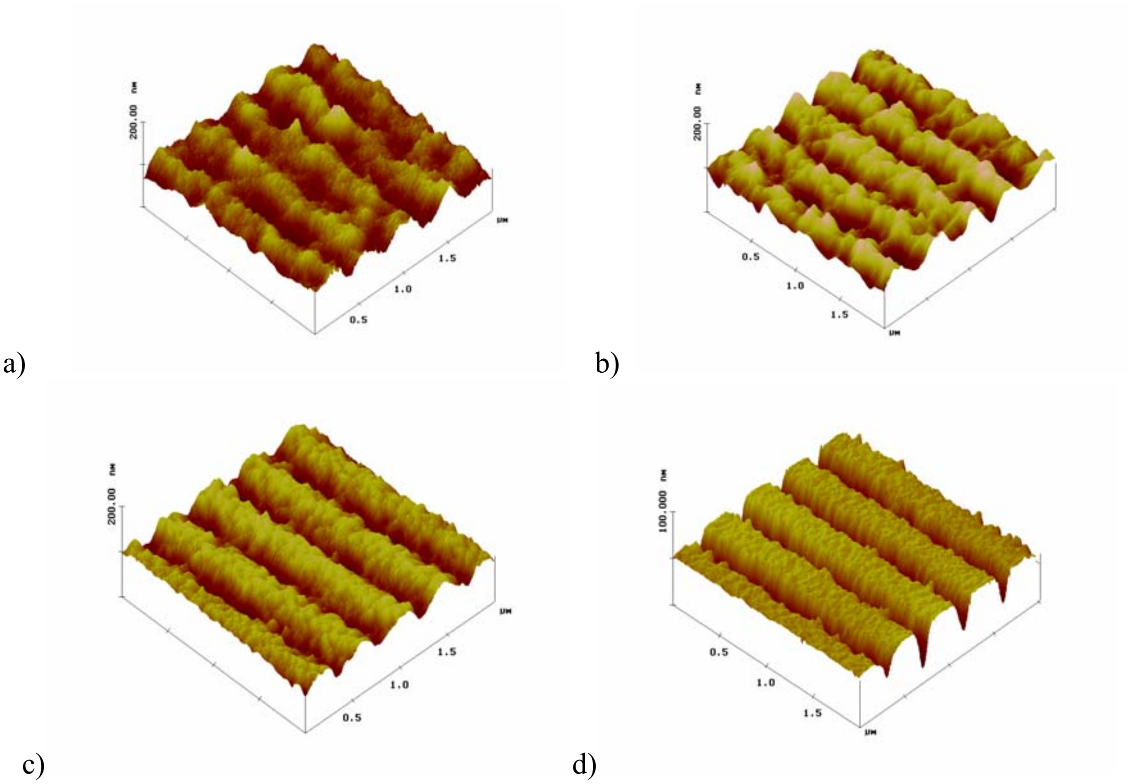

a) b)

c) d)

Fig. 63 Images of surface periodic modulation of gratings made into AZ1350 photoresist with the exposition time a) 20s, b) 30s, c) 100s and d) 500s, measured with AFM.

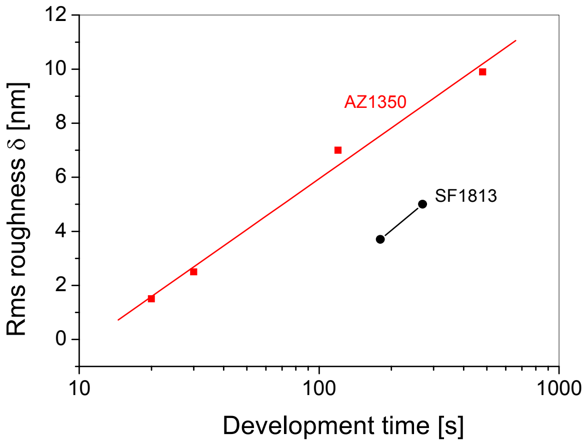

Fig. 64 Dependence of roughness (quantified by root mean square) of the grating on the development time, AZ 1350 photoresist and SF1813 photoresist, diffraction grating efficiency 6 per cent.

From the cross-section of the AFM images parallel to the grating grooves, we measured roughness superimposed over the grating surface. The roughness was quantified by root means square (rms). Results presented in Fig. 64 suggest that the roughness increases when increasing the development time. The reason for this behavior is probably that for higher development time the grating surface is etched deeper and thus imperfections inside the polymer influence the grating surface more significantly. In addition, obtained data reveal that the gratings recorded into SF1813 photoresist exhibited smaller roughness compared to that of AZ1350 gratings.

4.1.5 Characterization of replicated diffraction gratings

In this section, characterization of diffraction gratings prepared by replication is discussed. Reproducibility and fidelity of the replication are tested by analysis of replicas prepared from polymers NOA-72 and OGG-146. The grating parameters including period, grating efficiency, grating modulation profile, and homogeneity across the grating surface are compared with the same parameters of their masters.

In Tab. 10 and Tab. 11, parameters of replica diffraction gratings prepared from a NOA-72 and OGG-146 polymers, respectively, are compared with the ones of their masters. These gratings were prepared from a single PDMS stamp made from a holographic master grating. Obtained results reveal that the homogeneity of the grating efficiency and homogeneity of modulation depth was identical for both master and replica gratings. The grating modulation period of replicas was 1 per cent lower comparing to that of the master due to the temperature expansibility of the PDMS cured at the temperature 60 ºC (see the protocol presented in Tab. 8). Probably due to the mechanical relaxation and volume changes of NOA-72 polymer, the grating modulation depth of the replica gratings was 25% lower than the one of the master grating. This decrease was not observed on OGG-146 polymer replicas. When comparing the overall efficiency of the set of ten replica gratings (made from NOA-72 polymer), it exhibited the standard deviation (SD) of 1.2 per cent. To demonstrate the reproducibility of diffraction grating replication, we coated five gratings made from a single PDMS stamp into NOA-72 polymer with gold layer (100 nm thickness) and measured their SPR reflectivity. This reflectivity was acquired in wavelength spectrum for normal incidence geometry and gratings were brought in contact with water. Obtained results presented in Fig. 65 show spectra with SPR dip centered at the wavelength 656.4±0.2 nm, minimum 0.1±0.02 and full width at half minimum of 16±1 nm.

	Master grating	Replica grating
Grating modulation period	463 nm	460 nm
Grating efficiency (TM polarization)	10 %	5 %
Grating modulation amplitude	20.5 nm	15 nm
Homogeneity of the efficiency across the surface	15% (standard deviation)	15% (standard deviation)
Homogeneity of modulation depth across the surface	5% (standard deviation)	5% (standard deviation)

Tab. 10 Parameters of holographic master grating made into photoresist SF1813 compared to the ones of its replicas made into NOA-72 polymer.

	Master grating	Replica grating
Grating modulation period	449 nm	443 nm
Grating efficiency (TM polarization)	2.3 %	2.3 %
Grating modulation depth	10.5 nm	10.5 nm
Homogeneity of the efficiency across the surface	10% (standard deviation)	10% (standard deviation)
Homogeneity of modulation depth across the surface	5% (standard deviation)	5% (standard deviation)

Tab. 11 Parameters of holographic master grating made into photoresist SF1813 compared to the ones of its replicas made into OGG-146 polymer.

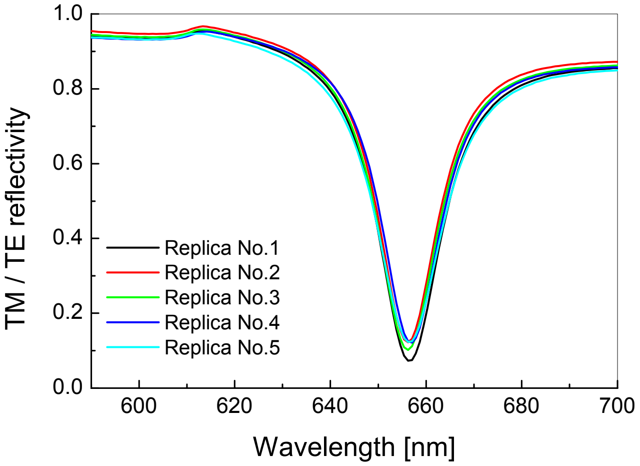

Fig. 65 SPR reflectivity spectra from set of five replica gratings prepared from single elastomer stamp, sinusoidal grating period Λ=460nm, grating modulation amplitude a_1=15 nm, gold layer thickness 100 nm, water in contact with grating surface.

4.1.6 Diffraction gratings preparation – summary

In the previous chapters, we presented procedures for preparation and replication of diffraction gratings. Two photoresists SF1813 and AZ1350 were tested for holographic recording of diffraction grating masters. Performed experiments revealed that the photoresist SF1813 was more sensitive and that SF1813 gratings exhibited lower roughness when comparing with AZ1350 ones. To prepare more durable gratings, we adopted replication of grating masters by soft lithography. We tested UV curable polymers NOA-72 and OGG-146 for the replication. OGG-146 polymer was found to be more suitable for sensor applications as it was found resistant to mostly used solvents (acetone, ethanol, phosphate buffer saline) and it was stable at elevated temperatures (the degradation temperature of OGG-146 polymer was 363 ºC while the one for NOA-72 polymer was below 125 ºC).

4.2 Surface plasmon resonance on diffraction gratings

Surface plasmon resonance on diffraction gratings with different of modulation profiles and modulation depths was experimentally explored. Surface plasmon resonance on prepared diffraction grating structures was observed in angular and wavelength reflectivity spectrum and the sensitivity of SPR to changes in refractive index was determined. Obtained results were compared with the theory.

4.2.1 Optical arrangements

For observation of surface plasmon resonance in angular and wavelength reflectivity spectra two optical setups were used, see Fig. 66 and Fig. 67.

In the optical arrangement used for angular spectrum measurements, light beam from He-Ne laser (SL03 from Sios, Germany, wavelength 623.8 nm, beam divergence 0.09º) was launched through a Glan-Thompson polarizer and a rotary $\lambda/2$ waveplate (from VOD CAS, Turnov) allowing selecting TM or TE polarization. The polarized light was made incident at diffraction grating mounted on a rotation stage (accuracy of adjusting the angle of incidence was 1 minute). The intensity of light reflected from the grating surface was measured with a silicon detector. Intensity measured in TM polarization was normalized with the one measured in TE polarization. On the grating surface a droplet of liquid with desired refractive index was micropipetted and covered with a microscope cover-glass.

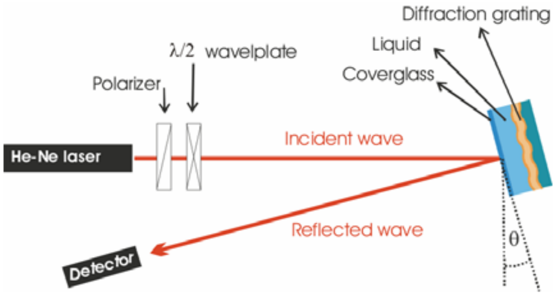

Fig. 66 Optical setup for measurements of angular SPR reflectivity spectrum.

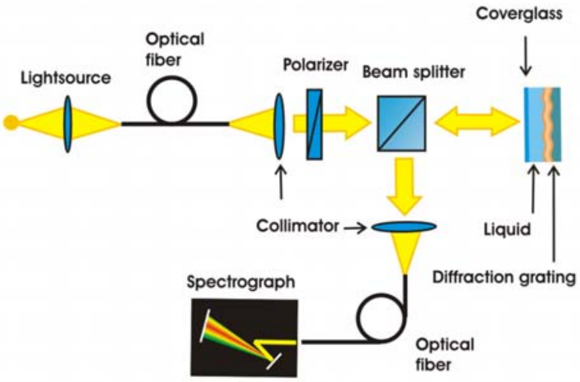

Fig. 67 Optical setup for measurements of wavelength SPR reflectivity spectrum.

The optical setup used for measurements of SPR wavelength reflectivity spectrum is depicted in Fig. 67. White light from a halogen lamp built in a spectrometer (CL 500 from Ziess, Germany) was coupled into an multimode fiber (FT-200-EMT from Thorlabs, USA) and brought to collimator (from Ziess, Germany) producing a collimated light beam with the divergence 0.3º. The collimated beam was polarized with a broad-band polarizer (Polarcor 800-HC, distributed by Corning, Inc., USA) and made normal incident on the diffraction grating. Reflected light from the grating was separated from the incident light using a cube beam splitter (from Linos, UK) and coupled by means of an output collimator (from Zeiss, Germany) into multimode optical fiber (FT-200-EMT from Thorlabs, USA). The output optical fiber was connected to the input of a spectrograph (CLH 500 with wavelength resolution 2.5 nm from Zeiss, Germany), which was used o measure the wavelength spectrum of reflected light. Measured spectrum in TM polarization was normalized with the one measured in TE polarization.

4.2.2 Sinusoidal diffraction gratings with different modulation depth

To explore dependence of SPR on the grating modulation depth, four holographic sinusoidal gratings with the modulation amplitude a_1 in the range 6-24 nm were prepared. These gratings were made using the protocol described in Chapter 4.1.1 (SF1813 photoresist, exposition time 50 seconds, development time adjusted to achieve desired modulation depth) and coated with 100 nm of gold by using the recipe in Chapter 4.1.3. The surface of these gratings was analyzed by Atomic Force Microscope and evaluated as was discussed in Chapter 4.1.4, see Fig. 68.

Modulation amplitudes a_1 of diffraction gratings measured from AFM and the ones obtained from grating efficiency were evaluated. Obtained data in Tab. 12 show that grating amplitudes measured with AFM are approximately 25 per cent lower comparing with those from grating efficiency. This discrepancy can originate from the fact that grating area analyzed by AFM was much smaller than the one on which the grating efficiency was measured.

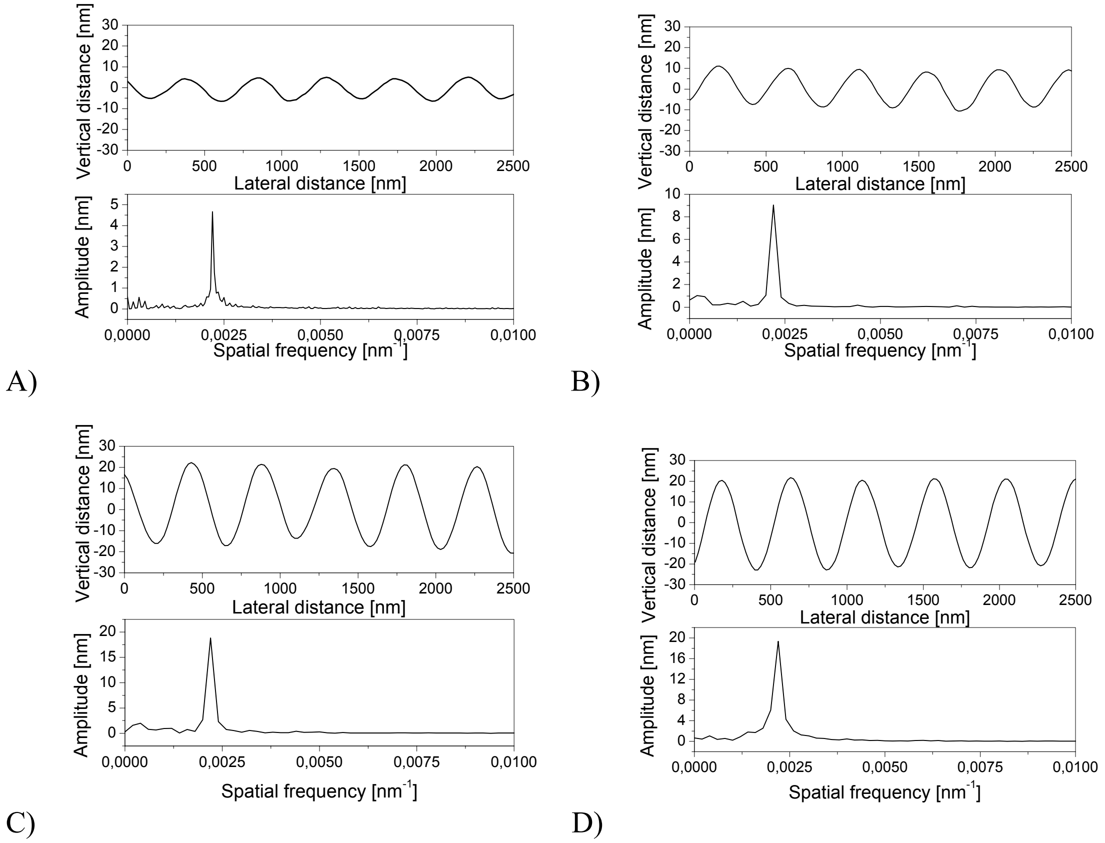

Fig. 68 Surface modulation profile of four sinusoidal gratings with different modulation amplitudes, each graph shows the dependence of grating surface height on the lateral distance perpendicular to the grating grooves (upper part of the graph), and the Fourier spectrum of the grating profile

(bottom part of the graph). Grating modulation profile of gold coated grating was averaged over 700 nm perpendicular to the grating grooves.

Grating sample	Modulation amplitude a_1 (from efficiency)	Modulation amplitude a_1 (from AFM)
A	6 nm	4.8 nm
B	11.5 nm	8.2 nm
C	18 nm	17 nm
D	24 nm	18 nm

Tab. 12 Parameters of the set of gold coated sinusoidal grating samples A-D with different surface modulation depth, grating modulation period Λ=461 nm.

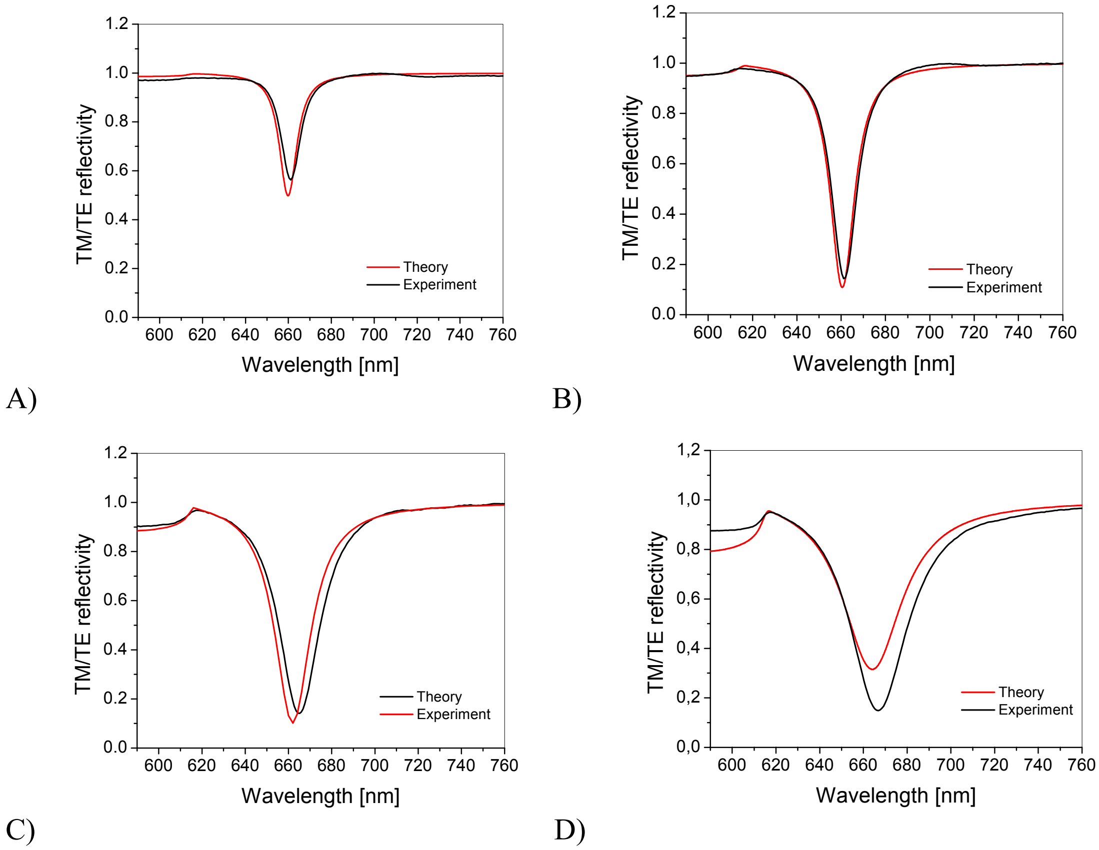

A) B) C) D)

Fig. 69 SPR wavelength reflectivity spectra measured on grating samples with different grating modulation amplitude a_1 (red curve) compared with simulations (black curve) for parameters stated in Tab. 12, normal incidence geometry, water in contact with the gold grating surface.

Reflectivity from prepared grating samples in wavelength and angular spectrum was measured using the setup described in Chapter 4.2.1. On each grating, a drop of de-ionized water was micropipetted and covered with a microscope cover-glass.

Obtained wavelength reflectivity spectra in Fig. 69 show that excitation SPWs on gold grating surface is manifested as an SPR dip centered at the wavelength 660 nm. When increasing the grating modulation amplitude the strength of coupling between the optical wave and SPW increases. These experimental results are in an excellent agreement with the theory as shown in Fig. 69. The theoretical curves were calculated by using the integral method and the grating modulation amplitude a_1 determined from the grating efficiency, see Tab. 12. In Tab. 13, the main parameters of SPR dip obtained experimentally and from the theory are compared: the average difference between theoretical and experimental SPR wavelength, SPR absorption dip width and SPR dip depth of 1 nm, 10 per cent, and 12 per cent was observed.

Grating	SPR wavelength Experiment/Theory	Depth of SPR dip Experiment/Theory	FWHM of SPR dip Experiment/Theory
A	660.9 nm / 660.0 nm	43% / 50 %	10 nm / 11 nm
B	660.9 nm / 660.2 nm	86 % / 90 %	13.2 nm / 12.7 nm
C	662.0 nm / 665.0 nm	85 % / 94 %	21.7 nm / 19.5 nm
D	665.4 nm / 664 nm	84 % / 67 %	30 nm / 30 nm

Tab. 13 SPR dip characteristics in wavelength reflectivity spectrum, sinusoidal diffraction gratings A-D with modulation amplitude a_1 stated in Tab. 12 .

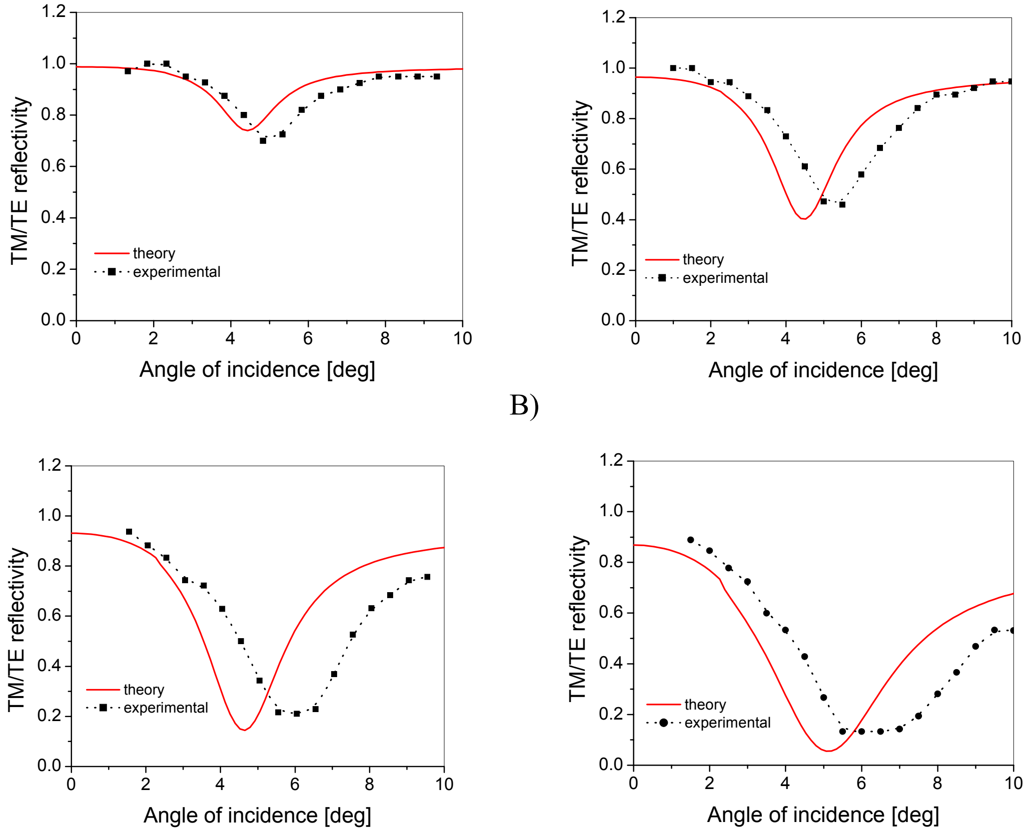

A) B) C) D)

Fig. 70 SPR angular reflectivity spectra measured from sinusoidal diffraction gratings with modulation amplitudes a_1 (black curve) and simulations (red curve) for parameters stated in Tab. 12; wavelength 632.8 nm, water on the top of the gold grating surface.

Similarly, SPR angular reflectivity spectra were measured, see Fig. 70. These results show a good agreement with theory - the difference between theory and experiment for SPR angle of incidence, SPR dip depth and SPR dip width was in average 1 deg, 11 per cent, and 30 per cent, respectively. The comparison between theoretical and experimental SPR reflectivity dip characteristics are summarized in Tab. 14.

Grating	SPR angle Experiment/Theory	Minimum of SPR dip Experiment/Theory	FWHM of SPR dip Experiment/Theory
A	5.0 deg / 4.4 deg	30 % / 20 %	2.3 deg / 1.8 deg
B	5.3 deg / 4.5 deg	45 % / 42 %	2.75 deg / 2.0 deg
C	6.0 deg / 4.6 deg	22 % / 16 %	3.4 deg / 2.6 deg
D	6.4 deg / 5.1 deg	85 % / 93 %	5.4 deg/ 3 deg

Tab. 14 SPR dip characteristics in angular reflectivity spectrum, sinusoidal diffraction gratings A-D with modulation amplitude a_1 stated in Tab. 12 ; wavelength 632 nm.

4.2.3 Diffraction gratings with different modulation profiles

To investigate the dependence of surface plasmon resonance on the modulation profile, four mirror-symmetric diffraction gratings with different surface modulations and identical depths were prepared. These gratings were holographically recorded using the protocol presented in Chapter 4.1.1. These gratings were made in the photoresist AZ1350 for exposition time from 20 sec to 500 sec and development time adjusted to achieve grating efficiency 6 per cent. For more detailed information on holographic grating profiles see Chapter 4.1.4.

The surface of prepared gratings was coated with gold (see Chapter 4.1.3) and analyzed by Atomic Force Microscope, see Fig. 63. Measured profiles of the set of gratings noted as I-IV are presented in Fig. 72. These results reveal that prepared gratings exhibited the grating modulation profile with narrow valleys and broad peaks. As shown in Fig. 72, the grating I has sinusoidal modulation and samples II-IV has modulation profile with increasing amplitudes of higher spatial frequencies a_2 and a_3. Modulation amplitude a_1 was approximately 14 nm and a_2 lied in the range from 0 to 4.2 nm, see Fig. 71 and Tab. 15.

No.	Modulation amplitude a_1 (from AFM)	Modulation amplitude a_2 (from AFM)
I	14 nm	0 nm
II	17 nm	0.8 nm
III	15 nm	2.4 nm
IV	12 nm	4.2 nm

Tab. 15 The modulation profile of grating samples I-IV decomposed into first two terms of Fourier series harmonics, Λ=442nm.

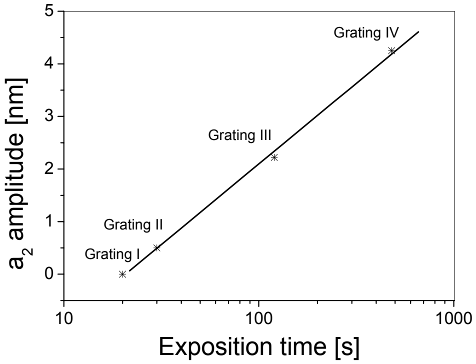

Fig. 71 Dependence of the amplitude a_2 on the development time, diffraction grating I-IV.

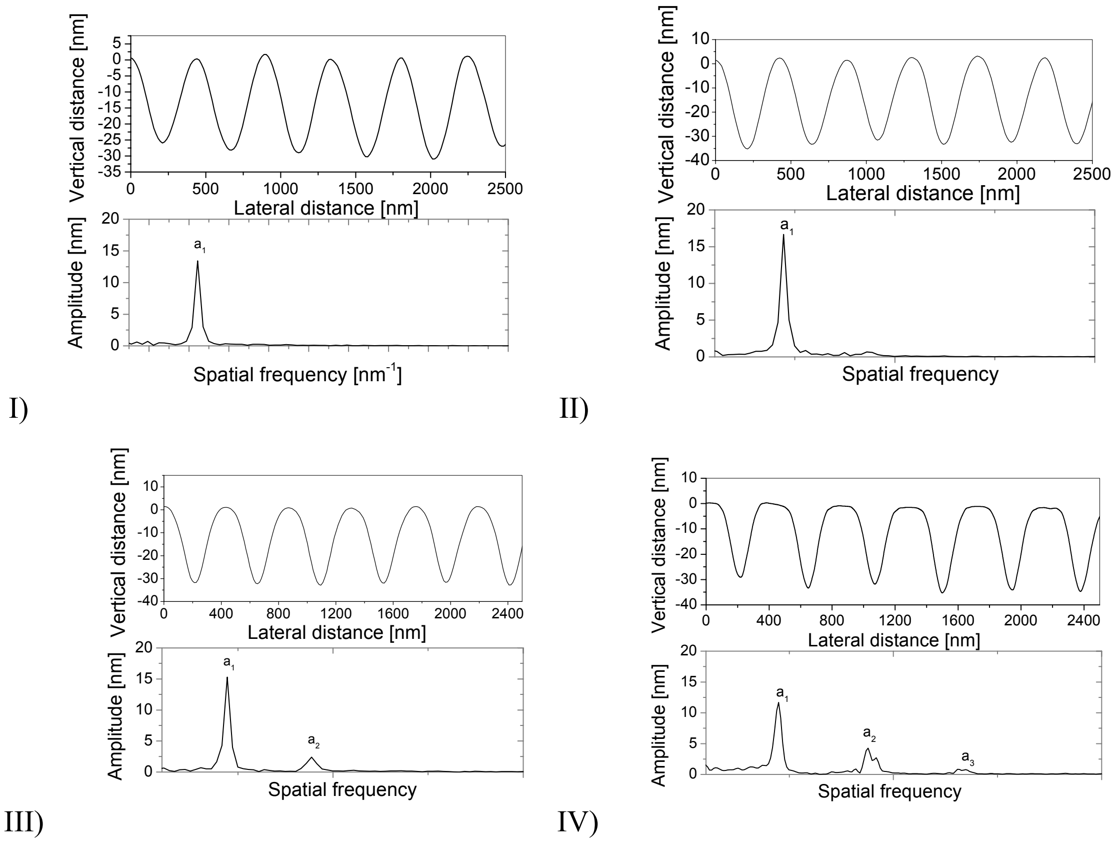

Fig. 72 Surface modulation profile of four gratings I-IV, each graph shows the dependence of grating surface height on the lateral distance perpendicular to the grating grooves (upper part of the graph), and the Fourier spectrum of the grating profile (bottom part of the graph). Grating modulation profile of gold coated grating was averaged over 700 nm perpendicular to the grating grooves.

From each diffraction grating I-IV, we measured the SPR wavelength reflectivity spectrum using the setup described in Chapter 4.2.1. Prior to the measurement, on the surface of each grating a drop of de-ionized water was micropipetted and covered with a microscope cover-glass. Obtained results presented in Fig. 73a reveal a shift of the SPR wavelength toward longer wavelengths when trenches in the grating profile become narrower. To compare the experimental results with the theory, SPR reflectivity spectra were simulated for studied gratings using the integral method and grating parameters stated in Tab. 15. Experimental SPR dips are broader and shifted by approximately 5 nm with respect to the ones obtained from simulations, see Fig. 73a and Fig. 73b. The reason for this discrepancy is probably due to surface roughness of diffraction gratings which was not accounted for in the theoretical model. Furthermore, gratings III and IV exhibited higher in-homogeneity in the grating modulation over the surface which resulted in an additional broadening of measured SPR reflectivity dips.

The observed shift in the SPR wavelength toward longer wavelengths occurring on gratings with “narrow valley” profile is due to the Bragg scattering of SPWs on the spatial frequency with the amplitude a_2 (see theory in Chapter 3.2.3). Measured dependence of SPR wavelength shift on a_2 amplitude exhibits the slope $\delta\lambda_{res}/a_2 = 4.0$, see Fig. 74. This value lies in the range predicted by simulations $\delta\lambda_{res}/a_2 = 3.1$ - 4.4 (see Chapter 3.2.3).

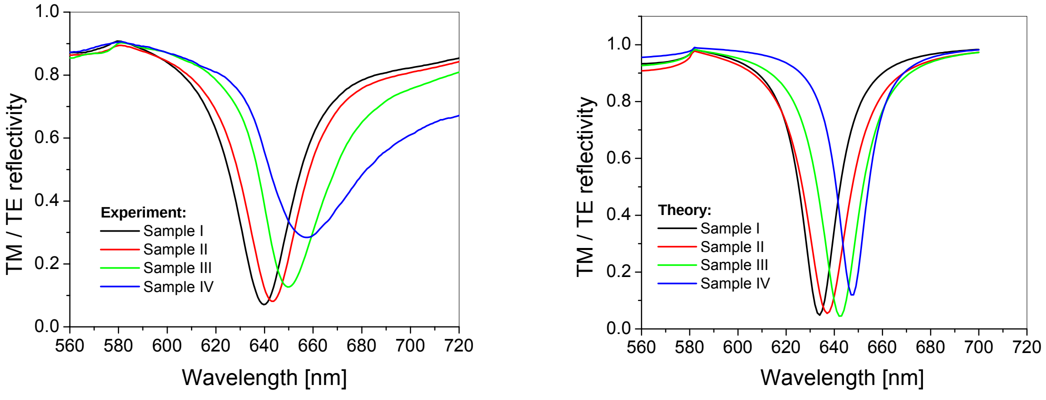

a) b)

Fig. 73 a) Experimental and b) theoretical SPR wavelength reflectivity spectra from gratings I-IV, normal incidence geometry, water in contact with the grating samples, grating period Λ=442nm.

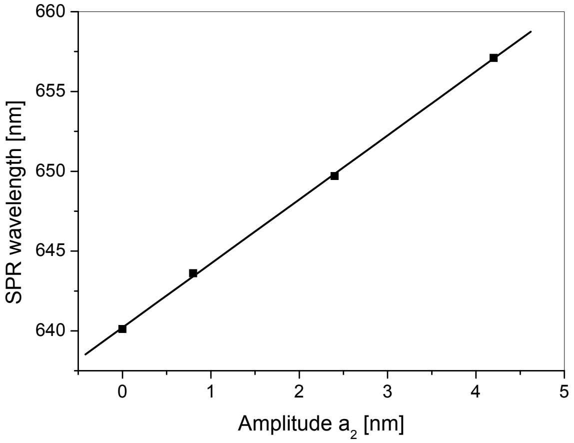

Fig. 74 Experimental dependence of the SPR wavelength on the spatial frequency amplitude a_2.

4.2.4 Sensitivity of SPR sinusoidal diffraction grating

Variations of SPR induced by changes in the refractive index at the diffraction grating surface were investigated experimentally. Effect of two types of refractive index variations were studied – homogenous refractive index changes in the whole dielectric (bulk changes) and refractive index changes occurring in the close proximity of the metal surface (surface changes).

This study was performed using a sinusoidal gold grating with modulation period Λ=459 nm and the amplitude a_1=12 nm. Sensitivity to changes in refractive index of whole dielectric adjacent to the grating surface (bulk refractive index sensitivity) was determined from SPR spectra measured when liquids with refractive index 1.333, 1.353 and 1.370 were brought in contact with the gold grating surface, see Fig. 75. Used liquids were prepared by mixing ethylene-glycol and water (with refractive index 1.41 and 1.333, respectively, at the wavelength 632.8 nm). From measured SPR dip shifts, the wavelength and angular bulk refractive index sensitivity $S_b^W=459$ nm RIU^{-1} and $S_b^A=78$ deg RIU^{-1} was determined, respectively. As shown in Tab. 16, experimental wavelength and angular bulk refractive index sensitivity was of 3 percent lower and of 8 per cent higher, respectively, when compared with the theory (see Chapter 3.3).

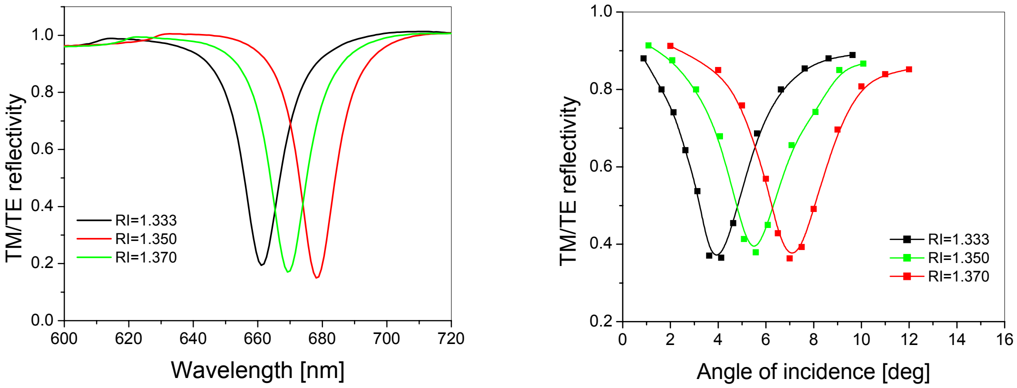

a) b)

Fig. 75 SPR reflectivity measured from sinusoidal diffraction grating (grating modulation period Λ=459 nm, grating modulation amplitude a_1=12 nm) for the dielectric refractive index 1.333 (black curve), 1.353 (green curve) and 1.370 (red curve): a) wavelength spectrum for normal incidence b) angular spectrum for the wavelength of 632.8 nm.

To determine surface refractive index sensitivity, time evolution of SPR angle of incidence and SPR wavelength was measured when protein monolayers were grown on the grating surface. This molecular assembly was successively grown from a citrate buffer solution (CB, pH 4.0) with dissolved bovine serum albumin (BSA, from Sigma) and dextran sulphate (DS, from Sigma). When BSA and DS solutions were alternately flowed across the sensor surface, stack of BSA monolayers interlinked with DS layers was formed on the sensor surface as BSA and DS are oppositely charged in CB buffer. Shifts in SPR angle of incidence and SPR wavelength induced by growth of protein layers are shown in Fig. 76a and Fig. 76b, respectively. The average shift in the resonant wavelength and angle of incidence produced by a single BSA layer was of 0.5 deg and 3.1 nm, respectively. Assuming the refractive index of 1.45-1.5 and the thickness 4-7 nm of the BSA monolayer [173], these SPR shifts correspond to the surface refractive index sensitivity in the range $S_s^A=0.4\text{-}1$ deg nm^{-1} RIU^{-1} and $S_s^W=2.8\text{-}6.5$ RIU^{-1}. The surface sensitivity obtained from the theory presented in Chapter 3.3 gives the sensitivity of $S_s^A=0.67$ deg nm^{-1} RIU^{-1} and $S_s^W=3.9$ RIU^{-1} which is in the measured range, see Tab. 16.

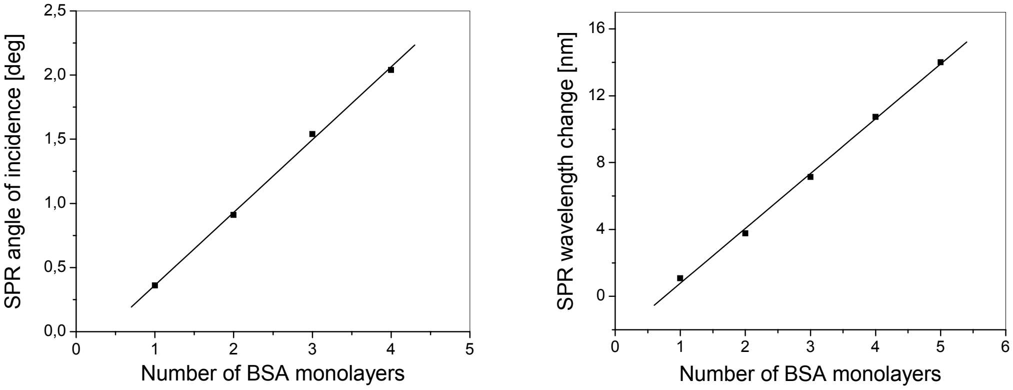

a) b)

Fig. 76 Measured shifts in a) SPR angle of incidence and b) SPR wavelength for a stack of BSA monolayers successively grown on a gold-coated sinusoidal grating, modulation period Λ=459 nm, modulation amplitude a_1=12 nm.

RI sensitivity	Theory	Experiment
Angular bulk, λ=632.8nm	S_b^A=72 deg RIU^{-1}	S_b^A =78 deg RIU^{-1}
Wavelength bulk, λ=660nm	S_b^W =459 nm RIU^{-1}	S_b^W =452 nm RIU^{-1}
Angular surface, λ=632.8nm	S_s^A=0.67 deg nm^{-1} RIU^{-1}	S_s^A =0.44-1 deg nm^{-1} RIU^{-1}
Wavelength surface, λ=660nm	S_s^W = 3.9 RIU^{-1}	S_s^W =2.8-6.47 RIU^{-1}

Tab. 16 Comparison of theoretical and experimental sensitivity of SPR wavelength and SPR angle of incidence to changes in surface and bulk refractive index; gold sinusoidal grating with the modulation period Λ=459 nm and the modulation amplitude a_1=12 nm.

4.3 SPR sensor device with an array of diffraction gratings

In this chapter, the implementation of diffraction gratings for multichannel SPR biosensor is described. A prototype SPR sensor device based on spectroscopy of surface plasmons on an array of diffraction gratings was developed. The sensor device consists of the following components: a) an *SPR sensor chip* with an array of sensing channels, b) a *fluidic system* for distribution of liquid samples on the sensor chip, c) an *SPR sensor chip reader* for real-time measurements of SPR changes on the sensor chip and d) a *data processing* for evaluation of the sensor response. Further, the integration of these components into an SPR sensor device is described and its accuracy for measurement of SPR angle of incidence is investigated.

4.3.1 SPR sensor chip

SPR sensor chip was fabricated on the top of a rectangular replica grating with dimensions of 32 x 15 mm. This grating was replicated into OGG-146 polymer from Epotek, USA, using the procedure described in Chapter 4.1.2. The grating had a sinusoidal surface modulation (with the period Λ=455 nm and modulation amplitude a_1=17 nm). A two-dimensional array of sensing channels was prepared on the replica by evaporating an adhesion promoting titanium layer and gold layer using procedure from Chapter 4.1.3 through a special mask. This mask encompassed two-dimensional array of rectangular windows lithographically fabricated into a 50 µm phosphor bronze sheet (prepared in Psoft Inc., Czech Republic). In this mask, the windows had dimensions 300 x 300 µm and were grouped into five areas with 6 columns and 14 rows. By using this mask, 420 gold-coated pads were prepared each of can support an individual sensing channel. In order to align the position of the evaporation mask on the replica grating, a special holder depicted in Fig. 77 was used. Blueprints of the holder components and used evaporation masks are attached in Appendix.

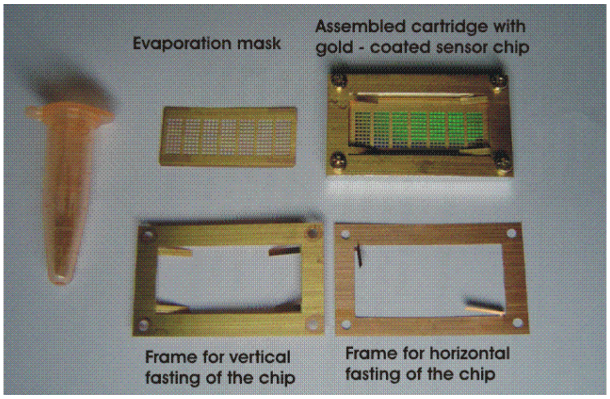

Fig. 77 Evaporation mask, alignment frames and the assembled holder for the preparation of an array of gold diffraction gratings on a replica grating.

4.3.2 SPR sensor chip cartridge and fluidic system

In order to distribute liquid samples on the array of sensing channels, the sensor chip was mounted into a cartridge in which its surface was interfaced with a fluidic system. The fluidic system was formed of three layers of a thin polymer (50 µm thick Mylar) attached to a plastic support with input and output ports for liquid samples (see Fig. 78). Into the Mylar layers, the channels and flow-chambers were cut. For better sealing of the fluidic system, polyurethane gaskets were attached on the top and bottom rims of the flow-chambers. The flow chambers were closed by the SPR sensor chip on the bottom and by a transparent cover-glass on the top. In order to reduce back reflections of light from the-cover glass, its bottom and top surface was coated with anti-reflection coating (prepared in VOD in Turnov, CZ).

Mylar sheets and polyurethane sheets were cut with a CO_2 laser beam by Micronics Inc. (Bothel, USA) and Medicom (Prague, CZ) according to the blueprints attached in Appendix. The middle Mylar layer (noted as 2 in the figure Fig. 78) included a thin self-adhesive layer on the both sides, the polyurethane sheets were coated with a self-adhesive layer on a single side, and the bottom and top Mylar layers (noted as 1 and 3) contained no adhesive. These layers were assembled on a plastic support using alignment pins. A prototype of the flow-cell with five flow-chambers was developed. Each flow-chamber was interfaced with 6 columns of diffraction gratings on the sensor chip and the depth and width of an individual flow-chamber was 350 µm and 3 mm, respectively. To flow liquid samples through the cartridge, their input ports were connected to multi-channel peristaltic pump Reglo (ISM 930 from Ismatec, Switzerland) by using Teflon tubing (1/16" OD 1527L from Upchurch Scientific, USA) and connectors (P-844x from Upchurch Scientific, USA). In order to assure the sealing of the flow-cell, we used clamping frame with four 60 N plungers (see the overall view of the sensor chip cartridge shown in Fig. 79).

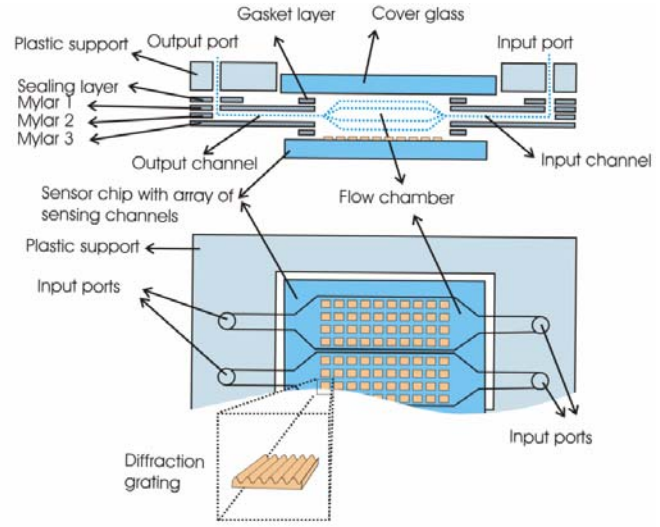

Fig. 78 **Cross section of a flow-cell for sample delivery to the array of diffraction gratings on the sensor chip.**

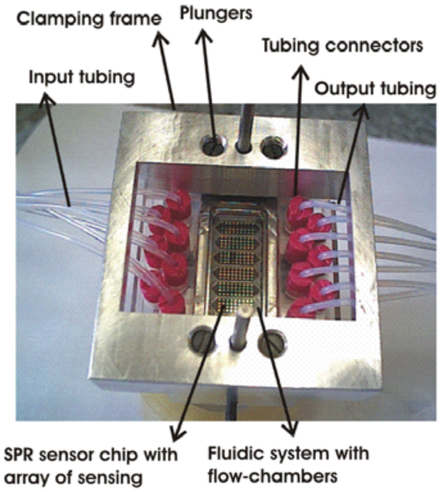

Fig. 79 **Overall view of the cartridge with SPR sensor chip and the fluidic system.**

4.3.3 SPR sensor chip reader

An SPR sensor chip reader was developed for reading of changes in SPR angle of incidence on the array of sensing channels. As shown in Fig. 80, the SPR sensor chip reader consists of three modules: *light-source* producing a beam of collimated monochromatic polarized light, *scanning optics* for scanning of the light beam across the sensor chip and *imaging optics* projecting the angular SPR reflectivity spectra on a two-dimensional detector. In this device, angular spectra of light reflected from an individual row of diffraction gratings (each diffraction grating supports and individual sensing channel) are projected at the detector. SPR spectra from multiple rows of diffraction gratings are projected on the detector using the imaging optics.

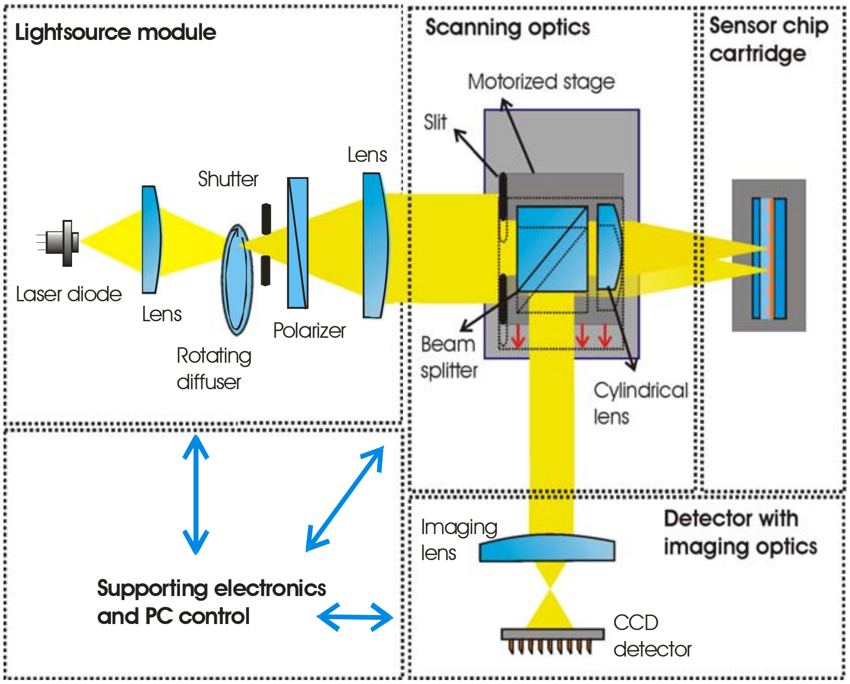

Fig. 80 The optical setup of SPR sensor chip reader.

A stabilized He-Ne laser (SL03 from Sios, Germany, λ=632.8 nm, power 2 mW) was used as a light-source. The wavelength 632.8 nm was used as it allowed simpler tuning of the prototype sensor device. The light beam from the He-Ne laser was focused on a rotating diffuser (grade 240 from Optosigma) using a plano-convex lens (focal length 50 mm, from Optosigma, USA) where it was scattered. The rotating diffuser allowed reducing the spatial coherency of the light for suppressing of parasitic patterns due to the diffraction on imperfections on optical components. The scattered light beam passed through a shutter (40Hz VS14/25 from Uniblitz, USA) and a dichroic polarizer. After, the light was collimated using a lens (focal length 150 mm) and it was launched into the scanning optics module.

In the scanning optics module a convergent light beam was produced by means of a cylindrical lens (focal length 150 mm, from Optosigma, USA). This beam was focused on a single row of sensing channels on the sensor chip. Upon the incidence, series of diverging beams (each originating from an individual channel) was reflected back into the scanning optics module. At each sensing channel, the light beam excites a SPW on a diffraction grating through the plus first and minus first diffraction orders. The excitation of surface plasmons is manifested as a drop in the intensity of the reflected light centered at two resonant angles. In the scanning optics module, series of reflected beams were separated from the incident light by using a cube beam splitter (cube side 30 mm, from Linos, UK). The scanning optics was mounted on a motorized translation stage (M-111.2DG from PI, Germany, scanning speed 1.5mm/s and accuracy of 0.9 microns) for sequential scanning of multiple rows on the sensor chip. The accuracy of the used translation stage was 0.9 µm for the acceleration 500000 counts s^{-2} (3.4 mm s^{-2}) and the velocity 290000 counts s^{-2} (2 mm s^{-2}). For each row of sensing channels, series of beams with encoded angular reflectivity spectra (the angular span of 5 deg) were projected on a two-dimensional photo-detector (DV434-FI, from Andor Technology, Ireland).The photo-detector was equipped with a CCD sensor with dimensions 13.3 x 13.3 mm, 1024 x 1024 pixels and 16 bit AD converter. The vertical readout speed of the detector was set to 16 and the horizontal readout time was set to 1. Typical exposition time was between 100 and 200 ms. The imaging optics consisted of two cylindrical plano-convex lenses (from OptoSigma, USA) with focal lengths of 200 mm and of 50 mm. The sensor chip cartridge was mounted on a system of XYZ linear stages (from Optosigma, USA) and a tilt (from Optosigma, USA) for its precise positioning and orientation. The overall view of the SPR sensor chip reader is presented in Fig. 81.

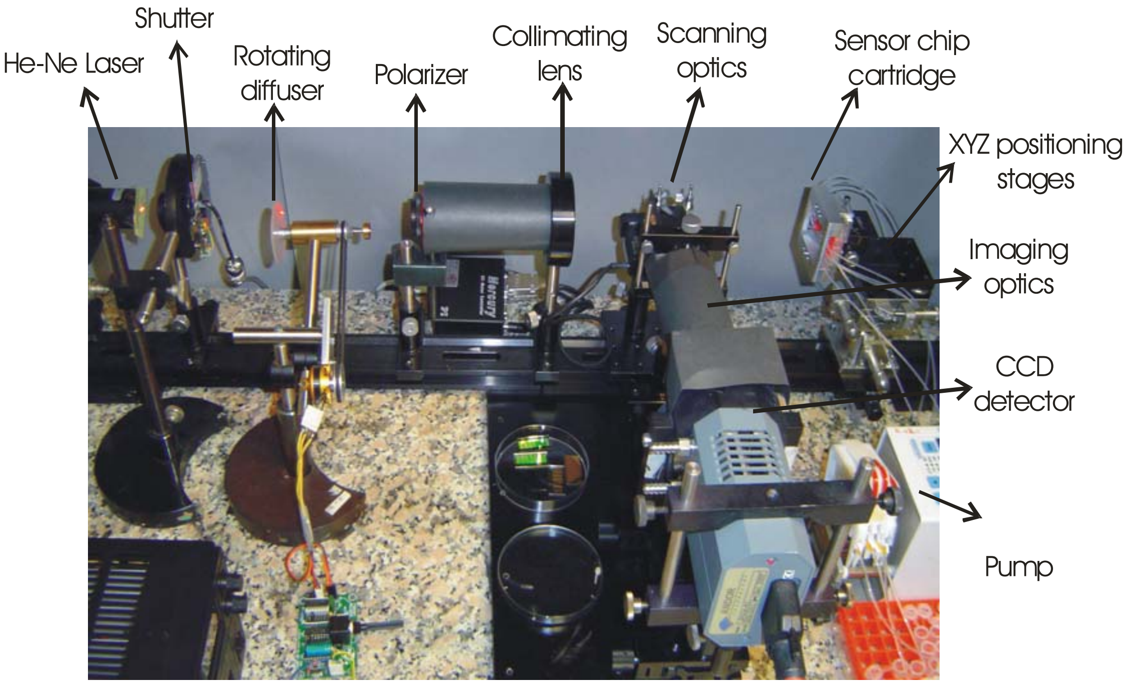

Fig. 81 SPR sensor chip reader.

In Fig. 82, typical SPR image from one row of sensing channels is presented. This figure shows series of horizontal bright strips each of which corresponds to an angular reflectivity spectrum originating from an individual sensing channel. Each strip contains two dark bands due to the excitation of surface plasmons through the plus first and minus first diffraction order. The angular span of the spectrum was from -2.5 deg to 2.5 deg.

4.3.4 Data processing

To evaluate changes in SPR spectra measured across the array of sensing channel, a special software for determining shifts in SPR angle of incidence was developed. This software was based on SPR-Spectral 1.20 program developed at IREE in Prague, into which a special module supporting communication with a CCD detector, shutter, and the motorized stage was integrated. This module also included tools for setting up parameters of SPR reader components (shutter, photo-detector and motorized stage), visualization of photo-detector output and definition of areas corresponding to individual sensing channels, see Fig. 82.

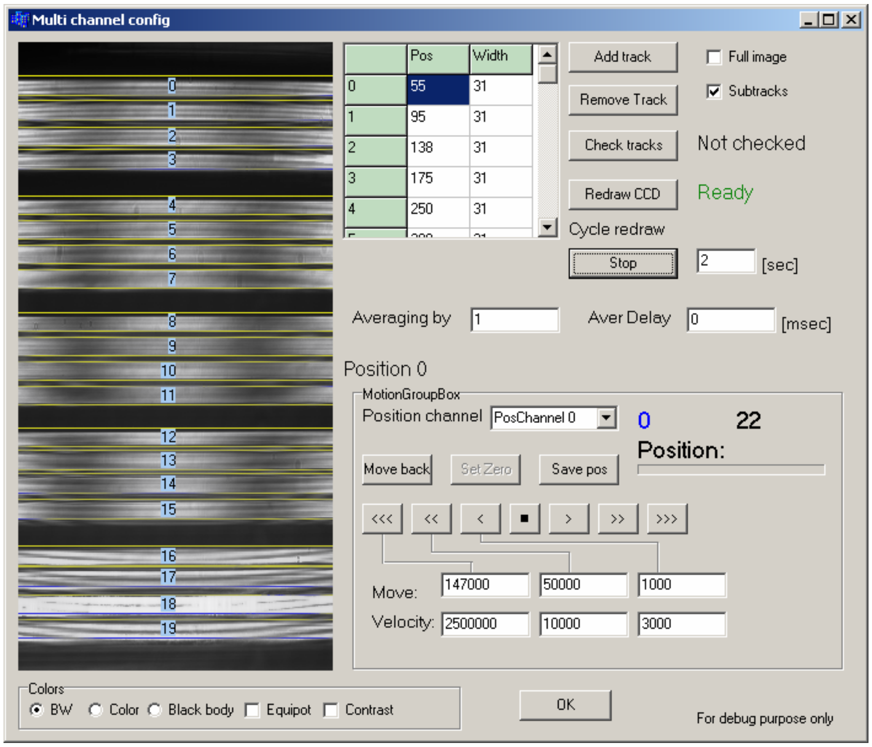

	Pos	Width
0	55	31
1	95	31
2	138	31
3	175	31
4	250	31

☐ Full image
☑ Subtracks
Not checked
Ready
Cycle redraw: 2 [sec]
Averaging by: 1
Aver Delay: 0 [msec]
Position 0
Position channel: PosChannel 0
0 22
Position:
Move: 147000 50000 1000
Velocity: 2500000 10000 3000
Colors: ● BW ○ Color ○ Black body ☐ Equipot ☐ Contrast
For debug purpose only

Fig. 82 SPR Spectral software dialog window for definition of strips of SPR spectra in an SPR image. SPR image is shown on the left hand side and the setting of data acquisition parameters are on the right hand side.

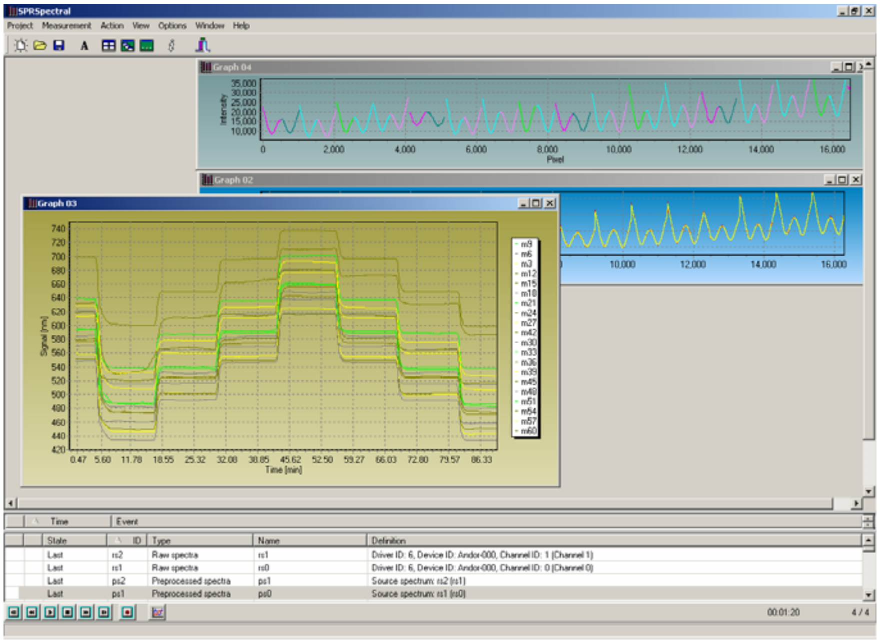

State	ID	Type	Name	Definition
Last	rs2	Raw spectra	rs1	Driver ID: 6, Device ID: Andor-000, Channel ID: 1 (Channel 1)
Last	rs1	Raw spectra	rs0	Driver ID: 6, Device ID: Andor-000, Channel ID: 0 (Channel 0)
Last	ps2	Preprocessed spectra	ps1	Source spectrum: rs2 (rs1)
Last	ps1	Preprocessed spectra	ps0	Source spectrum: rs1 (rs0)

00:01:20 4 / 4

Fig. 83 SPR spectral interface with raw spectra (top window), normalized spectra (middle window) and time-evolution of SPR sensor response acquired from multiple sensing channels (bottom window).

For each sensing channel, changes in SPR angle of incidence were calculated from the angular reflectivity spectrum acquired from the CCD detector (see Fig. 82). The spectrum strip located in acquired SPR image was averaged over the lines perpendicular to the stripe (n_A pixels), accumulated in time (n_T images) and boxcar-smoothed over 50 pixels. Raw SPR spectra measured in TM polarization were normalized with reference spectra measured in TE polarization and compensated for a detector dark current and stray light. The SPR angle of incidence was determined from normalized SPR reflectivity spectrum as the minimum of SPR dip by using a polynomial regression method, [166]. A change in the sensor response Θ was calculated as a shift in the angular distance between the two SPR dips associated with the excitation of SPW through the plus first and minus first diffraction orders (see Fig. 84).

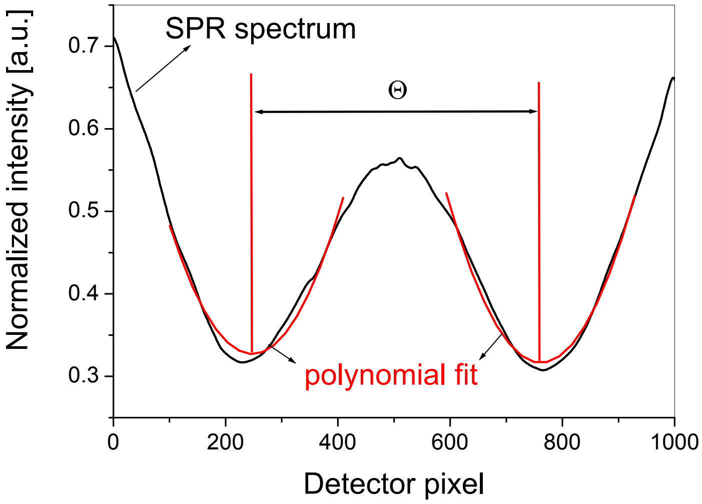

Fig. 84 A typical SPR spectrum from an individual sensing channel with gold surface and a liquid with refractive index of 1.332 flowed through the sensor. The spectrum was averaged over n_A=10 pix, time accumulation was n_T=5, boxcar smoothing over 50 pix was applied.

4.3.5 Accuracy in determining the SPR angle of incidence

In this section, let us investigate the accuracy with which the SPR reader determines the SPR angle of incidence. This parameter of the SPR sensor depends on (i) the performance of key components of SPR sensor device and on (ii) the setting of parameters for the acquisition of SPR spectra.

The key components of the SPR sensor device include the light-source, CCD detector and the translation stage. We found, that the accuracy of SPR angle measurement was not affected by scanning the light beam between multiple rows of sensing channels with the velocity and acceleration parameters specified above. As a light-source, we used frequency stabilized He-Ne laser operating at the wavelength 632.8 nm. The wavelength stability of this laser was better than 0.01 pm over 1 min. As predicted by theory, for small wavelength changes $\delta\lambda$ the SPR angle of incidence follows the slope $\delta\Theta/\delta\lambda \sim 0.32$ deg nm^{-1}. Therefore the wavelength fluctuations at the level of about 0.01 pm induce SPR angle variations of about 3×10^{-3} mdeg. Performed experiments revealed that dominant contribution to noise of CCD detector output is the shot noise which is characterized by standard deviation proportional to the square root of intensity of light. For used CCD detector, the standard deviation of the detector output was equal to $\sigma_I = 0.66\sqrt{I}$, where I is measured intensity in counts. At the saturation intensity (65536 counts) the signal to noise ratio was 0.26 per cent. It was possible to reduce the standard deviation of measured intensity by averaging over detector pixels or by accumulation of intensity over time $\sigma_I = 0.66\sqrt{I}/\sqrt{n_T n_A}$. The effect of shot noise to the accuracy in determining of the SPR angle of incidence was theoretically investigated in Chapter 3.4.2.

Further, we experimentally investigate the effect of the setting of parameters for SPR spectra acquisition to the accuracy in determining of the SPR angle of incidence. For different averaging n_A and time accumulation n_T, we acquired time evolution of SPR spectra while a liquid with a constant refractive index was flowed over the sensor surface. From these SPR spectra, the evolution of resonant angle of incidence Θ was determined using the data processing method described in Chapter 4.3.4. Without averaging and accumulation (n_T=1 and n_A=1 pix), SPR angle Θ was determined with the standard deviation σ_Θ=0.17 pix (0.8 mdeg). Using the experimentally determined characteristics of SPR dip (see Fig. 84 and Tab. 17) and measured signal to noise ratio of the CCD detector, the standard deviation of about $\sigma_\Theta=\sqrt{2}\,\sigma_\theta$=0.14 pix (0.7 mdeg) is obtained from theoretical Equation (3.13). This value is in good agreement with the experiment and it indicates that main factor limiting the sensor accuracy is shot noise of the CCD detector. The noise contribution caused by the light-source instabilities is two orders of magnitude below this value and the diffuser and translation stage were found to do not affect the noise of the acquired signal. The observed discrepancy between the experiment and simulations is mostly due to the deviation of measured SPR spectra from Lorentzian function for which the model was derived. As shown in Tab. 18, the standard deviation σ_Θ was reduced below 0.01 pix (of about 0.05 mdeg) when applying accumulation and averaging n_T=100 and n_A=100 pix, respectively.

Reflectivity angular span	1024 pix (5 deg)
SPR dip width	250 pix (1.1 deg)
SPR dip depth	0.3
Signal to noise ratio at maximum reflectivity	0.3%

Tab. 17 Parameters of SPR spectra acquired for an individual sensing channel; see Fig. 84. For definition of these parameters see Chapter 3.4.2.

Accumulation	Averaging	Standard deviation σ_Θ
n_T=1	n_A=1	0.170 pix (0.8 mdeg)
n_T=1	n_A=15	0.045 pix (0.25 mdeg)
n_T=1	n_A=100	0.020 pix (0.1 mdeg)
n_T=5	n_A=15	0.020 pix (0.1 mdeg)
n_T=10	n_A=100	0.009 pix (0.04 mdeg)

Tab. 18 Standard deviation of SPR angular distance Θ for different accumulation and averaging of SPR spectrum.

4.4 Characterization of the SPR sensor refractometer

In this section, let us determine the main performance characteristics of the developed SPR sensor device including the sensitivity to refractive index changes, the operating range, the sensor time resolution, refractive index resolution, and the reproducibility of the measurements across the array of sensing channels.

4.4.1 Refractive index sensitivity

In order to determine the *bulk refractive index sensitivity* of the developed SPR sensor device, we measured angular SPR reflectivity spectra when liquids with different refractive indices (mixtures of water and diethylene glycol) were flowed over the sensor surface (see Fig. 85). The SPR angle changes $\delta\Theta$ in these spectra were evaluated using the data processing method described in Chapter 4.3.4.

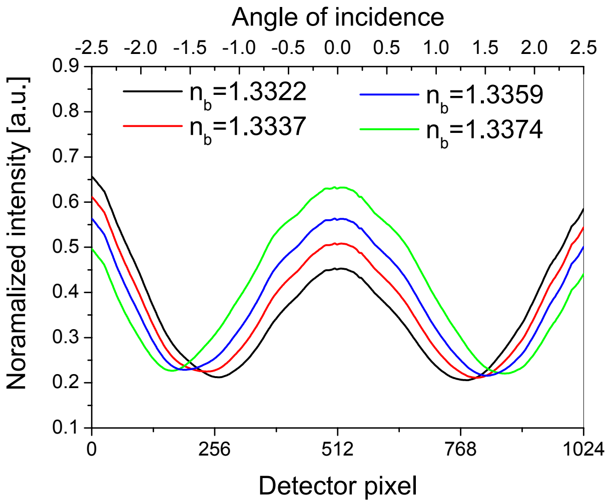

Fig. 85 SPR spectra acquired from an individual sensing channel for liquids with four different refractive indices flowed over its surface; averaging of the spectrum n_A=10 pix, time accumulation n_T=5, boxcar smoothing 50 pix.

Obtained sensorgram presented in Fig. 86a reveals that the SPR angle of incidence changes linearly with the bulk refractive index. Measured slope coefficient $S_b=\delta\Theta/\delta n_b$ lies in the range S_b=32-36 kpix RIU^{-1} which corresponds to the bulk refractive index sensitivity $S^A{}_b$=78-88 deg RIU^{-1}. This value is in good agreement with the theory predicting $S^A{}_b$ =72 deg RIU^{-1} (see Chapter 3.3.2). To determine the *surface refractive index sensitivity*, we monitored changes in the SPR angle of incidence while a protein monolayer (bovine serum albumin - BSA, from Sigma) was grown on the sensor surface. This layer was non-specifically bound from a citrate buffer solution (CB, pH 4.0) in which BSA was dissolved at the concentration of 100 µg ml^{-1}. The sensorgram acquired during the BSA monolayer growth shows the SPR angle shift $\delta\Theta$ = 110 pix (0.53 deg), see Fig. 85b. Assuming the BSA monolayer has refractive index of 1.45-1.5 and the thickness 4-7 nm [173], the measured sensor response corresponds to the surface refractive index sensitivity S_s=92-260 pix nm^{-1} RIU^{-1} and to the angular surface refractive index sensitivity S_s^A=0.44-1.23 deg nm^{-1} RIU^{-1}. The angular surface refractive index sensitivity obtained from theory is equal to 1.32 deg nm^{-1}, see Equation (3.8).

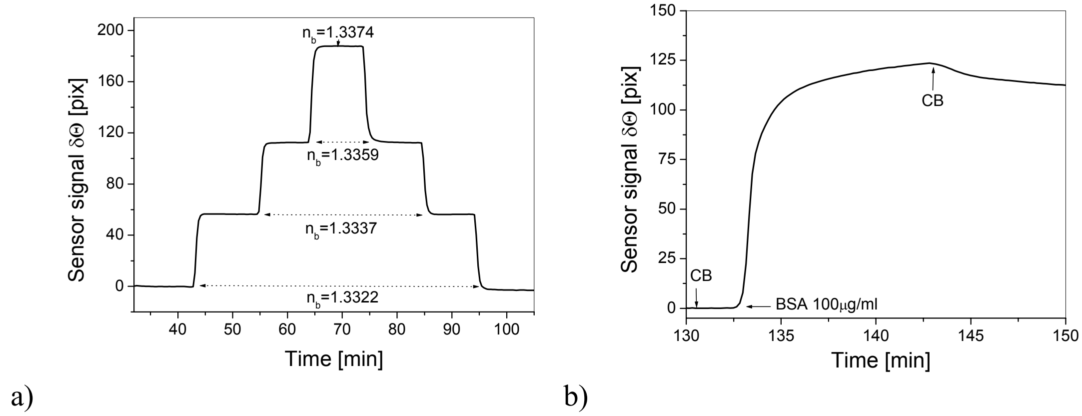

Fig. 86 SPR sensor response from an individual sensing channel for a) bulk refractive index change due to flow of four liquids with different refractive indices through the sensor and b) for the growth of a BSA monolayer on the sensor surface; time accumulation n_T=5, averaging n_A=10.

We can observe that measured surface and bulk refractive index sensitivity is higher then predicted by the theory. The reason for this discrepancy is due to the overlap of SPR dips in angular spectra from which the sensor output is determined as the difference between SPR dip minima Θ (see Fig. 84). For small Θ, the shape of SPR dips are changed leading to a lower distance between the SPR dip minima when compared with the true angular distance between SPR angles of incidence. This effect is decreased when increasing the SPR dip distance Θ.

4.4.2 Operating range

Let us define the SPR sensor angular range as the range of values Θ, for which the difference between the SPR reflectivity spectrum in the middle and on its edges (angles of incidence 0 deg at 512 pix and ± 2.5 deg at 0 and 1024 pix) differs less than 50 per cent. The experiments shown previously reveal that such defined SPR sensor angular range is of about 1 deg. By using sensitivity determined in previous chapter, this range corresponds to the bulk refractive index operating range of 0-5×10^{-3} RIU and to the protein coverage operating range of 0-5 ng mm^{-2} (see Tab. 19 and Chapter 3.4.1).

Bulk refractive index sensitivity S_b	32-36 kpix RIU^{-1} (156-175 deg RIU^{-1})
Surface refractive index sensitivity S_s	92-260 pix nm^{-1} RIU^{-1} (0.45-1.23 deg nm^{-1} RIU^{-1})
SPR sensor angular range	200 pix (1 deg)
Bulk refractive index operating range	5×10^{-3} RIU
Protein coverage operating range	5 ng mm^{-2}

Tab. 19 Sensitivity and the operating range of the developed SPR sensor device.

4.4.3 Time resolution

The minimum repetition time with which the sensor can acquire the response is further reffered as to the *time resolution*.

In general, the time resolution depends on the number of sensing channels and accumulation. In order to evaluate this parameter, we acquired the sensor signal from different number of sensing channels and different accumulation n_T. First, we acquired the sensor signal from 30 channels arranged in a single row on the sensor chip (SPR scanning optics was not moving). Obtained results shown in Tab. 20 reveal that for the accumulation in the range n_T=1-10 the time resolution lied between 1.8-11.5 seconds. The time for readout of sensor signal from an individual row of sensing channels included data transfer from the CCD detector to SPR spectral software (1.3 seconds per SPR image), exposure of the detector to light reflected from the sensor chip (200 ms) and evaluating an SPR angular spectra using the polynomial fitting (approximately 10 ms per spectrum per spectrum). After, we tested the time resolution when SPR spectra were measured from multiple rows (SPR scanning was moving). As shown in Tab. 21, the sensor signal was acquired in 3 seconds per an individual rows (each row contained 30 sensing channels) when no accumulation was applied (n_T=1).

Accumulation n_T	Time resolution
1	1.8 sec
5	6.0 sec
10	11.5 sec

Tab. 20 Time resolution for the SPR sensor response read from 30 channels in a single row, n_A=10.

Number of rows	Number of channels	Accumulation n_T	Repetition time
2	60	1	5.1 sec
5	150	1	15 sec
10	300	1	30 sec

Tab. 21 Time resolution for the SPR sensor response read from multiple rows of sensing channels; each row supported with 30 channels, n_A=10.

4.4.4 Refractive index resolution

The refractive index resolution is the parameter describing the minimum change in the bulk refractive index measurable with the SPR sensor device. This refractive index resolution is defined as the ratio σ_Θ/S_b, where σ_Θ is the standard deviation in the sensor signal Θ and S_b is the bulk refractive index sensitivity. When using averaging n_A=10 pix and accumulation time n_T=5, the refractive index resolution to 7×10^{-7} RIU is achieved. By using the Equation (3.10) derived in Chapter 3.4.1, this value corresponds to the resolution in measurement of protein surface coverage on the sensor surface of about 0.5 pg mm^{-2}. The sensor resolution for different accumulations can be obtained from the data presented in see Tab. 18 and Tab. 19.

4.4.5 Reproducibility

In this section, the reproducibility of the SPR sensor measurements across the array of sensing channels is investigated. In order to evaluate this parameter, we compared the sensor response acquired from different sensing channels to identical refractive index variations.

In this experiment, liquids (mixtures of water and ethylene glycol) with different refractive indices were flowed across the surface of the sensor chip followed with a growth of bovine serum albumin (BSA) monolayer from phosphate buffer (PBS). Sensorgrams measured in different sensing channels for these bulk and surface refractive index changes are presented in Fig. 87 (accumulation n_T=5, averaging n_A=10). In this figure, data from a single row with 30 sensing channels are shown (sensor response from other rows exhibited similar behavior). These data exhibit the variability in the surface and bulk refractive index sensitivity across sensing channels of about 7 per cent (standard deviation). Besides the variations in the sensitivity, the accuracy of determination of the resonant SPR angle also varies across the array of sensing channels. In the performed experiment, the SPR angle of incidence was determined with the average accuracy 0.05 pix. This value corresponds to the average sensor refractive index resolution of 1.3 10^{-6} RIU, the standard deviation of the refractive index resolution was 0.4 10^{-6} RIU. These variabilities were due to imperfections of the gratings across the sensor chip, misalignments of optical components, instabilities in the optical reader and fluctuations caused by passing of light through flowed liquid samples. For illustration of the effect of these imperfections, typical SPR spectra acquired from a row of six channels and from a column of five channels located in an individual flow-chamber are presented in Fig. 88.

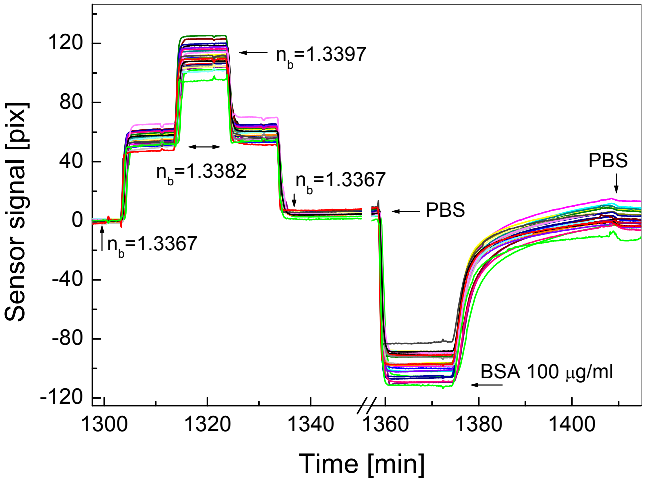

Fig. 87 Sensor response from 30 channels in a single row on a sensor chip to identical changes in the bulk refractive index and a growth of a thin protein layer on its surface.

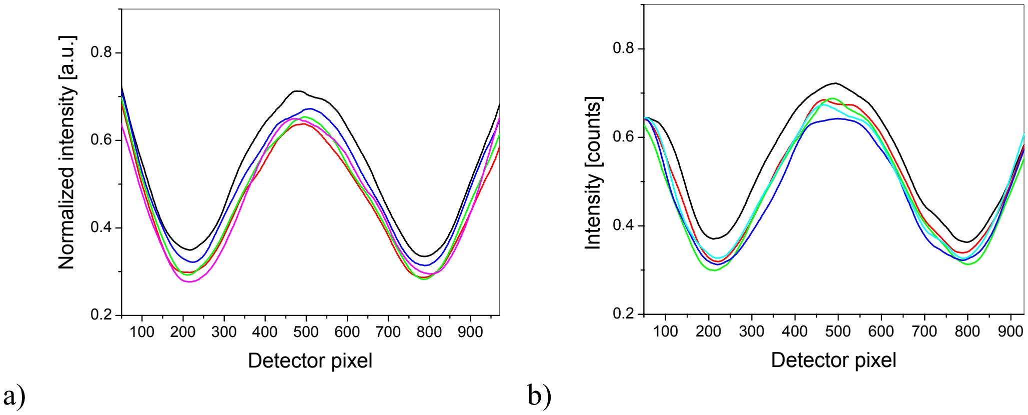

Fig. 88 Comparison of SPR spectra measured from: a) six gratings located in a single row in an individual flow-chamber, b) five gratings located in a column in an individual flow-chamber; averaging n_A=10, accumulation n_T=5, boxcar smoothing over 50 pix

4.4.6 SPR sensor based on an array of diffraction gratings - summary

Sensing device based on spectroscopy of surface plasmons on an array of diffraction gratings was developed. This sensor encompasses a sensor chip produced by replication of a holographic diffraction grating on which an array of gold pads was prepared (see Chapter 4.3.1). For delivery of liquid samples to sensing channels formed by the array of metallic gratings, the sensor chip was interfaced with a fluidic system (see Chapter 4.3.2). For readout of changes in the SPR angle of incidence on the array of sensing channels, an SPR sensor chip reader was developed (see Chapter 4.3.3). By sequential scanning of rows of 30 sensing channels (time multiplexing), reading of up to 150 sensing channels was achieved. The refractive index resolution and the time required for the sensor chip reading (time resolution) depend on the number of evaluated channels. For the time resolution of 6 seconds, the sensor provided 30 channels with the refractive index resolution as small as 7×10^{-7} RIU (channels in a single row were read with the accumulation n_T=5, averaging n_A=10). For the time resolution of 16 seconds, the sensor allowed measurement from 150 channels with the refractive index resolution of 1.5×10^{-6} RIU (channels in five rows were read without accumulation n_T=1, averaging 10). Mainly due to imperfections on the sensor chip, instabilities of the sensor system, and due to passing of the light through flowed samples, refractive index resolution (averaged over the sensing channels) was typically deteriorated by the factor of 2 with respect to the upper values.

4.5 Application of the SPR sensor device to biosensing

To demonstrate potential of the developed SPR sensor device for biosensing, we performed a model experiment in which hormones related to female cycle were directly detected by using antibody recognition elements. In following sections, (i) the procedure employed for immobilization of antibodies on surface of individual sensing channels is described and (ii) detection of selected hormones using the SPR biosensor with antibodies immobilized on its surface is performed.

In the experiment, we used four individual sensing channels located in four flow-chambers through which liquid samples were flowed at the flow-rate 30 μl min^{-1}. In each sensing channel, we applied averaging n_A=50 pixels and time accumulation n_T=5 to SPR spectra from which variations on the SPR angle of incidence were determined. In the experiment, following compounds diluted in citrate buffer, 0.1 M, pH 4 (CB) and phosphate-buffered physiological saline, pH 7.4 (PBS) were used. Human choriogonadotropin (hCG), monoclonal antibody against β subunits of human choriogonadotropin (a-hCG), follicle stimulating hormone (FSH) and monoclonal antibody against follicle stimulating hormone (a-FSH) were obtained from Biodesign, USA. Monoclonal antibody against horse radish peroxidase (a-PX) was from Seva Immuno, Czech Republic. Dextran sulfate sodium salt (DS; from dextran with an average molecular weight of 10 000), bovine serum albumin (BSA; 99% by electrophoresis), and glutaraldehyde (GA) were from Sigma.

4.5.1 Immobilization of antibodies on the sensor chip

To apply the developed SPR biosensor for detection of female cycle hormones hCG and FSH, the sensor surface were coated with antibodies a-hCG (in one channel), a-FSH (in one channel) and a-PX (in two channels). Antibodies a-hCG and a-FSH were used for specific capture of corresponding hormones from analyzed solutions and a-PX antibody was employed as the reference. Prior to the immobilization of a-hCG, a-FSH and a-PX, the sensor chip was cleaned in ozone cleaner (UVO Cleaner 42-220 from Jelight Company, Inc.) washed with deionized water and dried in a nitrogen stream. The immobilization of a-hCG, a-FSH and a-PX antibodies in different sensing channels was performed from a-hCG, a-FSH and a-PX solutions flowed through corresponding flow-chambers. These antibodies were anchored on the sensor surface in cross-linked two-layer molecular assemblies (the procedure is described in detail in the reference [120]).

On the gold surface, assemblies consisting of alternating BSA, DS and antibody layers were formed by alternating adsorption from BSA, DS and antibody solutions. Initially, a BSA monolayer was adsorbed on the gold surface from BSA solution (concentration of 0.1 mg/ml in CB) flowed for 20 min through flow-chamber. Then, DS layer was adsorbed on the BSA layer from DS solution (concentration 1 mg/ml in CB, 5 minutes flow through a flow-chamber). After, an antibody layer was adsorbed on DS layer from an antibody solution (concentration 0.1 mg/ml in CB, 20 minutes flow through a flow-chamber). Between injecting these solutions, the sensor surface was washed with CB. The BSA layer was bound on the gold surface mainly due to the hydrophobic interaction. The assemblies of BSA, DS and antibody layers were formed due to electrostatic attraction between DS polyanions and BSA and antibody molecules positively charged below their isoelectric point in CB at pH 4. GA was used to crosslink covalently the assemblies through reactive amino-groups of

BSA and antibodies. Finally, PBS with pH 7.4 was flowed over the sensor surface in which the net electrical charge of used proteins reverted to a negative one and DS polyanions were expelled from the protein network.

The immobilization of antibodies on the sensor surface was performed in-situ and each immobilization step was monitored using the SPR sensor device. Sensorgrams measured for the growth of a-hCG and a-FSH assemblies from solutions prepared in CB are shown in Fig. 89 (injecting of each solution is clearly marked in the graph). These data reveal that the immobilization of a-hCG and a-FSH antibodies at the sensor surface produced a sensor response of about 210 pixels (a-PX antibody not shown in the graph produced similar sensor response). When PBS was flowed over the sensor surface, a decrease in the sensor signal is observed due to the different refractive indices of PBS and CB and due to the desorption of loosely bound molecules. After CB was injected again into the sensor, we observe the difference in the SPR sensor signal acquired before and after the flow of PBS of about 80 pixels. This SPR signal shift corresponds to the release BSA and antibody molecules from the sensor surface due to reverting the net electrical charge in the assemblies.

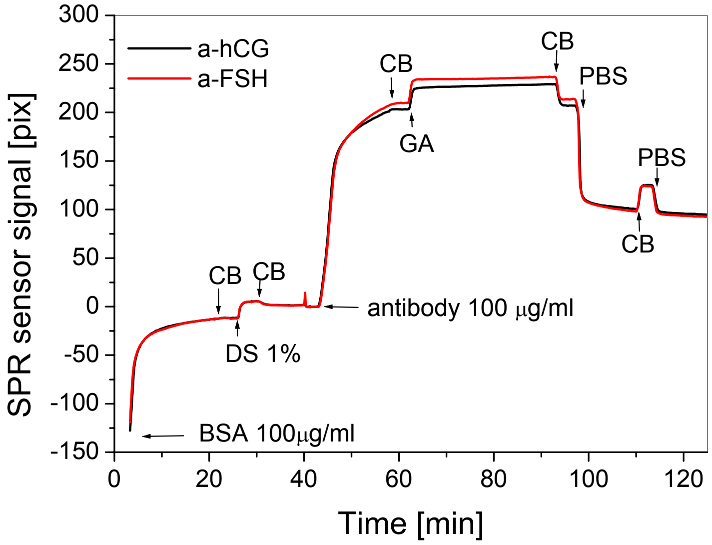

Fig. 89 **SPR sensor signal acquired during the immobilization of a-hCG and a-FSH antibodies on the sensor surface.**

4.5.2 Detection of female hormones using antibodies

Prior to the detection of hCG and FSH using the respective antibodies on the sensor surface, BSA dissolved in PBS at the concentration of 100 µg ml^{-1} (PBS-BSA) was flowed across the sensor surface. We observed no increase in the sensor response due to binding of BSA from PBS-BSA onto surface with a-hCG, a-FSH and a-PX antibodies. Therefore, we can assume that solid coating of the sensor surface with protein two-layer was produced preventing the non-specific binding of biomolecules.

The further experiment was performed in the PBS-BSA to reduce the binding of analyte molecules to the surface of tubing connected to the flow-cell. Initially, PBS-BSA buffer was flowed through the sensor for 5 min to establish sensor signal baseline. Then, solution with the analyte was flowed through the sensor for 10 min and binding of hormone to respective antibody and to reference antibody was measured. After the binding, the sensor surface was washed with PBS-BSA for 5 min. Fig. 90a shows the sensor response measured for successive binding of FSH dissolved in PBS-BSA at concentrations 125 ng ml^{-1}, 500 ng ml^{-1} and 2.5 μg ml^{-1} to a-FSH and a-PX antibody. The SPR sensor signal from the channel with a-FSH antibody was subtracted from the one in reference channel with a-PX antibody yielding the sensor response of 0.95, 2.6 and 11.1 pixels for the concentration 125 ng ml^{-1}, 500 ng ml^{-1} and 2.5 μg ml^{-1}, respectively. Similarly, Fig. 90b shows the time-evolution SPR sensor signal to successive binding of hCG from solutions with hCG dissolved in PBS-BSA at concentrations 25, 125 and 500 ng ml^{-1} to a-hCG and a-PX antibody. The SPR sensor response due to binding of hCG at the concentration of 25, 125 and 500 ng ml^{-1} was 2.4, 8.9 and 12.2 pixels, respectively.

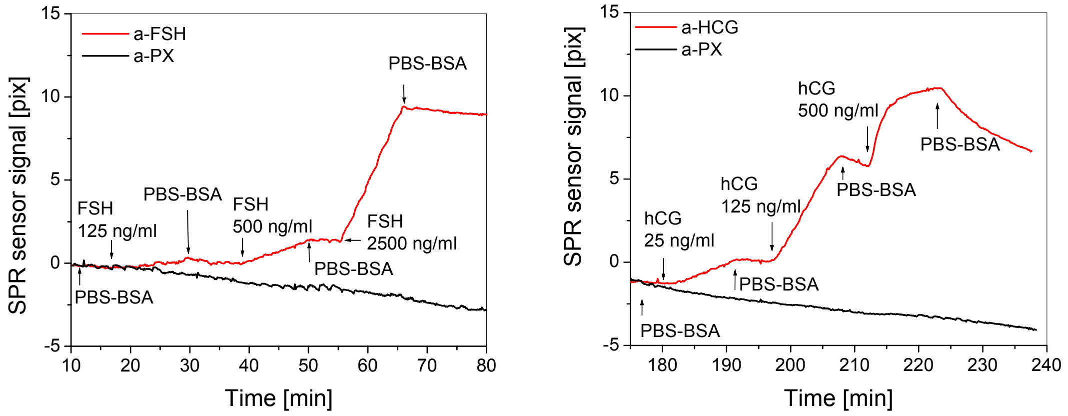

a) b)

Fig. 90 SPR sensor signal acquired for binding of a) FSH and b) hCG to its respective antibody and reference a-PX antibody immobilized on the sensor surface. Binding of FSH and hCG was performed from solutions with the analyte dissolved in PBS-BSA at increasing concentrations clearly marked in the graph.

Further, let us determine the detection limit of the presented SPR biosensor for detection of hCG and FSH. Detection limit of the biosensor is defined as $3\sigma_\Theta\times(\Delta\Theta/c)^{-1}$, [175], where σ_Θ is the standard deviation of the SPR sensor signal Θ and $\Delta\Theta/c$ is the slope of the sensor calibration ($\Delta\Theta$ is the sensor response and c is the concentration of analyte in the analyzed sample). The standard deviation of SPR sensor signal was σ_Θ =0.025 pix in the performed experiment. From the sensor response measured for the lowest concentrations of FSH and hCG, we estimated the sensor calibration slope as 7.6×10^{-3} and 0.1 ng^{-1}ml pix, respectively. By using these parameters, the detection limit for hCG and FSH of 0.6 and 9 ng ml^{-1}, respectively, was achieved. The detection limit for hCG is close to value 0.5 ng ml^{-1}, which is to our knowledge the lowest reported detection limit for hCG achieved with an SPR biosensor and direct detection [176].

5 Conclusions

In this work, a novel high-throughput surface plasmon resonance (SPR) biosensor platform was developed. This platform is based on an array of diffraction gratings each of which serves as an independent sensing channel. Refractive index variations on the array of sensing channels are simultaneously measured using the angle-modulated spectroscopy of surface plasmons and spatial and time multiplexing of sensing channels.

In the theoretical part of the work, the phenomenon of surface plasmon resonance on diffraction gratings was investigated using analytical and numerical methods. The optimization of a diffraction grating for SPR biosensor relying on angle-modulated spectroscopy of surface plasmons was carried out. In the experimental work, holographic diffraction gratings were prepared, replicated and characterized. Optimized diffraction grating structures were implemented in a SPR sensor device for measurement of refractive index changes on an array of sensing channels. A sensor chip cartridge including a sensor chip with a two-dimensional array of metallic diffraction gratings interfaced with a fluidic system for delivery of liquid samples was designed. An SPR reader was developed for measurement of changes in the SPR angle of incidence on an array of sensing channels. Potential of the developed sensor platform for biosensing was demonstrated in an experiment in which hormones related to female cycle were detected.

The SPR sensor device enabled parallel detection in up to hundreds of sensing channels with the accuracy in the measurement of protein coverage changes at the sub pg mm^{-2} level. In comparison with current state-of-the-art SPR biosensors, the developed SPR sensor platform offers a comparable accuracy in measurement of refractive index changes and an order of magnitude higher number of sensing channels. In conjunction with the technology for preparation of arrays of biomolecules on the sensor surface (e.g. contact or inject spotting), this SPR sensor platform holds the potential for high-throughput monitoring of biomolecular interactions needed in important fields including proteome research and drug discovery.

5.1 Future research

The future development of the SPR sensor device will be aimed towards further improving the refractive index and time resolution, number of sensing channels as well as to achieve higher stability of the sensor. These advances will be enabled by the following improvements in the SPR sensor chip and its reader. The theoretical analysis indicates that by adjusting the operating wavelength, three fold enhancement of the refractive index resolution can be achieved. In addition, the number of sensing channels and time resolution can be increased by improving the imaging optics allowing measurement from denser arrays. The stability of the sensor can be increased by avoiding the excitation of surface plasmons through liquid samples, e.g. employing optical structure with surface plasmons coupled though a thin metal layer.

6 Acknowledgements

At this place, I would like acknowledge many people who helped me during my doctoral studies. I would especially like to thank to Dr. Jiří Homola who introduced me to the fascinating field of surface plasmon resonance optics and its biosensor applications.

I would like to express my thanks to Dr. Miroslav Miler who kindly guided me through the world of diffractive optics and design of diffraction gratings. Also, my colleagues Pavel Adam, Olga Telezhnikova and Milan Vala deserve my thanks for the work on optimization of protocols for preparation of diffraction grating.

I wish to thank to Dr. Václav Malina and Petra Chocholáčová for preparation of thin films. In addition, thanks goes to Dr. Zbyněk Pientka for characterization of diffraction gratings by using Atomic Force Microscopy.

I wish to thank to Jan Habr for help with the design of mechanical components. Also, Ivo Tichý and Jiří Löffelmann deserve my thanks for development of electronics.

Thanks go to Jan Jirmásek, Marek Piliarik and Petr Hlavenka for help with the implementation of data-acquisition and data-processing into the SPR-Spectral software.

Thank you, Hana Vaisocherová, Kateřina Mrkvová and Marketa Lachmanová for kind support during the experiment in which the SPR sensor device was applied for detection of biomolecular analytes.

In addition, I would like thank to all my colleagues from the Dr. Homola's research group for the friendship and warm atmosphere I had the chance to enjoy with them in many situations in the lab, while having a beer, on the tennis or squash court etc.

Finally, I wish to thank to my family and friends for keeping my life in proper balance.

7 References

[1] Shah J., Wilkins E., Electrochemical Biosensors for Detection of Biological Warfare Agents, *Electroanalysis* 15 (2003), 157-167.

[2] Suzuki H., Advances in the Microfabrication of Electrochemical Sensors and Systems, *Electroanalysis* 12 (2000), 703-715.

[3] Raiteri R., Grattarola M., Butt H.J., Skládal P. Micromechanical cantilever-based biosensors, *Sensors and Actuators*, B 79 (2001) 115-126.

[4] Skládal P, Piezoelectric quartz crystal sensors applied for bioanalytical assays and characterization of affinity interactions, *Journal of the Brazilian Chemical Society* 14 (2003) 491-502.

[5] O'Sullivan C.K., Guilbault G.G., Commercial quartz crystal microbalances - theory and applications, *Biosensors & Bioelectronics* 14 (1999) 663-670.

[6] Alan D. Stuart, Some applications of infrared optical sensing, *Sensors and Actuators* B, 11 (1993) 185-193.

[7] Nguyen Quy Dao and Michel Jouan, The Raman laser fiber optics (RLFO) method and its applications, *Sensors and Actuators* B, 11 (1993) 147-160.

[8] Wolfgang Trettnak, Otto S. Wolfbeis, Fully reversible fibre-optic glucose biosensor based on the intrinsic fluorescence of glucose oxidase, *Analytical Chimica Acta*, 221 (1989) 195-203.

[9] Dmitry B. Papovsky, Janos Olah and Ilya N. Kurochkin, Fiber-optic lifetime-based enzyme biosensor, *Sensors and Actuators* B, 11 (1993) 525-530.

[10] Medintz I.L., Clapp A.R., Mattoussi H., et al. Self-assembled nanoscale biosensors based on quantum dot FRET donors, *Nature Materials* 2 (9) (2003) 630-638.

[11] R. Cush, J. M. Cronin, W. J. Stewart, C. H. Maule, J. Molloy, N. J. Goddard, The resonant mirror: a novel optical biosensor for direct sensing of biomolecular interactions Part I: Principle of operation and associated instrumentation, *Biosensors and Bioelectronics* 8 (1993) 347-354.

[12] B.T. Cunningham, P. Li, B. Lin, J. Pepper, Colorimetric resonant reflection as a direct biochemical assay technique, *Sensors and Actuators* B, 81 (2002) 316-328.

[13] D. Clerc and W. Lukosz, Integrated optical output grating coupler as refractometer and (bio-)chemical sensor, *Sensors and Actuators* B, 11, (1998) 461-465.

[14] G. Boisde, A. Harmer, Chemical and biochemical sensing with optical fibres and waveguides, Artech House (1996).

[15] F.S. Liegler and C.A.R. Taitt, Optical biosensors, Elsevier (2002).

[16] Cooper M.A., Label-free screening of biomolecular interactions, Anal. Bioanal. Chem. 377 (2003), 834-842.

[17] H.M. Striebel, P. Schellenberg, P. Grigaravicius, K.O. Greulich, Readout of protein microarrays using intrinsic time resolved UV fluorescence for label-free detection, *Proteomics* 4 (2004) 1703-1711.

[18] C. Stamm and W. Lukosz, Integrated optical difference interferometer as refractometer and chemical sensor, *Sensors and Actuators* B, 11 (1993) 177-181.

[19] Birkert O., Tunnenmann R., Jung G., Gauglitz G., Label-free parallel screening of combinatorial libraries using reflectometric interference spectroscopy, *Anal. Chem.* 74 (2002) 834-840.

[20] Jin G., Tengvall P. Lundstrom I., Arwin H. A biosensor concept based on imaging ellipsometry for visualization of biomolecular interactions, *Analytical Biochemistry*, 232 (1995) 69-72.

[21] www.biacore.com

[22] http://www.windsor-ltd.co.uk

[23] http://www.ibis-spr.nl

[24] Rich R.L., Myszka D.G., Survey of the year 2001 commercial optical biosensor literature, *Journal of Molecular Recognition* 15 (2002) 352-376.

[25] Yasmina S.N. Day, Cheryl L. Baird, Rebecca L. Rich and David G. Myszka**,** Direct comparison of binding equilibrium, thermodynamic, and rate constants determined by surface- and solution-based biophysical methods, *Protein Sci* (2002) 11: 1017-1025.

[26] Rich R.L., Myszka D.G., Advances in surface plasmon resonance analysis, *Current Opinion in Biotechnology*, 11 (2000) 54-61.

[27] J. Homola: Present and Future of Surface Plasmon Resonance Biosensors, *Analytical and Bioanalytical Chemistry*, 377 (2003) 528-539.

[28] J. Homola, S. Yee, G. Gauglitz: Surface plasmon resonance sensors: review, *Sensors and Actuators B*, 54 (1999) 3 - 15.

[29] R. Karlsson, SPR for molecular interactions analysis: a review of emerging application areas, *Journal of Molecular Recognition* 17 (2004) 151-161.

[30] C. Mouvet, R. D. Harris, C. Maciag, B. J. Luff, J. S. Wilkinson, J. Piehler, A. Brecht, G. Gauglitz, R. Abuknesha, G. Ismail, Determination of simazine in water samples by waveguide surface plasmon resonance, *Analytica Chimica Acta*, 338 (1997) 109 - 117.

[31] J. Homola, J. Dostálek, S. F. Chen, A. Rasooly, S. Jiang, S. S. Yee, Spectral surface plasmon resonance biosensor for detection of staphylococcal enterotoxin B in milk, *Int. J. Food Microbiology*, 75 (2002) 61-69.

[32] V. Koubová, E. Brynda, L. Karasová, J. Škvor, J. Homola, J. Dostálek, P. Tobiška, J. Rošický: Detection of foodborne pathogens using surface plasmon resonance biosensors, *Sensors and Actuators,* 74 (2001) 100-105.

[33] G.C.A.M. Brokken, R.J. Corbee, F. van Knapen, A.A. Berkwerff, Immunodetection of Salmonella group B, D and E using an optical surface plasmon resonance biosensor, *FEMS Microbiology Letters* 222 (2003) 75-82.

[34] T. T. Goodrich, H. J. Lee, and R. M. Corn, Direct detection of genomic DNA by enzymatically amplified SPR imaging measurements of RNA microarrays, J. *Am. Chem. Soc.*, 126 (2004) 4086-4087.

[35] J. Dostálek, J. Čtyroký, J. Homola, E. Brynda, M. Skalský, P. Nekvindová, J. Špirková, J. Škvor, J. Schröfel, Surface plasmon resonance biosensor based on integrated optical waveguide, *Sensors and Actuators B*, 76 (2001) 8-12.

[36] Choi K., Seo W., Cha S., Choi J., Evaluation of two types of biosensors for immunoassay of botulinum toxin, *Journal of Biochemistry and Molecular Biology* 31 (1998) 101-105.

[37] A.D. Wetson, L. Hood, Systems biology, proteomics, and the future of health care: towards predictive, preventive, and personalized medicine, *Journal of Proteome Research*, 3 (2004) 179-196.

[38] G. Marko-Varga, T.E. Fehringer, Proteomics and Diseases – the challenges for technology and discovery, *Journal of proteome research* 3 (2004) 167-168.

[39] S.W. Michnick, Proteomics in living cells, *Drug Discovery Today*, 9 (2004) 262-267.

[40] A. Navas, J.P. Albar, Applications of proteomics in phylogenetic and evolutionary studies, *Proteomics*, 4 (2004) 299-302.

[41] H. Zhu, M. Bilgin, R. Bangham, D. Hall, A. Casamayor, P. Berone, N. Lan, R. Jansen, S. Bidlingmaier, T. Houfek, T. Michel, . Miller, R.A. Dean, M., Gerstein, M. Snyder, Global analysis of protein activities using proteome chips, *Science*, 293 (2001) 2101-2105.

[42] B.B. Haab, M.J. Dunham, P.O. Brown, Protein microarrays for highly parallel detection and quantification of specific proteins and antibodies in complex solutions, *Genome biology* 2 (2001) 1-13.

[43] R.W. Wood, Anomalous diffraction gratings, *Phys. Rev.*, *48* (1935) 928-936.

[44] U. Fano, The theory of anomalous diffraction gratings and of Quasi-Stationary Wave on Metallic surfaces (Sommerfeld's waves), *J. Opt..Soc. Am.*, 31 (1941) 213-222.

[45] M.C. Hutley, F. Mayster, The total absorption of light by a diffraction grating, *Optics communications*, 19 (1976) 431-436.

[46] R.H. Ritchie, E.T. Arakawa, J.J. Cowan, R.N. Hamm, Surface-plasmon resonance effect in grating diffraction, *Phys. Rev. Lett.*, 21 (1968) 1530-1533.

[47] Hutley, Diffraction gratings,Academic, London, (1982).

[48] R. Petit, ed. Electromagnetic theory of gratings, Springer-Verlag, (1980).

[49] K. Welford, Surface plasmon-polaritons and their uses, *Optical Quantum Electronics*, 23 (1991) 1-27.

[50] W.L. Barnes, A. Deraux, T.W. Ebessen, *Nature*, 424 (2003) 824.

[51] E. Hutter, H.H. Fendler, Exploitaion of localized surface plasmon resonance, *Adv. Mater,* 16, No.19 (2004) 1685-1706.

[52] Cross G.H., Girling I.R. Petterson I.R., Cade N.A., Electronics letters 21 (1986) 1111.

[53] Simon H.J., Mitchelll D.E., Watson J.G., *Phys. Rev. Lett.*, 33 (1974) 153.

[54] G. M. Wysin, H. J. Simon, R. T. Deck, Optical bistability with surface plasmons, *Optics letters* 6 (1981) 30-33.

[55] H. Raether, The dispersion relation of surface plasmons on rough surface, a comment on roughness data, *Surface Science*, 125 (1983) 621-634.

[56] B. Fisher, T.M. Fisher, W. Knoll, Dispersion of surface plasmons on rectangular, sinusoidal and incoherent gratings, *J. Appl. Phys*, 75 (1994) 1577-1581.

[57] H. Reather: Surface plasmons on smooth and rough surfaces and on gratings, Springer tracks in modern physics, Vol 111, Springer Verlag, Berlin (1983).

[58] J. R. Samples, A.P. Hibbins, M.J. Jory, H. Azizbekyan, A surface plasmon study of the optical dielectric function of indium, *Journal of Modern Optics*, Vo. 47, No.7, (2000) 1227-1235.

[59] R.J. Warmack, S.L. Humprey, Observation of two surface plasmon modes on gold nanoparticles, *Phys. Rev. B*, 34 (1986) 2246-2252.

[60] Gotschy W, Vonmetz K. Leitner A. Aussenegg F.R., Thin films by regular patterns of metal nanoparticles: tayloring the optical properties by nanodesign, *Appl. Phys. B*, 63 (1996) 381-384.

[61] Girard C., Quidant R., Near-field optical transmittance of metal particle chain waveguide, *Optics Express*, Vol.12, No. 25 (2004) 6141-6146.

[62] M. Salerno, J.R. Krenn, A. Hohenau, H. Ditlbacher, G. Schider, A. Leitner, F.R. Aussenegg, The optical near-field of gold nanoparticle chains*, Opt.Commun*., 248 (2005) 543.

[63] A. Krishnan, T. Thio, T. J. Kim, H. J. Lezec, T. W. Ebbesen, P. A. Wolff, J.B. Pendry, L. Martin-Moreno, F. J. Garcia-Vidal, Evanescently coupled resonance in surface plasmon enhanced transmission, *Optics Communications,* 200 (2001) 1-7.

[64] Raffaele Colombelli, Kartik Srinivasan, Mariano Troccoli, Oskar Painter, Claire F. Gmachl, Donald M. Tennant, A. Michael Sergent, Deborah L. Sivco, Alfred Y. Cho, and Federico Capasso, Quantum Cascade Surface-Emitting Photonic Crystal Laser, *Science* (2003) 1374-1377.

[65] H.Ditlbacher, J.R.Krenn, B.Lamprecht, A.Leitner, F.R.Aussenegg, Metal nanoparticles for spectrally coded optical data storage, *Optics & Photonics News* 11(12), (2000), 43.

[66] Barnes W.L., Preist T.W, Litson S.C., Sambles J.R. Cotter N.P.K., Nash D.J., Photonic gaps in the dispersion of surface plasmons on gratings, *Phys. Rev. B.*, Vol. 51. (1995) 11164-11167.

[67] W.L. Barnes, T.W. Preist, S.C. Kitson, J.R. Sambles, Physical origin of photonic energy gaps in the propagation of surface plasmons on gratings, *Phys. Rev. B* (54), 9, (1996) 6227-6244.

[68] Nicholas Fang, Hyesog Lee, Cheng Sun, and Xiang Zhang, Sub–Diffraction-Limited Optical Imaging with a Silver Superlens**,** *Science*, (2005) 534-537.

[69] J. R.Krenn, H.Ditlbacher, G.Schider, A.Hohenau, A.Leitner, F.R.Aussenegg Surface plasmon micro- and nano-optics, *J.Microsc*., 209, (2003) 167.

[70] J. Homola, G. Schwotzer, H. Lehman, R.Willish, W. Ecke, H. Barlert, A New Optical Fiber Sensor for Humidity Measurement, Photonics' 95, Prague, Czech Republic, August 1995, *EOS Annual Meeting Digest Series*, 2A, 225-248.

[71] A. Schilling, O.Yavas, J. Bischof, J. Boneberg, and P. Leiderer, Absolute preasure measurement on nanosecond scale using surface plasmons, *Appl. Phys. Lett.*, 69, 27, (1996) 4159-4161.

[72] A. Chadwick, M. Gal, An optical temperature sensor using surface plasmons, *Japanese journal of Applied Physics*, 32 (1993) 2716-2717.

[73] G. Margheri, A. Mannoni, F. Quercioli, A new high-resolution displacement sensor based on surface plasmon resonance, *Proceeding of SPIE*, 2783 (1996) 211-220.

[74] B. Moslehi, M. W. Foster, P. Harvey, Optical Magnetic and Electric Field Sensors Based on Surface Plasmon Polariton Resonance Coupling, *Electronics Letters*, Vol.27 No.11. (1991) 951-953.

[75] C. Nylander, B.Liedberg and T. Lindt, Gas detection by Means of Surface Plasmon Resonance, *Sensors and Actuators*, 3 (1982/1983) 79-88.

[76] B. Liedberg, C. Nylander and I. Lundström, Surface Plasmon Resonance for Gas Detection and Biosensing, *Sensors and Actuators*, 4 (1983) 299-304.

[77] Chen. S., Liu L., Zhaou J., Jiang S., Controlling Antibody Orientation on Charges Self-Assembled Monolayers, *Langmuir*, 19 (2003) 2859-2864.

[78] Shumaker-Parry J.S, Zareie M.H., Aebersold R., Campbell C.T., Microspotting of Streptavidin and Double-Stranded DNA Arrays for High-Throughput Studies of Protein-DNA Interactions by Surface Plasmon Resonance Microscopy, *Anal. Chem.*, 74 (2004) 918-929.

[79] Ye L, Haupt K. Molecularly imprinted polymers as antibody and receptor mimics for assays, sensors and drug discovery. *Anal Bioanal Chem,*. 378 (2004) 1887.

[80] Yoshikawa M., Hotta N., Kyoumura J., Osagawa J. , Aoki T., Chiral recognition sites from carbonyldioxyglyceryl moiety by an alternative molecular imprinting, *Sensors and Actuators B,* 104 (2005) 282-288.

[81] Kikuchi K, Umehara T, Fukuda K, Hwang J, Kuno A, Hasegawa T, Nishikawa S, RNA aptamers targeted to domain II of hepatitis C virus IRES that bind to its apical loop region, *Journal of Biochemistry*, 133 (2003) 263-270.

[82] Chien-Ming Wu, Zhi-Cheng Jian, Shen-Fen Joe and Liann-Be Chang, High-sensitivity sensor based on surface plasmon resonance and heterodyne interferometry, *Sensors and Actuators* B, 92 (2003) 133-136.

[83] R. Karlsson, R. Stahlberg, Surface plasmon resonance detection and mutispot sensing for direct monitoring of interactions involving low-molecular-weight analytes for determination of low affinities, *Analytical Biochemistry*, 228 (1995) 284-280.

[84] J. S. Shumaker-Parry, C. T. Campbell, Quantitative methods for spatially resolved adsorption/desorption measurements in real time by surface plasmon resonance microscopy, *Anal. Chem.*, 76 (2004) 918-929.

[85] S.G. Nelson, R. S. Jorgenson, S.S. Yee: High sensitivity surface plasmon resonance sensor based on phase detection, *Sensors and Actuators* B, 65-36 (1996) 187-191.

[86] P. I. Nikitin, A.A. Beloglazov, V.E. Kochergin, M.V. Valeiko, T.I. Ksenevich, Surface plasmon resoance interferometry for biological and chemical sensing. *Sensors and Actuators* B 54 (1999) 43-50.

[87] M. Zhang, D. Uttamchandani: Optical chemical sensing employing surface plasmon resonance, *Electronics Letters*, Vol.24 No.23, (1988) 1469-1470.

[88] K. Matsubara, S. Kawata, S. Minami: Optical chemical sensor based on surface plasmon measurement, *Applied Optics* Vol.27, No.6 (1988) 1160.

[89] R. C Jorgenson, S. S Yee, A fibre-optic chemical sensor based on surface plasmon resonance, *Sensors and Actuators* B, 12 (1993) 213-220.

[90] A. Trouillet, C. Ronot-Trioli, C. Veillas, and H. Gagnaire, Chemical sensing by surface plasmon resonance in a multimode optical fibre, *Pure Applied Optics*, 5 (1996) 227 - 237.

[91] R. E. Dessy, W. J. Bender, Feasibility of a chemical microsensor based on surface plasmon resonance on fiber optics modified by multilayer vapor deposition, *Analytical Chemistry*, 66 (1994) 963 – 970.

[92] J. Homola, Optical fiber sensor based on surface plasmon excitation, *Sensors and Actuators* B, 29 (1995) 401 - 405.

[93] R. Slavík, J.Homola, Jiří Čtyroký, Miniaturization of fiber optic surface plasmon resonance, *Sensors and Actuators* B, 51 (1998) 311-315.

[94] H. J. M. Kreuwel, P. V. Lambeck, J. van Gent, T.J.A. Popma, Surface plasmon dispersion and luminiscence quenching applied to a planar waweguide sensors for measurement of chemical concentrations, *Proc. SPIE* , 789 (1987) 218–224.

[95] C. R. Lavers, J. S. Wilkinson, A waveguide-coupled surface plasmon resonance sensor for an aqueous environment, *Sensors and Actuators B,* 22 (1994) 475–481.

[96] R. D. Harris, J. S. Wilkinson, Waveguide surface plasmon resonance sensors, *Sensors and Actuators B,* 29 (1995) 261–267.

[97] M. N. Weiss, R. Srivastava, H. Grogner, Experimental investigation of a surface plasmon-based integrated-optic humidity sensor, *Electronics Letters*, 32 (1996) 842–843.

[98] J. Homola, J. Čtyroký, M. Skalský, J. Hradilová, P. Kolářová, A surface plasmon resonance based integrated optical sensor, *Sensors and Actuators B*, 38–39 (1997) 286–290.

[99] C. Mouvet, R. D. Harris, C. Maciag, B. J. Luff, J. S. Wilkinson, J. Piehler, A. Brecht, G. Gauglitz, R. Abuknesha, G. Ismail, Determination of simazine in water samples by waveguide surface plasmon resonance, *Analytica Chimica Acta*, 338 (1997) 109–117.

[100] D. C. Cullen, R. G. Brown, C. R. Lowe, Detection of Immuno-complex Fromation via Surface Plasmon Resonance on Gold-coated Diffraction Gratings, *Biosensors* 3 (1987/88) 211-225.

[101] C. R. Lawrence, N. J. Geddes, D. N. Furlong, J. R. Sambles, Surface plasmon resonance studies of immunoreactions utilizing disposable diffraction gratings, *Biosensors and Bioelectronics*, 11 (1996) 389-400.

[102] W. A. Challener, R. R. Ollman, K. K. Kam, A surface plasmon resonance gas sensor in a ‘compact disk’ format, *Sensors and Actuators* B, 56 (1999), 254-258.

[103] M. T. Gale, Replication technique for diffractive optical elements, *Microelectronic Engineering*, 34 (1997) 321-339.

[104] M. J. Jory, G. W. Bradberry, P. S. Cann and J. R. Sambles, A surfase-plasmon-based optical sensor using acusto-optics, *Meas. Sci. Technology*, 6 (1995) 1193-1200.

[105] J. M. Brockman, S. M. Fernandez, Grating-coupled surface plasmon resonance for rapid, label-free, array-based sensing, *Am. Laboratory*, 33 (2001) 37-40.

[106] J. Dostálek, J. Homola, M. Miler, Rich information format surface plasmon resonance biosensor based on array of diffraction gratings, *Sensors and Actuators B*, 107 (2005) 154-161.

[107] Rothenhäusler, B., Knoll W., Surface plasmon microscopy, *Nature*, 332 (1988) 615 – 617.

[108] Charles E. H. Berger, Tom A. M. Beumer, Rob P. H. Kooyman, and Jan Greve, Surface Plasmon Resonance Multisensing, *Anal. Chem*., 70 (1998) 703-706.

[109] Marek Piliarik, Hana Vaisocherová and Jiří Homola, A new surface plasmon resonance sensor for high-throughput screening applications, *Biosensors and Bioelectronics*, *20* (2005) 2104-2110.

[110] S. Sjölander, C. Urbanitzky, Integrated fluid handling system for biomolecular interaction analysis, *Anal. Chem.*, 63 (1991) 2338-2345.

[111] S. Löfas, M. Malmqvist, I. Rönnberg, E. Stenberg, B. Liedberg, I. Kundström, Bioanalysis with surrface plasmon resonance, *Sensors and Actuators B*, *5* (1991) 79 - 84.

[112] M. J. O'Brien, V. H. Perez-Luna, S.R.J. Brueck, G.P. Lopez, A surface plasmon resonance array biosensor based on spectroscopic imaging, *Biosensors and Bioelectronics*, 16 (2001) 97-108.

[113] C. Thirstrup, W. Zong, M. Borre, H. Neff, H. C. Pedersen and G. Holzhueter, Diffractive optical coupling element for surface plasmon resonance sensors, *Sensors and Actuators B* 100 (2004) 299-309.

[114] J. Homola, J. Dostálek, S. F. Chen, A. Rasooly, S. Jiang, S. S. Yee, Spectral surface plasmon resonance biosensor for detection of staphylococcal enterotoxin B in milk, *Int. J. Food Microbiology*, 75 (2002) 61-69.

[115] G.G. Nenninger, J.B. Clendenning, C.E. Furlong, S.S. Yee, Reference-compensated biosensing using a dual-channel surface plasmon resonance sensor system based on a planar lightpipe configuration, *Sensors and Actuators B*, 51 (1998) 38-45.

[116] J. Homola, J. Dostálek, J. Čtyroký, Novel approach to surface plasmon resonance multichannel sensing, Optical Engineering for Sensing and Nanotechnology, Yokohama, Japan, June 6-8, *SPIE Proceedings* 4416 (2001) 86-89.

[117] J. Homola, H. B. Lu, S. S. Yee: Dual-Channel Surface Plasmon Resonance Sensor with Spectral Discrimination of Sensing Channels Using a Dielectric Overlayer, *Electronics Letters*, 35 (1999) 1105-1106.

[118] J. Homola, H.B. Lu, G. G. Nenninger, Jakub Dostálek, S. S. Yee, A novel multichannel surface plasmon resonance biosensor, *Sensors and Actuators B*, 76 (2001) 403 - 410.

[119] J. Dostálek, H. Vaisocherová, J. Homola, Multichannel Surface Plasmon Resonance Biosensor with Wavelength Division Multiplexing, *Sensors and Actuators B*, 108 (2005) 758-764.

[120] Brynda E., Houska M., Škvor J., Ramsden J.J., Immobilisation of multilayer bioreceptror assemblies on solid substrates, *Biosensors and Bioelectronics*, 13 (1998) 165-172.

[121] Brynda E., Homola J., Houska M., Pfeifer P., Škvor J., Antibody networks for surface plasmon resonance immunosensors, *Sensors and Actuators* B 54 (1999) 132-136.

[122] Xia N., Shumaker-Parry J.S., Zareie M.H., Campbell C.T., Castner D.G., A Streptavidin linker layer that functions after drying, *Langmuir* 20 (2004) 3710-3716.

[123] Lofas S., Johnsson B., A novel hydrogel matrix on gold surface in surface plasmon resonance sensors for fast and efficient covalent immobilization of ligands, *J. Chem. Soc. Chem. Commun.* (1990) 1526-1528.

[124] Lofas S., Johnsson B., Edstrom A. Hansson A., Lindquist G., Hillgren R.M.M., Stigh L., Methods for site controlled coupling to carbocymethyldextran surfaces in surface plasmon resonance sensors, *Biosensors and Bioelectronics* 10 (1995) 813-822.

[125] Delamarche E., Bernard A., Schmidt H., Bietsch A., Michel B., Biebuyck, Microfluidic network for chemical patterning of substrates: design and application to bioassays, *J. Am. Chem. Soc.* 120 (1998) 500-508.

[126] Lee H.J., Goodrich T.T, Corn R.M., Imaging measurements of 1-D and 2-D DNA microarrays created from microfluidc channels on gold thin films, *Anal. Chem.*, 73 (2001) 5525-5531.

[127] Park JP, Lee SJ, Park TJ, et al.,Microcontact printing of biotin for selective immobilization of streptavidin-fused proteins and SPR analysis, *Biotechnology and Bioprocess Engineering*, 9 (2004) 137-142.

[128] Bernard A., Delamarche E., Schmidt H., Michel B., Bosshard H.R., Biebuyck H., Printing patterns of proteins, *Langmuir*, 14 (1998) 2225-2229.

[129] Lahiri J., Ostuni E., Whitesides G.M., Patterning ligands on reactive SAMs by microcontact printing, *Langmuir* 15 (1999).

[130] J. S. Shumaker-Parry, M. H. Zareie, R. Aebersold, C. T. Campbell, Microspotting streptavidin and double-stranded DNA arrays on gold for high-throughput studies of protein-DNA interactions by surface plasmon resonance microscopy, *Anal. Chem.*, 76 (2004) 918 – 929.

[131] Glezos N., Misiakos K., Kabakakos S., Petrou P., Terzoudi G., Electron beam pattering of biomolecules, *Biosensors and Bioelectronics* 17 (2002) 279-282.

[132] Delamarche E., Sundarababu G., Biebuyck H., Michel H., Gerber Ch., Sigrist H., Wolf H., Ringsdorf H., Xanthopuolos N., Matieu H.J., Immobilization of antibodies on a photoactive self-assembled monolayer on gold, *Langmuir* 12 (1996) 1997-2006.

[133] Boozer C., Yu O., Chen S., Lee C., Homola J., Yee S.S, Jiang S., Surface functionalization for self-referencing surface plasmon resonance (SPR) biosensors by multi-step self-assembly, *Sensors and Actuators B*, 90 (2003) 22–30.

[134] V. Sikavitsas, J. M. Nitsche, T. J. Mountziaris, Transport and Kinetic Processes Underlying Biomolecular, 18 (2002) *Biotechnol. Prog,* 885-897.

[135] M. Furuki, J. Kameoka, H.G. Greighead, M.S. Isaacson, Surface plasmon resonance sensors utilizing microfabricated channels, *Sensors and Actuators B*, 79 (2001), 63-69.

[136] E. Kim, Y. Xia , G.M. Whitesides, Micromolding in capillaries: application in material science, *J. Am. Chem. Soc*, 188 (1996) 5722-5731.

[137] E. Delamarche, A. Bernard, H. Schmidt, A. Bietsch, B. Michel, H. Biebuyck, Microfluidic networks for chemical patterning of substrates: design and application to bioassays, *J. Am. Chem. Soc.* 120 (1998) 500-508.

[138] T. T. Goodrich, H. J. Lee, and R. M. Corn, Direct detection of genomic DNA by enzymatically amplified SPR imaging measurements of RNA microarrays, *J. Am. Chem. Soc.*, 126 (2004) 4086-4087.

[139] A.R. Wheeler, S.C. Chah, R.J. Whelan, R.N. Zare, Poly(dimethylsiloxane) microfluidic flow cells for surface plasmon resonance spectroscopy, *Sensors and Actuators* B 98 (2004) 208-214.

[140] D.C. Duffy, J.C. McDonald, O.J.A. Schueller, G.M. Whitesides, Rapid prototyping of microluidic systems in poly(dimetylsiloxane), *Anal. Chem.* 70 (1998) 4974-4984.

[141] N.E. Glass, M. Weber, D.L. Mills, Attenuation and dispersion of surface plasmon polaritons on gratings, *Phys. Rev. B*, 29 (1984) 6548-6559.

[142] M.G. Weber, Highly accurate renormalized mode-coupling theory for reflectivity of diffraction grating, *Phys. Rev. B.*, 33 (1986) 909-913.

[143] Wang B, Wang GP, Surface plasmon polariton propagation in nanoscale metal gap waveguides, *Optics Letters* 29, 17, (2004) 1992-1994.

[144] Nicolas Bonod, Stefan Enoch, Lifeng Li, Evgeny Popov, Michel Nevière, Resonant optical transmission through thin metallic films with and without holes, *Optics Express,* Vol. 11, No.5 (2003) 482-490.

[145] Suntak Park, Gwansu Lee, Seok Ho Song, Cha Hwan Oh, and Pill Soo Kim, Resonant coupling of surface plasmons to radiation modes by use of dielectric gratings, *Optics Letters* Vol. 28, No. 20 (2003) 1870-1872.

[146] A. Pomp, The integral method for coated gratings: computation cost, *Journal of Modern Optics*, Vol. 38, No.1, (1991) 109-120.

[147] W.A. Challener, Vector diffraction of a grating with conformal thin films, *J. Opt. Soc. Am. A.* 13 (1996) 1859-69.

[148] L. I. Goray, "Modified integral method for weak convergence problems of light scattering on relief grating," in Diffractive and Holographic Technologies for Integrated Photonic Systems, R. I. Sutherland, D. W. Prather and I. Cindrich, eds., SPIE Proceedings, Vol. 4291 (2001) 1-12.

[149] L.I. Goray, J.F. Seely, Efficiencies of master, replica , and multilayer gratings for soft-x-ray-extreme-ultraviolet range: modeling based on the modified integral emthod and comparison with measurements, *Applied Optics*, Vol. 41, No.7, (2002) 1434-1445.

[150] M. G. Moharam, T.K. Gaylord, Rigorous coupled-wave analysis of metallic surface-relief grating, *J. Opt. Soc. Am. A.*, 13 (1996) 1859-69.

[151] M. G. Moharam, T.K. Gaylord, Rigorous coupled-wave analysis of grating diffraction - E mode polarization and losses, *J. Opt. Soc. Am.*, 73 (1983) 451-55.

[152] L. Li, A modal analysis of lamellar diffraction grating in conical mountings, *Journal of Modern Optics*,Vol. 40, No.4, (1993) 553-573.

[153] L. Li, Multilayer modal method for diffraction gratings of arbitrary profile, depth, and permittivitty, *J. Opt. Soc. Am. A.*, 10, (1993), 2581-2591.

[154] J. Chandezon, M.T. Depuis, G. Cornet, D. Maystre, Multicoated gratings: a differential formalism applicable in the entire optical region, *J. Opt. Soc. Am.*, Vol 72, No.7, (1982) 839-846.

[155] L. I. Goray, "Modified integral method and real electromagnetic properties of echelles," in *Diffractive and Holographic Technologies for Integrated Photonic Systems*, R. I. Sutherland, D. W. Prather, and I. Cindrich, eds., SPIE Proceedings, Vol. 4291 (2001) 13-24.

[156] Berenger J.P., A perfectly matched layer for the absorption of electromagnetic waves, *J. Comput. Phys.*, 114 (1994) 185-200.

[157] http://www.gsolver.com

[158] http://www.pcgrate.com

[159] http://camfr.soureforge.org

[160] E.-H. Rosengart, I. Pockrand, Influence of higher harmonics of a grating on the diffraction orders via surface surface plasmons, *Optics letters*, Vol.1, No.6, (1977) 194-195.

[161] J. Burke, G. Stegman and T. Tamir, "Surface- polariton- like guided by thin, lossy metal films," *Phys. Rev. B.,* 33 (1986) 5186- 5201.

[162] R. E. Smith S. N. Houde Walter G. W. Forbes**,** Mode Determination For Planar Waveguides Using the Four-Sheeted Dispersion Relation, *IEEE Journal of Quantum Electronics* 28**,** No. 6, (1992) 1520-1526.

[163] http://www.waterloo.com

[164] J. Homola, I. Koudela, S. S. Yee, Surface plasmon resonance sensors based on diffraction gratings and prism couplers: sensitivity comparison, *Sensors and Actuators B*, 54, (1999) 16-24.

[165] B. Liedberg, I. Lunström, E. Stenberg, Principles of biosensing with extended coupling matrix and surface plasmon resoance, *Sensor and Actuators* B, 11 (1993) 63-72.

[166] G.G. Nenninger, M. Piliarik, J. Homola, Data analysis for optical sensors based on spectroscopy of surface plasmons, *Measurement Science and Technolog*y, 13 (12) (2002) 2038-2046.

[167] Chinowsky T M, Jung L S and Yee S S Optimal linear data analysis for surface plasmon resonance biosensors, *Sensors Actuators* B, 54 (1999) 89–97.

[168] Petr Tobiška and Jiří Homola, Advanced data processing for SPR biosensors, *Sensors and Actuators B*, 107 (2005) *162-169*

[169] Y. Xia, G. M. Whitesides, Soft Lithography, *Angew. Chem. Int. Ed.*, 37 (1998) 550-575.

[170] I. Aubrecht, M. Miler, Profile of relief phase gratings used for uniform multiple-beam splitting, *Optics Letters*, 18 (16) (1993) 1287-1289.

[171] D.E. Aspens: Optical properties of thin films, *Thin Solid Films*, 89 (1982) 249-262.

[172] G. M. Hale, M. R. Querry, Optical constants of water in the 200-nm to 200-μm wavelength region, *Applied Optics*, Vol. 12, No.3, (1973) 555-562.

[173] D.C. Carter, J. X. Ho, Structure of serum albumins, *Advances in Protein Chemistry*, 45 (1994) 153-203.

[174] Singh J., Optoelectronics - an introduction to materials and devices, McGraw-Hill, (1996)

[175] J. Homola, Surface Plasmon Resonance, Springer-Verlag, Berlin-Heidelberg-New York (2006)

[176] Ladd J, Boozer C, Yu QM, et al., DNA-directed protein immobilization on mixed self-assembled monolayers via a Streptavidin bridge, *Langmuir*, 20 (2004) 8090-8095

8 Appendix

8.1 Optical parameters of used materials

Optical parameters of materials used in simulations were taken from [171] and [172] for gold and water, respectively. The permittivity of gold and water is shown in Fig. 91 and Fig. 92, respectively. The permittivity of gold used in experiments (deposited by thermal evaporation atn the temperature of 21˚C and 150˚C) was measured using ellipsometry, see Fig. 93.

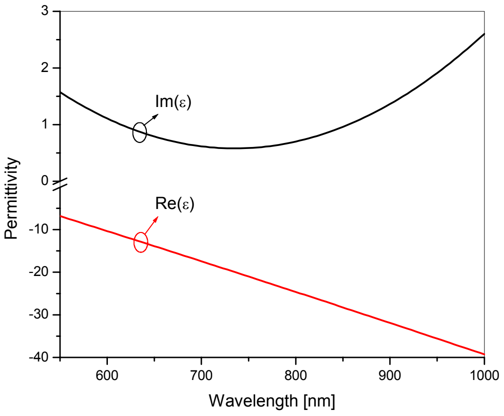

Fig. 91 Permittivity of gold, taken from [171].

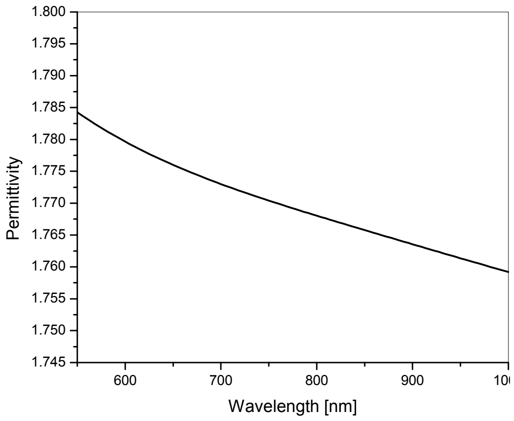

Fig. 92 Permittivity of water, taken from [172].

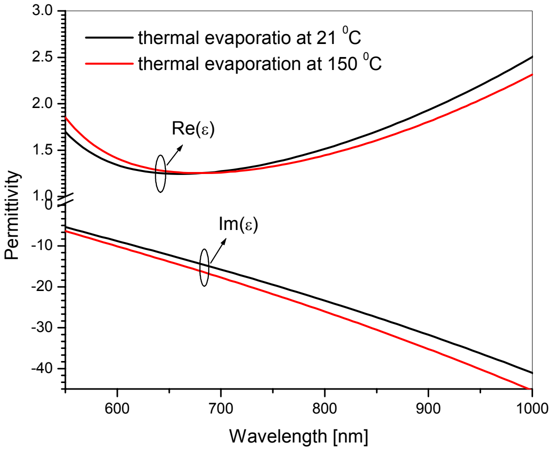

Fig. 93 Measured permittivity of gold layer with the thickness of 100 nm prepared by thermal evaporation at the temperature of 21˚C and 150˚C.

8.2 Schemes of SPR sensor components

8.2.1 Mould for casting of PDMS stamp

Acrylic mould used for casting of PDMS stamp for replication of diffraction gratings. Figure a) shows bottom of the mould into which a glass slide (dimensions 32x15x1.5 mm) with a diffraction grating was placed. The grating was fastened into the mould by the Mylar layer (Figure c) with an adhesive layer and a mould frame mounted using two M3 screw (see Figure b).

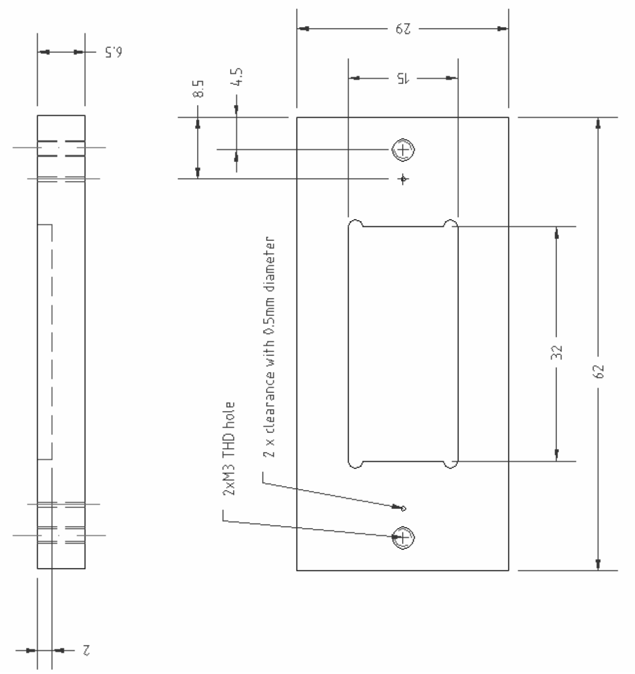

a)

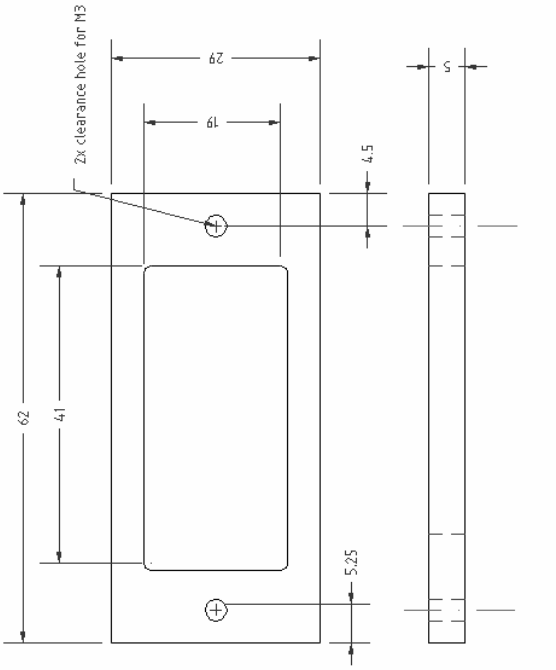

b)

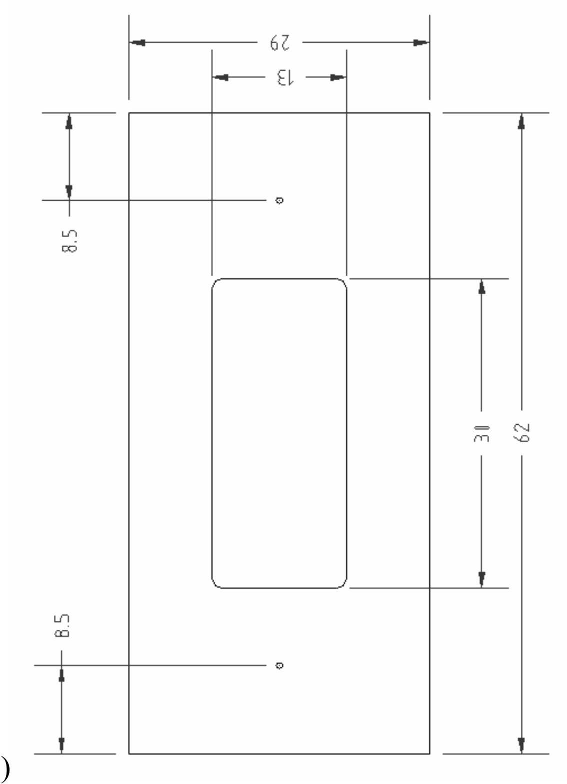

c)

8.2.2 Mask for preparation of an array of metal coatings

Mask and alignment frame for preparation of an array of metal coatings fabricated from phosphor-bronze by lithography. These components were placed into the chip holder shown below which was made from duralalumin.

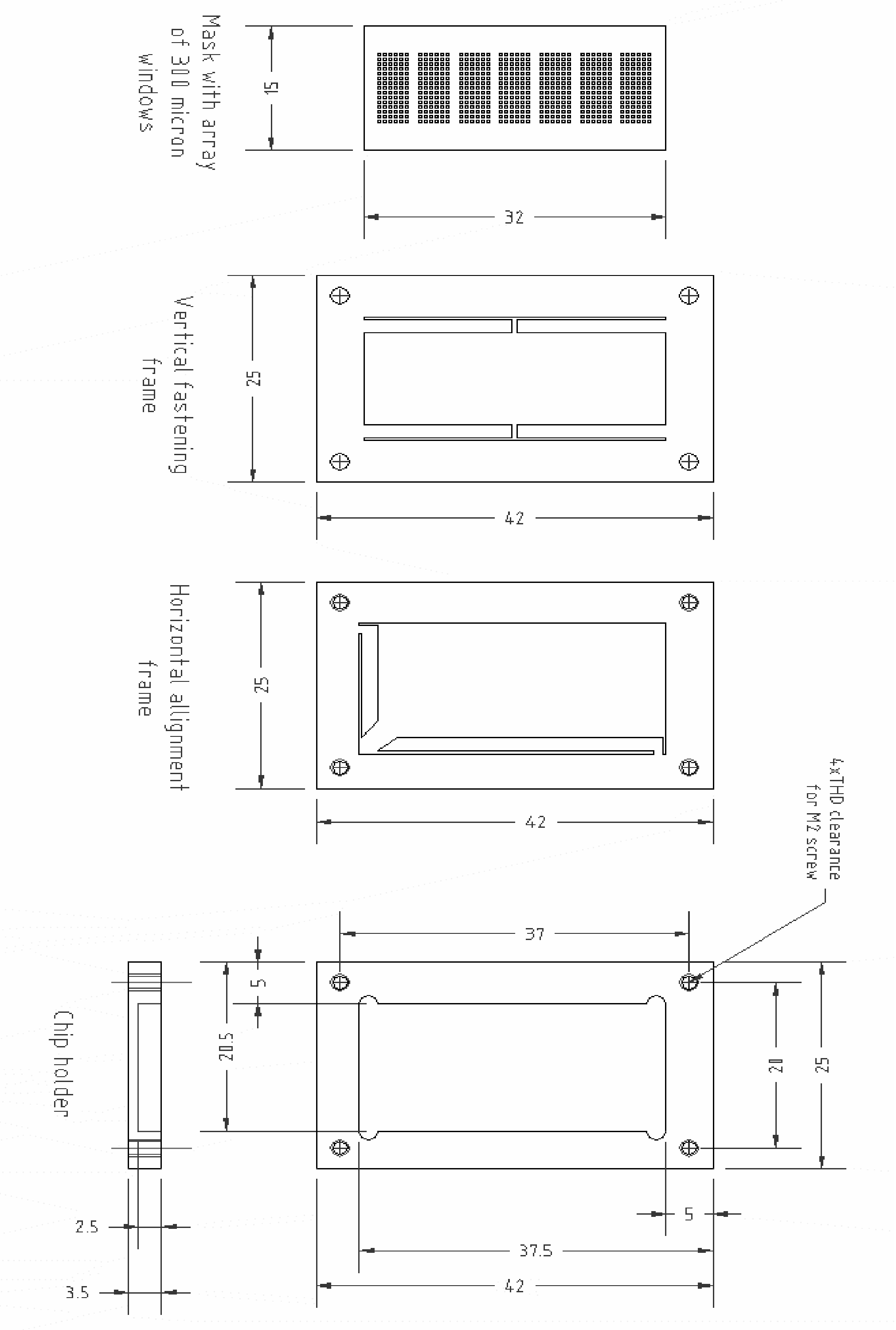

8.2.3 Fluidic manifold

Fluidic manifold cut into a 50 micron thick Mylar sheet by CO_2 laser beam with flow cells, input and output ports with flow channels. Mylar 1 and 3 were without an adhesive layer and Mylar 2 was coated with an adhesive layer on both sides.

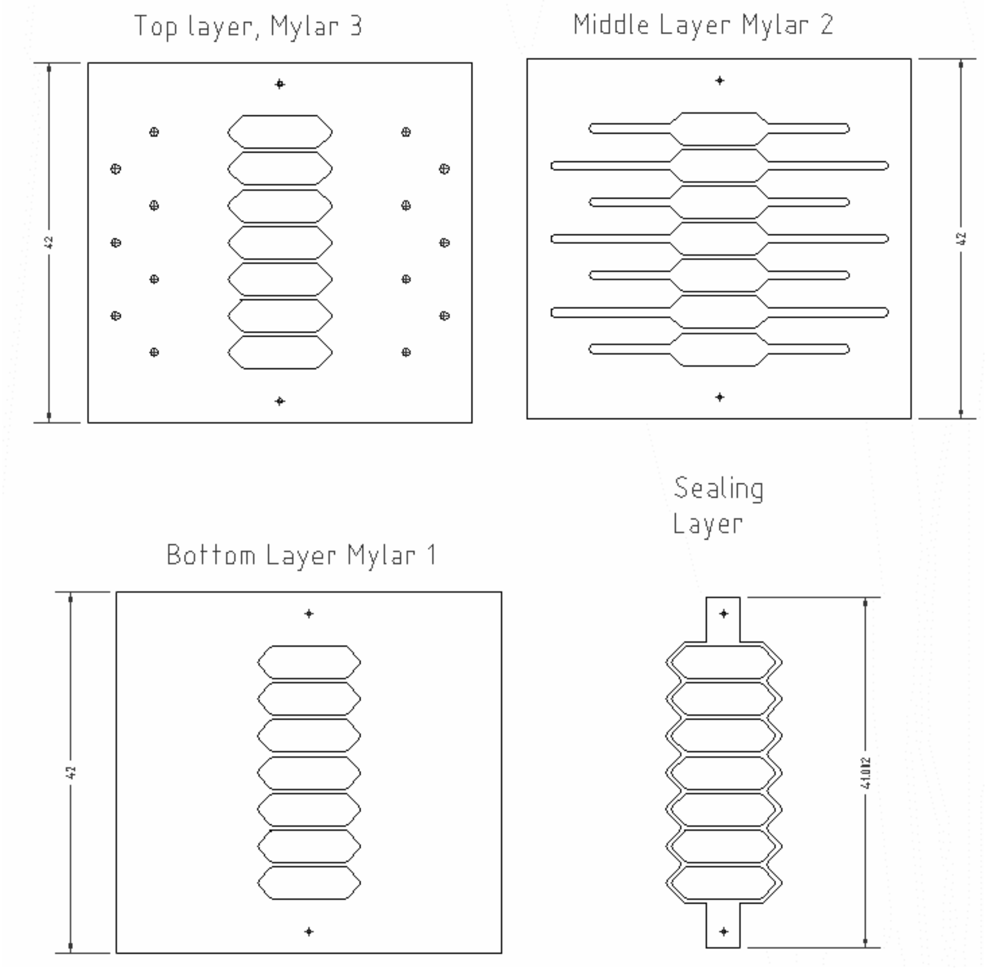

Frame to support the fluidic manifold and allow connection to tubing, cut into Mylar sheet made from acrylic.